

Ab initio structural prediction of interface and defect reconstructions in group IV crystals



Dissertation

zur Erlangung des akademischen Grades
doctor rerum naturalium (Dr. rer. nat.)

vorgelegt dem Rat der Physikalisch-Astronomischen Fakultät
der Friedrich-Schiller-Universität Jena

von M.Sc. Lin Sun
geboren am 30. Dezember 1989 in Hubei, China

Gutachter:

1. Prof. Dr. Silvana Botti
2. Prof. Dr. Fernando Nogueira
3. Prof. Dr. Gian-Marco Rignanesi

Tag der Disputation: 19. Oktober 2021

Abstract

In this thesis, we develop a constrained structural prediction approach for the structural reconstructions of interfaces and point defects in crystals.

First, we investigate the structure-property relations for a large and varied family of symmetric and asymmetric tilt grain boundaries in polycrystalline silicon. We find a rich polymorphism in the interface reconstructions, with recurring bonding patterns that we classify in increasing energetic order. We systematically classify the grain boundaries into different types by the structural reconstructions when atoms are removed or added at the interface. Then, we extend the low-energy structures from silicon to other group-IV elementary crystals (carbon, germanium, and tin) and study their stability. Finally, a clear relation between bonding patterns and electrically active grain boundary states is unveiled and discussed.

Second, we study the reconstructions of diamond interfaces along different directions and focus on the formation of diamond-graphite hybrid structures. We find that the formed graphite layers at interfaces parallel to the [100] axis are always following similar patterns. In contrast, for the interfaces parallel to the [110] axis, the graphite layers can be formed along two directions. We find the number of the graphite layers is limited by the distances between the bonded atoms on the diamond surface. We also compare the formation of diamond-graphite structures in carbon grain boundaries. Finally, how the electronic properties of diamond is affected by the graphitization is discussed.

Finally, we extend our approach to the study of point defect geometries in hexagonal silicon. We obtain among the lowest-energy structures the hexagonal counterparts of all known defects of cubic silicon, together with other often more complex geometries. Neutral vacancies, fourfold-coordinated and Frenkel defects have comparable formation energies in both hexagonal and cubic phases, while some interstitial defects become considerably more stable in the hexagonal lattice. Furthermore, due to the reduced symmetry, formation energies can depend on the orientation of the defect with respect to the *c*-axis. The density of states of the defective supercells is calculated to determine which defects lead to electronic states in the band gap, potentially affecting the performance of optoelectronic devices based on hexagonal group-IV crystals.

Abstrakt

In dieser Arbeit entwickeln wir einen eingeschränkten Strukturvorhersageansatz für die strukturelle Rekonstruktion von Grenzflächen und Punktdefekten in Kristallen.

Zunächst untersuchen wir die Struktur-Eigenschafts-Beziehungen für eine große und vielfältige Familie von symmetrischen und asymmetrischen Kipp-Korngrenzen in polykristallinem Silizium. Wir finden einen reichen Polymorphismus in den Grenzflächen-Rekonstruktionen, mit wiederkehrenden Bindungsmustern, die wir in zunehmender energetischer Ordnung klassifizieren.

Wir klassifizieren die Korngrenzen systematisch in verschiedene Typen anhand der strukturellen Rekonstruktionen, wenn Atome an der Grenzfläche entfernt oder hinzugefügt werden. Dann erweitern wir die niederenergetischen Strukturen von Silizium auf andere Elementarkristalle der Gruppe IV (Kohlenstoff, Germanium und Zinn) und untersuchen deren Stabilität. Schließlich wird ein klarer Zusammenhang zwischen Bindungsmustern und elektrisch aktiven Korngrenzenzuständen aufgedeckt und diskutiert.

Zweitens untersuchen wir die Rekonstruktionen von Diamantgrenzflächen entlang verschiedener Richtungen und konzentrieren uns auf die Bildung von Diamant-Graphit-Hybridstrukturen. Wir finden, dass die gebildeten Graphitschichten an Grenzflächen parallel zur [100]-Achse immer ähnlichen Mustern folgen. Im Gegensatz dazu können die Graphitschichten an Grenzflächen parallel zur [110]-Achse in zwei Richtungen gebildet werden. Wir finden, dass die Anzahl der Graphitschichten durch die Abstände zwischen den gebundenen Atomen auf der Diamantoberfläche begrenzt ist. Wir vergleichen auch die Bildung von Diamant-Graphit-Strukturen in Kohlenstoff-Korngrenzen. Schließlich wird diskutiert, wie die elektronische Struktur von Diamant durch die Graphitierung beeinflusst wird.

Schließlich erweitern wir unseren Ansatz auf die Untersuchung von Punktdefektgeometrien in hexagonalem Silizium. Wir erhalten unter den Strukturen mit der niedrigsten Energie die hexagonalen Gegenstücke aller bekannten Defekte des kubischen Siliziums, zusammen mit anderen oft komplexeren Geometrien. Neutrale Leerstellen, vierfach koordinierte und Frenkel-Defekte haben sowohl in der hexagonalen als auch in der kubischen Phase vergleichbare Bildungsenergien, während einige interstitielle Defekte im hexagonalen Gitter deutlich stabiler sind. Außerdem können die Bildungsenergien aufgrund der reduzierten Symmetrie

von der Orientierung des Defekts in Bezug auf die c -Achse abhängen. Die Zustandsdichte der defekten Superzellen wird berechnet, um festzustellen, welche Defekte zu elektronischen Zuständen in der Bandlücke führen, die möglicherweise die Leistung von optoelektronischen Bauelementen auf Basis von hexagonalen Gruppe-IV-Kristallen beeinflussen.

Table of contents

| | | |
|----------|--|-----------|
| 1 | Introduction | 1 |
| 2 | Theoretical Background | 5 |
| 2.1 | Density Functional Theory | 5 |
| 2.1.1 | Hohenberg-Kohn Theorem | 6 |
| 2.1.2 | Kohn-Sham Equations | 8 |
| 2.1.3 | Exchange-Correlation Energy Functionals | 9 |
| 2.2 | Density Functional Tight-Binding | 11 |
| 2.3 | Basic knowledge of grain boundaries | 13 |
| 3 | Constrained structural prediction approaches and computational details | 17 |
| 3.1 | Interface structure prediction | 17 |
| 3.2 | Constrained structural prediction approaches | 19 |
| 3.2.1 | Approach for interface reconstructions | 20 |
| 3.2.2 | Approach for point defects | 22 |
| 3.3 | Computational details | 24 |
| 3.3.1 | Simulations for silicon GBs | 24 |
| 3.3.2 | Simulations for interface reconstructions in diamond | 26 |
| 3.3.3 | Simulations for point defects in hexagonal silicon | 27 |
| 4 | Structure-property relations at silicon grain boundaries | 29 |
| 4.1 | Low-energy grain boundaries | 29 |
| 4.1.1 | Grain boundaries with rotation axis [110] | 29 |
| 4.1.2 | Grain boundaries with rotation axis [100] | 41 |
| 4.1.3 | Comparison of GB energies | 43 |
| 4.1.4 | Comparison of energy with different DFTB parameterizations | 44 |
| 4.1.5 | Extension of the study of low-energy GBs to other group-IV elementary crystals | 45 |

| | | |
|----------|---|-----------|
| 4.2 | Are the interfaces more stable after removal of atoms? | 49 |
| 4.3 | Electronic properties of reconstructed interfaces | 58 |
| 5 | Simulation of diamond/graphite interface in crystalline carbon | 61 |
| 5.1 | Diamond-graphite: a new carbon allotrope | 61 |
| 5.2 | Reconstructions of diamond interfaces | 62 |
| 5.2.1 | Reconstructions of (001) diamond interface | 62 |
| 5.2.2 | Reconstructions of interfaces parallel to the [110] axis | 65 |
| 5.2.3 | Reconstructions of interfaces parallel to the [100] axis | 72 |
| 5.3 | Diamond-graphite structures in tilt grain boundaries | 76 |
| 5.4 | Variation of atomic bonds in diamond-graphite | 78 |
| 5.5 | Electronic properties of diamond-graphite structures | 80 |
| 6 | Structural prediction of point defects in hexagonal silicon | 85 |
| 6.1 | Hexagonal phase is interesting | 85 |
| 6.2 | Geometric properties of the low-energy point defects | 87 |
| 6.3 | Electronic properties of the low-energy point defects | 91 |
| 7 | Summary and Conclusions | 93 |
| | References | 97 |

Chapter 1

Introduction

In solid-state physics, interfaces are defined as the small regions that separate two matters in intimate contact with each other [1]. Interfaces are of great importance that they strongly or even control the most important properties of materials in high-technology applications [2]. The prediction of microscopic atomic structures of interfaces, and the determination of their effects on the electronic properties of a multicomponent material is a challenging open problem of materials science. A solution to this scientific question is of utmost importance to understand, e.g., how to control the overall electronic response of a functional material.

An ubiquitous example of such internal interfaces is grain boundaries (GBs), i.e. two-dimensional defects that separate crystalline domains with different orientation in a polycrystalline sample [3]. GBs can affect dramatically structural, electronic, transport, and optical properties of semiconducting crystals used in microelectronic devices or solar cells [4–13]. In the latter devices, in particular, the effect of GBs is generally considered to be detrimental to charge transport, as deep defect states at internal interfaces can act as recombination centers for excited electrons and holes. However, the introduced disorder has a beneficial effect on light absorption efficiency, as it allows to break the \mathbf{k} -point selection rule for optical transitions [14]. A deep understanding of low-enthalpy structural reconstructions at GBs would provide the missing insight on how GBs limit energy conversion efficiency, disclosing new routes to enhance both light absorption and charge mobility in photovoltaic devices.

Due to the structural complexity of interfaces, the investigation of the precise link between material performance and interface reconstructions remains a challenging task for experimental techniques and computer simulations. Thanks to recent advances in nanocrystalline engineering, it is now possible to incorporate specific interface in a material [15, 16]. Directly experimental observations of interfacial geometries by high-resolution transmission electron microscopy are extremely difficult [17]. But, when they are successful, they generally show that GB atomic structures can bear little resemblance to intuitively guessed atomic

configurations [18]. In many cases, experimental images do not provide sufficient information about the atomic-level structure, so that, without theoretical support, it remains debated whether certain GBs are ordered, partially ordered, amorphous, or liquid. Unfortunately, and despite the large amount of theoretical work in literature, a comprehensive understanding of low GB reconstructions determine the electronic properties of a realistic polycrystal is still missing. The main difficulty is that experimental data are incomplete and simulations do not always sample the configuration space in an adequate manner.

Thus, it is my intention to provide an accurate and unbiased *ab initio* procedure for the extraction of structure-property relations of different families of interfaces in this thesis. We propose an efficient approach for the prediction of low-energy reconstructions of interfaces, that retains and combines strong points of previous approaches and tries to go beyond still existing limitations. In Chapter 3, a brief introduction of the current interface prediction methods is given, then, I will introduce our constrained structural prediction approaches in detail, followed by the computational details for different systems we have studied in this thesis.

The rest part of this thesis is organized as follows. Chapter 2 is an introduction to the fundamental theoretical background. In this part, the density functional theory (DFT) will be introduced briefly, then I will present a description of density-functional tight-binding (DFTB). Finally, I introduce the basic knowledge of the grain boundaries.

In Chapter 4, I apply our approach to study a set of low-energy tilt GBs in silicon. The focus on this family of GBs is motivated by the large amount of data available in the literature for polycrystalline silicon, which makes this system ideal for a thorough validation of the proposed approach. Our objective is, on one hand, to identify GB phases at a lower energy than those already reported and/or in better agreement with available experimental data. On the other hand, we want to collect comprehensive information on recurrent patterns in low-energy interface reconstructions for silicon and use these patterns to build a systematic classification of Si GBs. We also want to check the stability of the obtained low-energy structural patterns in other group-IV elementary crystals, including carbon, germanium, and tin. In the last section of this chapter, we study the electronic structures of the lowest-energy GBs to find the relation between the bonding patterns and the electrically active GB states.

Chapter 5 focuses on the graphitizations at diamond interfaces. This study is motivated by the studies of diamond-graphite composite nanostructures that such hybrid structures exhibit interesting properties both mechanically and electronically [19–25]. Thus, a systematical study of diamond-graphite structures is essential to understand the mechanism of transition between diamond and graphite. Our objective is to identify different diamond-graphite

phases at low energy and collect comprehensive information on graphitizations at different interfaces in the diamond.

In addition to the interfaces, the point defects are also of great importance in materials that the technological applications of semiconductors are extremely sensitive to the presence of defects. They can be seriously hindered, or sometimes even enabled, by the defects. In cubic diamond, the defects have already been widely studied both experimentally and theoretically. In fact, there is a detailed knowledge of which point defects are likely to exist in cubic silicon, their electronic properties, and their influence on functioning optoelectronic devices [26]. However, for its hexagonal counterpart, the Lonsdaleite silicon, that knowledge is still to a large extent lacking. Therefore, in Chapter 6 we move our study of interfaces to the point defects in hexagonal silicon. I will present the lowest-energy defects found in hexagonal silicon, and compare them with all known defects in cubic silicon. Furthermore, the electronic structures are also investigated to determine how the electronic density of states of hexagonal group-IV crystals will be affected by the defects.

Finally, Chapter 7 presents a summary and conclusions of the main results of this thesis.

Chapter 2

Theoretical Background

The many-body problem has bothered scientists for a long time. Thanks to the density-functional theory (awarded the Nobel Prize in chemistry in 1998), providing us a simpler way to deal with this problem with proper approximations.

In this chapter, we introduce the basic concepts of Kohn-Sham density-functional theory (DFT) in Sec. 2.1, and in the Sec. 2.2, we present a description of density-functional tight-binding (DFTB). In the last part, Sec. 2.3, the basic knowledge of grain boundaries is introduced for the reader to better understand the results of this work.

2.1 Density Functional Theory

Quantum properties of a many-body system are determined by the Hamiltonian of all the particles. Let us consider a system with K atoms and N electrons. The Hamiltonian \hat{H} can be written as

$$\hat{H} = \hat{T}_n + \hat{T}_e + \hat{V}_{nn} + \hat{V}_{ne} + \hat{V}_{ee}, \quad (2.1)$$

where \hat{T}_n and \hat{T}_e represent the kinetic energy of the nuclei and electrons, respectively:

$$\hat{T}_n = \sum_{\alpha=1}^K -\frac{\hbar^2}{2M_\alpha} \nabla_{\mathbf{R}_\alpha}^2, \quad \hat{T}_e = \sum_{i=1}^N -\frac{\hbar^2}{2m} \nabla_{\mathbf{r}_i}^2, \quad (2.2)$$

\mathbf{R}_α and \mathbf{r}_i denote the Cartesian coordinates of nucleus α with mass M_α and electron i with mass m , respectively. $\nabla_{\mathbf{R}_\alpha}^2$ and $\nabla_{\mathbf{r}_i}^2$ are the Laplacian operators. The interaction among the nuclei \hat{V}_{nn} and among the electrons \hat{V}_{ee} are:

$$\hat{V}_{nn} = \sum_{\alpha, \beta=1; \alpha \neq \beta}^K \frac{1}{2} \frac{Z_\alpha Z_\beta e^2}{|\mathbf{R}_\alpha - \mathbf{R}_\beta|} \quad \text{and} \quad \hat{V}_{ee} = \sum_{i, j=1; i \neq j}^N \frac{1}{2} \frac{e^2}{|\mathbf{r}_i - \mathbf{r}_j|}, \quad (2.3)$$

respectively. $Z_\alpha e$ is the charge of nuclei, and the interaction between the nucleus and electron \hat{V}_{ne} is

$$\hat{V}_{\text{ne}} = - \sum_{\alpha=1}^K \sum_{i=1}^N \frac{Z_\alpha e^2}{|\mathbf{R}_\alpha - \mathbf{r}_i|}. \quad (2.4)$$

Since the huge difference between the mass of nuclei and electrons, $m \ll M_\alpha$. The positions of the nuclei are treated as parameters of the Hamiltonian. This is achieved by the *Born-Oppenheimer approximation* [27]. The nuclei terms \hat{T}_{n} and \hat{V}_{nn} in \hat{H} are taken as constants, so that we are focusing on the parts related to electrons. The interactions between nuclei and electrons \hat{V}_{ne} is treated as external potential $\hat{V}_{\text{ext}}(\mathbf{r}_i)$ in the Hamiltonian

$$\hat{H} = \hat{T}_{\text{e}} + \hat{V}_{\text{ee}} + \hat{V}_{\text{ext}} \quad \text{with} \quad \hat{V}_{\text{ext}}(\mathbf{r}_i) = \sum_{i=1}^N v_{\text{ext}}(\mathbf{r}_i), \quad (2.5)$$

where $v_{\text{ext}}(\mathbf{r}_i) = \sum_{\alpha=1}^K \frac{-Z_\alpha e^2}{|\mathbf{R}_\alpha - \mathbf{r}_i|}$. With the Hamiltonian, the ground-state wavefunction Ψ_0 can be obtained by solving the Schrödinger equation:

$$\hat{H}\Psi_0(\mathbf{r}_1, \dots, \mathbf{r}_N) = E_0\Psi_0(\mathbf{r}_1, \dots, \mathbf{r}_N), \quad (2.6)$$

However, it is difficult to solve Eq. 2.6, due to the high dimensionality, where the many-body wavefunction is depending on $N * 3$ spatial variables. Approximated approaches are necessary to have solutions as close as possible to the accurate ones. And the density functional theory (DFT) is an exceptional way to solve this problem.

2.1.1 Hohenberg-Kohn Theorem

To introduce DFT, the Hohenberg-Kohn (HK) theorem [28] is always the beginning of the story. It ensures the many-body system can be characterized by the electron density $n_{\mathbf{r}}$ and the relation between $n_{\mathbf{r}}$ and the ground-state wavefunction. The first Hohenberg-Kohn (HK) theorem states that the external potential $v_{\text{ext}}(\mathbf{r})$, with an additive constant, is determined uniquely by the the ground state electronic density $n_0(\mathbf{r})$, which implies that

$$v_{\text{ext}}(\mathbf{r}) = v_{\text{ext}}[n_0(\mathbf{r})]. \quad (2.7)$$

Since there is a one-to-one correspondence between the external potential v_{ext} and the corresponding ground-state wavefunction $\Psi_0(\mathbf{r})$ which is obtained from solving the Schrödinger

equation, $\Psi_0(\mathbf{r})$ is also a functional of $n_0(\mathbf{r})$,

$$\Psi_0(\mathbf{r}) = \Psi[n_0(\mathbf{r})]. \quad (2.8)$$

For any observable $\hat{O}(\mathbf{r})$ of the system, the expectation value of $\hat{O}(\mathbf{r})$ at ground state $\Psi_0(\mathbf{r})$ is also a functional of $n_0(\mathbf{r})$,

$$\hat{O}[n_0(\mathbf{r})] = \langle \Psi[n_0(\mathbf{r})] | \hat{O} | \Psi[n_0(\mathbf{r})] \rangle. \quad (2.9)$$

Particularly, the ground-state energy is a density functional

$$\begin{aligned} E[n_0(\mathbf{r})] &= \langle \Psi[n_0(\mathbf{r})] | \hat{T} + \hat{V}_{ee} + \hat{V}_{\text{ext}} | \Psi[n_0(\mathbf{r})] \rangle \\ &= F_{\text{HK}}[n] + \int d^3r n_0(\mathbf{r}) v_{\text{ext}}(\mathbf{r}), \end{aligned} \quad (2.10)$$

where

$$F_{\text{HK}} = T[n] + V_{ee}[n], \quad (2.11)$$

which is an universal functional and only dependent on the density $n(\mathbf{r})$.

The second Hohenberg-Kohn theorem states that for a given v_{ext} , minimizing the energy functional gives the ground-state energy of the system, and the functional is minimized only by the true ground-state density $n_0(\mathbf{r})$:

$$E_0 = \min_{\{n\}} E_{v_{\text{ext}}}[n], \quad (2.12)$$

which can also be written by the variational principle with a Euler-Lagrange equation:

$$\frac{\delta}{\delta n(\mathbf{r})} [E_{v_{\text{ext}}}[n] - \mu (\int d^3r n(\mathbf{r}) - N)] = \frac{\delta F_{\text{HK}}[n]}{\delta n(\mathbf{r})} + v_{\text{ext}}(\mathbf{r}) - \mu = 0 \quad (2.13)$$

where μ is the Lagrange multiplier and the subsidiary condition is required to ensure the proper normalization of the density. The exact ground-state of the system can be obtained by solving Eq 2.13. Unfortunately, the explicit form of F_{HK} still remains unknown. In this section we have briefly introduced the HK-theorem and the proof part is skipped, for any reader who is interested in the details, there are several DFT books that can be good references [29–32].

2.1.2 Kohn-Sham Equations

The Kohn-Sham (KS) system is an auxiliary system of non-interacting particles with the same density as the physical system. To introduce the KS equations, we start from the Hamiltonian of a non-interacting system with a multiplicative external potential $v_s(\mathbf{r})$,

$$\hat{H}_s = \hat{T} + \hat{V}_s(\mathbf{r}), \quad \hat{V}_s = \int d^3r n(\mathbf{r})v_s(\mathbf{r}) \quad (2.14)$$

with

$$\hat{H}_s|\Phi_0\rangle = [\hat{T} + V_s(\mathbf{r})]|\Phi_0\rangle = E_{s,0}|\Phi_0\rangle \quad (2.15)$$

To satisfy the Pauli principle, the non-degenerate ground state $|\Psi_0\rangle$ is a Slater determinant,

$$\Phi_0(\mathbf{r}_1\sigma_1, \dots, \mathbf{r}_N\sigma_N) = \frac{1}{\sqrt{N!}} \det \begin{pmatrix} \phi_1(\mathbf{r}_1\sigma_1) & \dots & \phi_N(\mathbf{r}_1\sigma_1) \\ \vdots & & \vdots \\ \phi_1(\mathbf{r}_N\sigma_N) & \dots & \phi_N(\mathbf{r}_N\sigma_N) \end{pmatrix} \quad (2.16)$$

ϕ_i are orbitals satisfying the one-particle Schrödinger equation

$$\left\{ -\frac{\hbar^2}{2m} \nabla^2 + v_s \right\} \phi_i(\mathbf{r}\sigma) = \varepsilon_i \phi_i(\mathbf{r}\sigma). \quad (2.17)$$

The variable σ represents the spin degree of freedom. The ground-state wavefunction of such a non-interacting system is a unique functional of the ground state density, i.e.,

$$|\Phi[n(\mathbf{r})]\rangle \quad \text{with} \quad |\Phi_0\rangle = |\Phi[n_0(\mathbf{r})]\rangle, \quad (2.18)$$

and

$$n(\mathbf{r}) = \sum_{i=1}^N |\phi_i(r)|^2. \quad (2.19)$$

Eq. 2.17 and 2.19 are called the KS equations. The HK ground-state energy functional of the non-interacting system can be defined as:

$$E_s[n] = \langle \Phi[n] | \hat{T} + \hat{V}_s | \Phi[n] \rangle = T_s + \int d^3r n(\mathbf{r})v_s(\mathbf{r}),$$

where $T_s = \langle \Phi[n] | \hat{T} | \Phi[n] \rangle$. The total energy $E[n]$ is written as

$$\begin{aligned} E[n] &= T[n] + E_{ee}[n] + E_{\text{ext}}[n] \\ &= T[n] + E_{ee}[n] + E_{\text{ext}}[n] + T_s[n] + E_H[n] - T_s[n] - E_H[n] \\ &= T_s[n] + E_{\text{ext}}[n] + E_H[n] + E_{xc}[n], \end{aligned} \quad (2.20)$$

where the functional $E_H[n]$ is the classical (Hartree) interaction energy between the particles with density $n(\mathbf{r})$,

$$E_H[n] = \frac{1}{2} \int \int d^3r d^3r' \frac{n(\mathbf{r})n(\mathbf{r}')}{|\mathbf{r} - \mathbf{r}'|}. \quad (2.21)$$

The last term of Eq. 2.20, $E_{xc}[n] = F_{\text{HK}}[n] - T_s[n] - E_H[n]$, is defined as the exchange-correlation (xc) energy functional, and $F_{\text{HK}}[n] = T[n] + V_{ee}[n]$. All the complicated many-body effects not contained in T_s , E_H and E_{ext} are absorbed in E_{xc} .

2.1.3 Exchange-Correlation Energy Functionals

The Kohn-Sham equations 2.17 give the exact density of the physical system, and the complicated many-body Schrödinger equation is converted to a set of single-particle equations which are much easier to solve. Unfortunately, the term $E_{xc}[n]$ in Eq. 2.20 is still hard to handle. Thus, an appropriate approximation of E_{xc} is indispensable for solving the KS equations, which will be discussed in this part. E_{xc} is usually decomposed into an exchange part E_x and a correlation part E_c ,

$$E_{xc} = E_x + E_c. \quad (2.22)$$

The standard definition [33, 34] of the exchange energy functional in DFT is

$$E_x[n] = \langle \Phi_0[n] | \hat{V}_{ee} | \Phi_0[n] \rangle - E_H[n]. \quad (2.23)$$

The correlation energy $E_c[n]$ is written as

$$E_c = \langle \Psi_0[n] | \hat{H} | \Psi_0[n] \rangle - \langle \Phi_0[n] | \hat{H} | \Phi_0[n] \rangle, \quad (2.24)$$

where $|\Psi_0[n]\rangle$ is the true ground-state wavefunction of the interacting system and $|\Phi_0[n]\rangle$ is the Kohn-Sham wavefunction.

In practice, the exact form of E_{xc} is unknown and it has to be approximated. Perdew and Schmidt described a ladder of approximations for E_{xc} , which is called ‘‘Jacob’s ladder’’ [35]. At the lowest rung of this ladder is the local density approximation (LDA) [36]. In LDA, the system is treated locally as a homogeneous electron gas, where the interacting electrons are

in an infinite region of space with a uniform positive external potential, that neutralizes the charge of the electrons.

In LDA we assume a spin-unpolarized system. For actual applications, the spin polarization should be taken into consideration. Thus, the more popular local spin density (LSD) approximation is introduced. The LSD exchange energy formula is

$$E_{xc}^{\text{LSD}}[n_{\uparrow}, n_{\downarrow}] = \int d^3r n(\mathbf{r}) \epsilon_{xc}(n_{\uparrow}(\mathbf{r}), n_{\downarrow}(\mathbf{r})), \quad (2.25)$$

where $e_{xc}(n_{\uparrow}(\mathbf{r}), n_{\downarrow}(\mathbf{r}))$ is the exchange-correlation energy per particle for the homogeneous electron gas of spin densities n_{\uparrow} and n_{\downarrow} [37–39].

To correct the formal features of LSD, generalized-gradient approximations (GGA) are proposed, which is one of the most popular methods to describe the exchange-correlation energy in computational physics. The general formula is

$$E_{xc}^{\text{GGA}}[n_{\uparrow}, n_{\downarrow}] = \int d^3r n(\mathbf{r}) \epsilon_{xc}^{\text{GGA}}(n_{\uparrow}, n_{\downarrow}, \nabla n_{\uparrow}, \nabla n_{\downarrow}). \quad (2.26)$$

It can be treated as an extension of LSD, but taking the gradients of the density $n(\mathbf{r})$ into consideration. The functional $\epsilon_{xc}^{\text{GGA}}(n_{\uparrow}, n_{\downarrow}, \nabla n_{\uparrow}, \nabla n_{\downarrow})$ is not unique in the form. It depends on different constraint methods. The most used GGA exchange functional nowadays in computational physics was proposed by Perdew, Burke, and Ernzerhof (PBE) [40].

Beyond the GGA we have the meta-GGAs. Compared to the form of GGA in Eq. 2.26, meta-GGAs take the more general form

$$E_{xc}^{\text{mGGA}}[n_{\uparrow}, n_{\downarrow}] = \int d^3r n(\mathbf{r}) \epsilon_{xc}^{\text{mGGA}}(n_{\uparrow}, n_{\downarrow}, \nabla n_{\uparrow}, \nabla n_{\downarrow}, \nabla^2 n_{\uparrow}, \nabla^2 n_{\downarrow}, \tau_{\uparrow}, \tau_{\downarrow}). \quad (2.27)$$

The most obvious variable meta-GGAs is the second-order gradient correction $\nabla^2 n$ for previous approximations and the Kohn-Sham orbital kinetic energy density for electrons of spin σ

$$\tau_{\sigma}(\mathbf{r}) = \frac{1}{2} \sum_k |\nabla \phi_{k\sigma}(\mathbf{r})|^2. \quad (2.28)$$

Several meta-GGAs have been constructed by a combination of theoretical constraints and fitting to chemical data [41–46]. The modified Becke-Johnson (mBJ) [46] approximation is one notable example of them. The mBJ potential is a local approximation to an atomic exact-exchange potential plus a screening term,

$$v_{x,\sigma}^{\text{mBJ}}(\mathbf{r}) = cv_{x,\sigma}^{\text{BR}}(\mathbf{r}) + (3c - 2) \frac{1}{\pi} \sqrt{\frac{5}{12}} \sqrt{\frac{2\tau_{\sigma}(\mathbf{r})}{n(\mathbf{r})}}, \quad (2.29)$$

where $v_{x,\sigma}^{\text{BR}}(\mathbf{r})$ is the Becke-Roussel potential [47] and the density dependent parameter c :

$$c = \alpha + \beta \left(\frac{1}{V_{\text{cell}}} \int_{\text{cell}} \frac{|\nabla n(\mathbf{r})|}{n(\mathbf{r})} \right)^{1/2}. \quad (2.30)$$

V_{cell} is the unit cell volume, α and β are two dimensionless parameters with the default values of -0.012 and 1.023 bohr^{1/2} according to a fit to experimental results [48]. This functional is rather excellent for calculating band gaps of semiconductors and insulators [48, 49].

2.2 Density Functional Tight-Binding

DFT is successful in accurately calculating the energy and electronic structures for different systems, but for large atomic structures which contain from hundreds of atoms up to tens of thousands of atoms, the cost of computational resources increases exponentially and the time consumption is rather large.

Density functional tight-binding (DFTB) [50, 51] method is a good choice for dealing with such large systems. One major aspect of DFTB is that the Kohn-Sham energy for the real system of density $n(\mathbf{r})$ is taken as an expansion of $n(\mathbf{r})$ around a reference density $n_0(\mathbf{r})$, $n(\mathbf{r}) = n_0(\mathbf{r}) + \delta n(\mathbf{r})$. It assumes that the artificial system of $n_0(\mathbf{r})$ without charge transfer is close enough to the real density such that $\delta n(\mathbf{r})$ is small. Another aspect of DFTB is that the electronic wave functions $\phi_a(\mathbf{r})$ are defined as linear combinations of minimal atomic orbital-type basis sets, $\{\varphi_\mu\}$.

$$\phi_a(\mathbf{r}) = \sum_{\mu} c_{\mu}^a \varphi_{\mu}(\mathbf{r}). \quad (2.31)$$

In DFTB the total energy E_{DFTB} is composed by three terms [52],

$$E_{\text{DFTB}} = E_{\text{BS}} + E_{\text{rep}} + E_{\text{coul}}. \quad (2.32)$$

The term E_{BS} is called band-structure energy,

$$E_{\text{BS}} = \sum_a f_a \sum_{\mu\nu} c_{\mu}^{a*} c_{\nu}^a \hat{H}_{\mu\nu}^0, \quad (2.33)$$

where

$$\hat{H}_{\mu\nu}^0 = \langle \phi_{\mu} | \hat{H}_0^{\text{KS}} | \phi_{\nu} \rangle = \langle \phi_{\mu} | -\frac{1}{2} \nabla^2 + \hat{V}_{\text{ext}}[n_0] + \hat{V}_{\text{H}}[n_0] + \hat{V}_{\text{xc}}[n_0] | \phi_{\nu} \rangle, \quad (2.34)$$

and f_a is the occupation of a single-particle state ϕ_a .

The term E_{rep} is the repulsive energy, it contains the nucleus-nucleus interaction and exchange-correlation interactions, thus it is in a complicated form,

$$E_{\text{rep}} = -\frac{1}{2} \int d^3r \hat{V}_H[n_0(\mathbf{r})]n_0(\mathbf{r}) + E_{\text{xc}}[n_0(\mathbf{r})] + V_{\text{nn}} - \int d^3r \hat{V}_{\text{xc}}[n_0(\mathbf{r})]n_0(\mathbf{r}). \quad (2.35)$$

E_{rep} can be considered as an equivalent to the exchange-correlation functional in DFT, since it absorbs the most difficult parts and is usually approximated as pairwise repulsive potential [52]

$$E_{\text{rep}} = \sum_{I < J}^{\text{nuclei}} V_{\text{rep}}^{IJ}(R_{IJ}), \quad (2.36)$$

where V_{IJ}^{rep} is the repulsive potential between atoms I and J at the inter-nuclear distance R_{IJ} .

The last term, E_{coul} , is the energy from charge fluctuations and it contains mainly the Coulomb interaction, but also the exchange-correlation contributions [52]. It includes the effects of charge transfer in hetero-nuclear systems [53],

$$E_{\text{coul}} = \frac{1}{2} \int \int d^3r d^3r' \left(\frac{\delta^2 E_{\text{xc}}[n_0]}{\delta n \delta n'} + \frac{1}{|\mathbf{r} - \mathbf{r}'|} \right). \quad (2.37)$$

By using the approach of Mulliken population analysis [54], this term can be written as

$$E_{\text{coul}} = \frac{1}{2} \sum_{IJ}^{\text{nuclei}} \gamma_{IJ}(R_{IJ}) \Delta q_I \Delta q_J, \quad (2.38)$$

where $\gamma_{IJ}(R_{IJ})$ represents the effective interaction between two spherical charge distributions, and q_I is the total number of electrons on atom I using the localized basis. $\Delta q_I = q_I - q_I^0$ are the atomic charges fluctuations, where q_I^0 is the number of valence electrons for a neutral atom.

Following the different terms written above, the final energy expression is

$$E_{\text{DFTB}} = \sum_a f_a \sum_{\mu\nu} c_{\mu}^{a*} c_{\nu}^a H_{\mu\nu}^0 + \frac{1}{2} \sum_{IJ} \gamma_{IJ}(R_{IJ}) \Delta q_I \Delta q_J + \sum_{I < J} V_{IJ}^{\text{rep}}(R_{IJ}) \quad (2.39)$$

The energy in Eq. 2.39 is minimized by variation of $\delta(E_{\text{DFTB}} - \sum_a \epsilon_a \langle \psi_a | \psi_a \rangle)$ and we obtain

$$\sum_{\nu} c_{\nu}^a \left(H_{\mu\nu}^0 + \frac{1}{2} S_{\mu\nu} \sum_K (\gamma_{IK} + \gamma_{JK}) \Delta q_K - \epsilon_a S_{\mu\nu} \right) = 0, \mu \in I, \nu \in J. \quad (2.40)$$

$S_{\mu\nu} = \langle \varphi_{\mu} | \varphi_{\nu} \rangle$ are the overlap matrix elements [52].

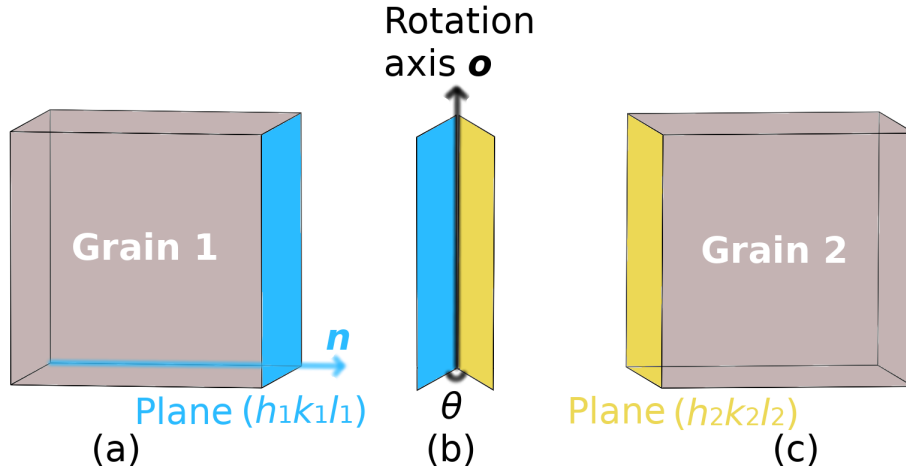


Fig. 2.1 A schematic of the composed parts of a tilt GB, panels (a) and (c) are two grains in the GB, vector n is normal to plane ($h_1k_1l_1$), which is also the boundary plane, θ is the misorientation angle between the planes ($h_1k_1l_1$) and ($h_2k_2l_2$) around the rotation axis o .

The parameters $S_{\mu\nu}$, $H_{\mu\nu}^0$ and V_{IJ}^{rep} need to be fitted to adequate datasets of DFT calculations [55] and stored in tables for future calculations to use.

2.3 Basic knowledge of grain boundaries

A grain boundary (GB) is a two-dimensional planar defect in solid crystalline materials between two portions of material with the same chemical composition and crystal structure. Inside the GB region, the atomic positions are therefore shifted from the regular sites in a perfect monocrystal [56].

The GB is usually described by five independent parameters, i.e. macroscopic degrees of freedom (DOFs), with which we can obtain the full information to build the initial structure of the GB.

Two degrees of freedom result from the orientation of the grain boundary plane between different grains and can be described by the normal vector n to this plane. Typically, this normal vector is given in terms of the Miller indices (hkl). The rotation axis o , which describes the misalignment of the grains, leads to another two degrees of freedom and is described by $[h_0k_0l_0]$. The last DOF is given by the misorientation angle θ . By these parameters, the GB is fully described (full notation: $\theta[h_0k_0l_0]\{hkl\}$).

Besides the five DOFs, GBs can be classified by the relation between the rotation axis and the boundary plane: when the rotation axis is parallel to the boundary plane, the GBs are defined as *tilt* GBs, and when the axis is perpendicular to the boundary plane they are

defined as *twist* GBs. Due to the symmetry of cubic structures, there are cases, in which the same boundary can be described by different but equivalent notations and the GBs can belong to more than one category. For example, the tilt GB $53.1^\circ[100]\{021\}$ can also be described as $36.9^\circ[100]\{021\}$. The twin tilt GB $70.5^\circ[110]\{111\}$, where two grains are in mirror symmetry, can also be obtained by a rotation of 60° or 180° around the $[111]$ axis which indicates a twist GB.

To understand the structures of GBs comprehensively, the GBs can also be classified by the symmetry of the boundary planes. When the boundary planes of adjoining grains can be defined by the same Miller indices, then the GBs are called symmetrical. GBs with different boundary planes are called asymmetrical and the notation $\theta[h_0k_0l_0]\{h_1k_1l_1\} \times \{h_2k_2l_2\}$ is used, in which $h_1k_1l_1$ and $h_2k_2l_2$ represent the Miller indices of the two asymmetrical boundary planes. For example, $38.9^\circ[110]\{111\} \times \{115\}$ describes an asymmetrical GB.

If the misorientation angles θ of GBs are larger than 15° , they are called high-angle GBs and the atomic arrangement in the boundary region can be described using the structural unit model. In contrast, low-angle GBs ($\theta < 15^\circ$) are described with the dislocation model [56]. In experimental studies of polycrystalline silicon, the most common high-angle GB is the mirror symmetrical GB $70.5^\circ[110]\{111\}$ [57, 58].

For an efficient identification of special high-angle GBs, the coincidence-site lattice (CSL) model was proposed by Kronberg and Wilson in their study of the secondary recrystallization in copper [59]. In this model, the lattice sites of one grain coincide/overlap exactly with the lattice sites of the neighboring grain and the number of bonds that are broken across the boundary is small, which leads to the high stability of GBs. A dimensionless parameter Σ is used to present the reciprocal value of the density of coincidence sites, Σ can be determined as Ref. [60]:

$$\Sigma = \frac{\text{number of coincidence sites in an elementary cell}}{\text{total number of all lattice sites in an elementary cell}} \quad (2.41)$$

Σ is an important parameter for characterizing the CSL model. It depends not only on the misorientation angle but also on the Miller indices of the boundary planes in tilt symmetrical GBs. The value of Σ can be simply calculated as [56]:

$$\Sigma = \begin{cases} h^2 + k^2 + l^2 & \text{if } (h^2 + k^2 + l^2) \text{ is odd} \\ 0.5 * (h^2 + k^2 + l^2) & \text{if } (h^2 + k^2 + l^2) \text{ is even} \end{cases} \quad (2.42)$$

For example, the Σ of $53.1^\circ[100]\{021\}$ GB is $\Sigma = 2^2 + 1^2 = 5$, and of $36.9^\circ[100]\{031\}$ GB is $\Sigma = 0.5 * (3^2 + 1^2) = 5$. The two GBs can be written within the CSL model as $\Sigma 5[100]\{021\}$ and $\Sigma 5[100]\{031\}$, respectively.

The smallest possible value of Σ equals 1: in this situation, all the coincidence sites are overlapping with the atomic position of the perfect crystal, i.e. $\Sigma = 1$ indicates a perfect crystal (no GB). In experiments, the most observed GBs in bcc and fcc structures are the twin GBs with the value $\Sigma = 3$. Various studies, in both experiments and theories, suggest that the GBs with a low value of Σ usually correspond to special GBs. In our studies on silicon, we thus consider CSLs with $\Sigma \leq 29$. These structures display a significant variety of starting interface configurations and have often been detected in experimental samples, where the most frequently encountered GBs are the energetically favored CSLs of $\Sigma 3$, $\Sigma 9$ and $\Sigma 27$ [61, 58, 62, 63].

Chapter 3

Constrained structural prediction approaches and computational details

The development of reliable approaches for crystal structure prediction has brought much convenience to the discoveries and studies of new materials. It is a challenging open problem of materials science for predicting microscopic atomic structures of internal reconstructions, and the determination of their effects on the electronic properties of a multicomponent material.

In this chapter, we first briefly review the methods of interface structural predictions in current literature in Sec. 3.1. Then, in Sec. 3.2, our constrained structural prediction approaches are introduced in detail. Finally, in Sec. 3.3, we present the computational details in different systems which are investigated using our approaches.

3.1 Interface structure prediction

In the past years, various approaches have been proposed for predicting the interface structures [64–75]. The introduction of genetic algorithms for the prediction of interface reconstructions [67, 68] represented a significant advance. Zhang *et al.* [67] combined a genetic algorithm with classical molecular dynamics and tight-binding to study silicon GBs. The use of quantum tight-binding methods led to substantial improvement of the reliability of calculations, as classical potentials are often inaccurate, and sometimes even qualitatively wrong [70, 73] when it comes to sampling the complex multi-dimensional potential energy surface. Chua *et al.* [68] developed a genetic algorithm to study both stoichiometric and non-stoichiometric GBs of SrTiO₃. Due to the high computational cost, classical interatomic potentials were preferred to carry out this work [68]. More recently, algorithms

and codes developed for structural prediction of bulk materials were adapted to tackle the challenging problem of predicting interface reconstructions. Zhu *et al.* [74] extended US-PEX [76, 77], a well-established and robust crystal structure prediction code, to the structural prediction of interfaces. In their seminal work [74], they combined evolutionary search and classical molecular dynamics, boosted by machine learning post-processing analysis, to uncover an unexpected rich polymorphism of Cu tilt GBs [69, 72, 74]. Genetic algorithms together with classical potentials were similarly successfully employed to investigate GBs in SrTiO₃ [68, 78] and symmetric tilt and twist GBs in elementary body-centered cubic metals [79]. The reduced computational cost provided by the use of classical potentials enabled the reconstruction and classification of a large set of boundaries, accounting for variable atomic densities at the interface. Similar low-energy reconstruction patterns were also determined in other metallic GBs, combining structural relaxation using classical potentials with Monte Carlo probabilities of atom addition or removal [80].

The stabilizing effect of a reduced atomic density at the interface had already been discussed in early studies on twist GBs in ionic oxides by Tasker and Duffy [81]. Concerning specifically GBs in silicon, this important issue was stressed by Von Alfthan *et al.* [64–66]. Using classical molecular dynamics, they revealed low-energy configurations with a higher degree of structural diversity by varying the number of atoms in the interface region. DFT GB energies were then calculated *a posteriori*. In view of those findings, previous simulations of GBs in silicon that did not consider variable atomic densities at the interface were disputed.

Gao *et al.* [75] have recently adapted the particle swarm method for crystal structure prediction to determine GB reconstructions, presenting applications for graphene and rutile TiO₂ [75]. Bonding constraints were imposed to generate better starting structures and DFTB was used to obtain energies and forces. As standard Slater-Koster parameters provided by the DFTB+ distributions [82] were adopted, the less accurate tight-binding calculations were complemented by DFT reoptimization of the lowest-energy structures. The addition and removal of atoms in the interface region during structural prediction were not considered.

Random structure searching for interfaces was proposed by Schusteritsch and Pickard [71]. This method relies on the repeated generation of random atomic positions in the vicinity of an interface, respecting efficient constraints, followed by relaxations using DFT energies and forces. Results for GBs in graphene and SrTiO₃ were discussed in both stoichiometric and non-stoichiometric conditions. The computational cost involved, especially for the three-dimensional system, was considerable, and in fact, only one tilt GB (the $\Sigma 3(111)$) was discussed in this work. Moreover, to ease the computational burden, a structural search was performed using coarse parameters and soft pseudopotentials, and only the relevant structures were refined by final accurate calculations.

All in all, a comparison of the different technical choices underlying these multiple studies brings to light complementary insight on the mechanisms of interface reconstruction. We can learn important lessons from the analysis of previous literature. First of all, varying the atomic density at the interface is a key step. In fact, some thermodynamic states that are accessed in real systems by a diffusion process, can be simulated in a supercell model only by removing or adding atoms. Significant deviations from DFT results have been demonstrated for calculations using classical potentials for silicon [83]. It is also known that force fields are not capable to stabilize the lowest energy point defect in silicon [84]. A recent comparison with DFT results for a large dataset also shows that forces calculated with Stillinger-Weber or Tersoff force fields are of poor quality, both in magnitude and in direction [85], pointing to the need for a quantum-mechanical description of energies and forces. However, DFT calculations remain too costly, and different strategies for computational efficiency need to be followed to ensure the accuracy of quantum *ab initio* calculations of energies and forces, as well as the possibility to access large families of interfaces. In this work, we use tight-binding parameters optimized to reproduce a large dataset of DFT calculations that guarantee a good sampling of the potential energy surface and yield DFT quality energy and forces [55].

3.2 Constrained structural prediction approaches

Our constrained structural prediction approach is implemented in the framework of the minima hopping method (MHM), which is developed by S. Goedecker and M. Amsler [86, 87]. MHM is an efficient structural prediction algorithm designed to determine the low energy crystal structures of a system given solely its chemical composition.

In MHM, the potential energy surface is explored using a sequence of local geometry optimization steps, followed by molecular dynamics steps in order to allow the system to escape from local minima. In the molecular dynamics steps, the direction of the initial velocities is chosen through a softening procedure. This returns the direction of a low potential barrier, which, according to the Bell-Evan-Polanyi principle [88, 89], is likely to lead to a lower minimum. This new minimum can, after optimization, be accepted or not, depending on whether the energy difference to the previous minimum is below or above a certain threshold. The latter is dynamically adapted to obtain an acceptance rate of approximately 50%. The predictive power of this approach was already demonstrated in a wide set of applications, ranging from bulk crystals [90] to low-density structures [91], crystals with defects [92], quasi two-dimensional materials [93], etc.

Most often, structural prediction using the MHM is performed calculating energy and forces from first-principles using density functional theory (DFT). This is clearly the preferred

method as DFT allows for the study of the whole periodic table with good accuracy. However, as the number of atoms in the unit cell (and, consequently, the number of local minima of the enthalpy surface) grows, DFT simulations become prohibitively long. This is certainly the case for our unit cells containing several hundred atoms. When good parametrizations are available, the DFTB scheme as implemented in the DFTB+ package [82] has proved to be a valuable alternative for global structural prediction studies [91–95]. Tight binding combines the advantages of a fully quantum approach with a moderate computational cost. We used the tight-binding parameters developed by Huran *et al.* [55], which are designed to guarantee an accurate evaluation of both energy and forces for group-IV compounds. The fitting procedure includes the generation of unbiased training sets and subsequent optimization of the parameters using a pattern search method. The DFT data sets are designed to encompass a wide range of crystal structures characteristic of different atomic arrangements that can appear in structural prediction simulations. As a target for the optimization, it is required that the formation energy and the forces on the atoms calculated within tight-binding reproduce the ones obtained using density-functional theory. An extensive test of these parameters is reported in Ref. [55].

For a fully reliable interpretation of the results, the final structures are always refined at the DFT level using the VASP [96–98] code with the Perdew-Burke-Ernzerhof (PBE) exchange-correlation functional [40]. Despite the well-known limitations of the PBE functional for calculation of formation enthalpies, with errors usually at the level of ~ 0.2 eV/atom for dissimilar chemistries, we can rely on strong error cancellations when considering chemically similar phases [99]. In the specific case of silicon polymorphs, the reliability of PBE calculations to predict phase stability has been proven by previous works [100, 91].

3.2.1 Approach for interface reconstructions

For the simulations of lowest-energy interface reconstruction, the implementation of the constraints is explained as follows: we build a supercell that contains the interface we want to study, as shown in Fig. 3.1. Such supercell is flexible for different studies that the structure can either contain the grain boundary or interface. The atoms of the supercell are separated into two sets, namely those belonging to the bulk regions and the ones making part of the interface. Considering the variation of volume during the structural reconstruction, we add a vacuum layer between the two bulk regions as depicted in Fig. 3.1, while the periodic boundary conditions are maintained parallel to the interface plane. The thickness of the vacuum layer should be large enough to eliminate the interaction between the two separated bulk parts. The thickness of bulk regions also needs to be sufficiently large to avoid the effects from the free surfaces of bulk regions.

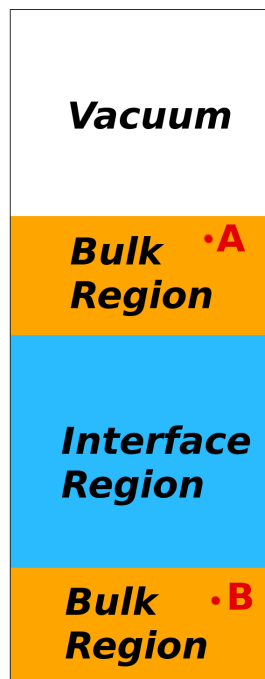


Fig. 3.1 A schematic of a starting supercell for the reconstruction of an interface. The constrained parts are indicated by orange rectangles, while the blue rectangle indicates the interface region, and their atomic positions are optimized during the MHM simulations. Atoms A and B are highlighted in red as they are mentioned in the text.

The relative positions of the bulk-like atoms (orange regions in Fig. 3.1) are fixed, so that the bulk regions behave like rigid bodies. This is achieved by imposing the conditions [101]

$$\mathbf{F}_n - \mathbf{F}_m = 0, \quad (3.1)$$

where n and m run over pairs of atoms in each bulk region. Then we choose in the top and bottom bulk layers, respectively, one atom A and one atom B (red atoms in Fig. 3.1). In the top bulk region, we imposed Eq. 3.1 to all pairs of atoms containing atom A, while in the bottom bulk region we impose the same constraint to all pairs containing atom B. We obtain therefore $N - 1$ equations per layer, where N is the number of atoms composing each bulk layer. This kind of constraint is clearly more physical than fixing each single atomic position to the perfect crystalline bulk, as the bulk layer can move as a whole, allowing for the minimization of the strain on the atoms at the interface during their reconstruction. In the (blue) interface region, all atomic coordinates are fully optimized. Note that, during the MHM calculations, the supercell lattice parameters are always kept fixed while the atomic positions are relaxed.

These constraints can also be easily applied to the study of surface reconstruction. We only need to eliminate the constrained condition in the top bulk region and impose Eq. 3.1 between atom B and the atoms of the interface region. Under this constraint, the atoms of the top bulk region will be optimized, while the bottom and interface regions are maintained as bulk.

Our approach also allows for variable atomic densities close to the interface. We observe that in many cases the lowest-energy reconstruction is attained only after adding (or removing) atoms to (from) the interface region. We remark that we tested systematically all possible modifications of the atomic density, until reaching a configuration equivalent to the starting one, differing by the simple addition of a full atomic plane.

3.2.2 Approach for point defects

For the geometrical prediction of point defects in a bulk crystal, we adjust the constraint conditions in the reconstructions of interfaces. Our procedure is the following: (i) we build a supercell of the parent compound large enough to include the defect plus a buffer region, as shown in Fig. 3.2. (ii) We select the atoms within a slab in each Cartesian direction and fix them to their equilibrium coordinates. For the purposes of the algorithm, this buffer region should be thick enough to represent the bulk of corresponding crystals, while the volume inscribed (atoms in green part in Fig. 3.2) should be large enough to contain the point defects. We also fix the lattice vectors. (iii) We may add or remove atoms from the green region, in

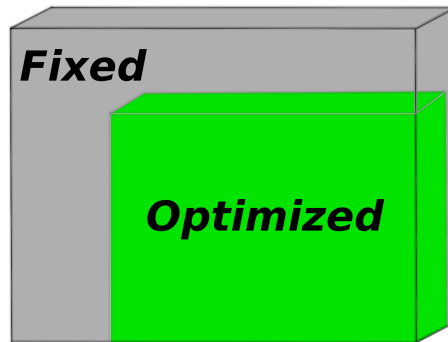


Fig. 3.2 A Schematic of starting supercell for the reconstruction of point defect in a bulk crystal. During the MHM simulations, the atoms in the gray part are fixed, while the atomic positions in the green part are optimized.

case we want to study interstitials or vacancies. (iv) We perform MHM simulations obeying the above constraints. These yield as the lowest possible structure the bulk phase, while metastable structures represent point defects.

Due to the geometrical constraints, it turns out that the same point defect located in different positions of the green region will have slightly different energies as a consequence of the different strains imposed by the fixed atoms. As such, they will likely be misidentified by the global structural prediction algorithm as different defects. To resolve this issue, we perform an extra step in our methodology: (v) We eliminate the constraints on the atoms (while still keeping the lattice vectors fixed) and perform a re-optimization of the geometry.

The process of defect creation stems from the competition between the minimum internal energy of the ideal crystal and the stabilizing effect of entropy related to the disorder introduced by defect creation. Formally, the Gibbs' free energy of formation of a defect is given at temperature T and pressure P by the sum of the formation enthalpy and the entropic term $T\Delta S$. We can however safely rely on the formation energy only to obtain the geometry of the lowest-energy isolated defects. First of all, we are interested in single isolated defects. The variation of volume due to the creation of a point defect is negligible in the dilute case and the formation enthalpy can be approximated by the internal energy only. The entropic term can be split in the contributions of configurational entropy and phonons. The configurational entropy contribution to the free energy of alloys cannot be neglected, but in the case of a diluted defect (i.e., if the defect concentration is close to zero) the entropic contribution is of the order of few meV per unit cell. The vibrational entropy also contributes to the free energy, but its inclusion has an extremely high computational cost, and it is therefore also neglected in this work.

3.3 Computational details

3.3.1 Simulations for silicon GBs

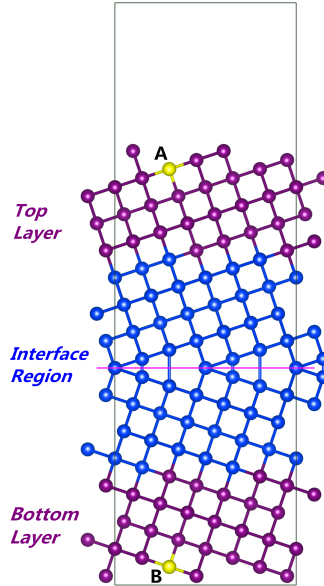


Fig. 3.3 Construction of a starting supercell containing a single $\Sigma 5(021)$ GB. We see a cut of the supercell along the axis perpendicular to the (021) boundary plane (pink line). The constrained layers are indicated by the magenta (and yellow) atoms, while blue atoms constitute the interface region and their atomic positions are optimized during the MHM simulations. Atoms A and B are highlighted in yellow as they are reference atoms for imposing the constraint conditions for the top and bottom bulk parts, respectively.

All starting geometries of grain boundaries were built using the software GB STUDIO [102], the different GBs are labeled by the introduced notation $\theta[h_0k_0l_0]\{hkl\}$ (presented in Sec. 2.3). As an illustration, we show in Fig. 3.3 the starting supercell of the $\Sigma 5(021)$ GB. In the figure, we also indicate how atoms are separated into bulk-like and interface atoms.

We run two different MHM calculations for each GB supercell from different initial interface configurations to avoid starting point biases. Note that the supercell lattice parameters are always kept fixed while the atomic positions are relaxed. After having explored more than 200 different minima, we stopped the MHM runs. Note that we tested that the lowest-lying minima evaluated during each run are independent of the chosen initial configuration.

The most promising structures (i.e. the five lowest-energy structures of each run) were then refined using VASP: the energy cutoff was set to 420 eV for silicon atoms, and for geometry optimization a $1 \times 1 \times 1$ Monkhorst-Pack \mathbf{k} -point [103] grid is selected. We then increased it to $8 \times 4 \times 1$ for accurate energy and DOS. We assured that the convergence of total

energy is better than 0.01 eV per atom. We notice that the energy ordering of the different structures with the PBE is consistent with the one of tight-binding. However, it turns out that bulk silicon is slightly over-stabilized in tight-binding, leading systematically to larger GB energies when compared to DFT. The DOS is also calculated with VASP using the PBE functional [40] and a Gaussian broadening of 0.1 eV.

The quantity that the minima-hopping algorithm must optimize is not the total energy of the supercell, but the interface energy γ , which is defined as the difference of total energy per unit area between the supercell with a GB and a supercell with the same number of atoms of crystalline silicon. It consists of the following steps. Using periodic boundary conditions, we build a starting supercell that contains two equivalent GBs. After having calculated once for all the total energy per atom μ_{Si} of bulk Si, we calculate the total energy of the unrelaxed supercell $E_{\text{unrel}}^{2\text{GB}}$ containing two equivalent GBs. We then add a vacuum layer to obtain open surfaces in the normal direction, while periodic boundary conditions are maintained parallel to the GB plane. The resulting supercell has only one GB and two surfaces separated by vacuum (see Fig. 3.3). We calculate the energy of this unrelaxed supercell with vacuum $E_{\text{unrel}}^{1\text{GB}}$. We use now the supercell with a single GB and vacuum as a starting geometry for the MHM structural prediction, obtaining $E_{\text{rel}}^{1\text{GB}}$ from the lowest-energy minimum.

The interface energy of the single unrelaxed GB is $\gamma^{\text{unrel}} = \frac{1}{2A} (E_{\text{unrel}}^{2\text{GB}} - N\mu_{\text{Si}})$, where N is the number of Si atoms in the supercell and A is the GB interface area. The surface energy of the unrelaxed interface with vacuum is $\gamma^{\text{surf}} = \frac{1}{A} [E_{\text{unrel}}^{1\text{GB}} - N\mu_{\text{Si}} - \frac{1}{2} (E_{\text{unrel}}^{2\text{GB}} - N\mu_{\text{Si}})]$. Finally, we can evaluate the relaxed GB energy as

$$\gamma = \frac{1}{A} (E_{\text{rel}}^{1\text{GB}} - M\mu_{\text{Si}}) - \gamma^{\text{surf}}, \quad (3.2)$$

where M is the number of atoms in the relaxed supercell and M can differ from N , i.e. we account for the possible change of atomic density in the interface region.

We needed, of course, to build supercells of different sizes and perform consistent convergence tests to determine the ideal number of atomic layers that allows for a valid description of an isolated interface between two bulk-like crystalline domains. In Fig. 3.3 the thickness of the bulk layer is 14 Å while the interface is 15.4 Å thick. The vacuum layer is 10 Å thick. To perform electronic structure calculations we added hydrogen atoms to saturate the Si atoms at the surface in contact with the vacuum layer. This surface passivation, used only for calculations of the DOS, prevents from having spurious surface states appearing in the band gap.

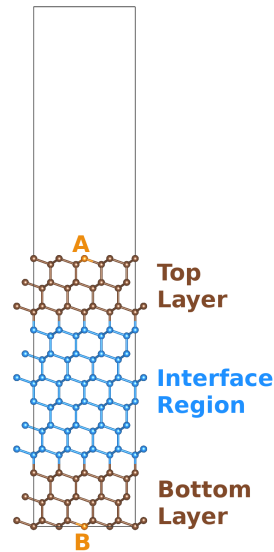


Fig. 3.4 Construction of a starting supercell containing $\{111\}$ diamond interface. The supercell is viewed along $[110]$ direction, the constrained layers are indicated by the brown (and orange) C atoms, while blue atoms constitute the interface region and their atomic positions are optimized during the MHM simulations, Atoms A and B are highlighted in orange as they are reference atoms for imposing the constraint conditions for the top and bottom bulk parts, respectively.

3.3.2 Simulations for interface reconstructions in diamond

The study of interface reconstructions in diamond is separated into two parts: the grain boundaries and the interfaces along different directions in bulk diamond. The procedure of the structural prediction follows the approach in Sec. 3.2.1, in particular, the simulations of carbon GBs are similar to the study of silicon GBs in Sec. 3.3.1.

The carbon GB supercells were built using the software GB STUDIO [102]. Then, for the interface study, we removed one of the grains to obtain a supercell composed of pure diamond with specific interface planes. As shown in Fig. 3.4, we present a supercell for the study of the $\{111\}$ interface reconstruction. During the MHM simulations, the constraint condition on the forces in Eq. 3.1 is imposed on the atoms in the top and bottom layers (the brown atoms), in which the atoms A and B (orange atoms) are taken as reference atoms for the constraints. The thickness of added vacuum is larger than those in silicon GBs (10 \AA), because of the large volume expansion during the structural reconstruction. In our study, the vacuum for carbon supercells is set from 15 to 20 \AA , the specific value depends on the size of the atomic structure.

For convenience, the supercells are labeled by the Miller indices of the interface plane. For example, the supercell with the interface of (112) diamond plane is represented as (112)

supercell. The lattice constant of the cubic diamond unit cell for constructing the supercell is $l_C=3.57 \text{ \AA}$, which is optimized with DFTB [82].

The structural prediction follows the same strategy introduced in Sec. 3.2.1. We performed four different MHM calculations for each supercell, we stopped each run after having explored more than 200 different minima. In contrast to focusing on the lowest-energy structures in Sec. 3.3.1 of Si GBs, we mainly investigate the low-energy structures composed of sp^3 - and sp^2 -hybridized carbon atoms in this part of the study.

The final structures were then refined with VASP using the PBE exchange-correlation functional [40]. The energy cutoff was set to 350 eV, we selected a $1 \times 1 \times 1$ Monkohst-Pack \mathbf{k} -point [103] grid for geometry optimization and increased it to $6 \times 6 \times 2$ for accurate energies and the DOS (with a Gaussian broadening of 0.1 eV). To saturate the C atoms at the surface contact with the vacuum layer, we added hydrogen atoms to them for the electronic structure calculations.

3.3.3 Simulations for point defects in hexagonal silicon

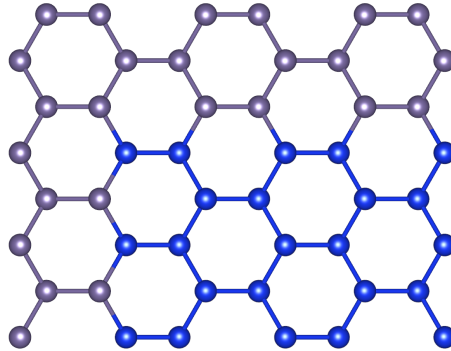


Fig. 3.5 Depiction of the (0001) surface of the constrained cell. In gray, we show the silicon atoms that are fixed and in blue the atoms that are allowed to move. Note that there is a slab of silicon atoms in the perpendicular direction that are fixed, but that is not visible in the figure.

To study the point defect in hexagonal silicon, we apply our approach presented in Sec. 3.2.2 to an orthorhombic supercell containing 288 silicon atoms (72 unit cells of the primitive hexagonal lattice) with lattice vectors $a = 15.4 \text{ \AA}$, $b = 20.0 \text{ \AA}$, and $c = 19.1 \text{ \AA}$. The supercell is depicted in Fig. 3.5, 3 layers of atoms are selected to be fixed as the bulk part, these are the atoms in gray in Fig. 3.5.

Following this procedure, we performed a series of simulations for unit cells containing one or two vacancies (-1 or -2 atoms), one or two interstitials (+1 or +2 atoms), and with

the pristine 288-atom cell. The atoms were added/removed to/from random positions in the lattice. For each case, we performed four independent minima-hopping runs, and each run was stopped after obtaining around 400 minima.

It is true that, in general, the charge state of the defect is essential to determine its thermodynamic and electronic properties. However, it was shown for cubic silicon that the vacancy is the only defect stabilized by charge, and this stabilization is rather small [104, 105]. In view of that, we concentrate in this work on neutral defects only.

To eliminate the error introduced by the use of tight-binding, we perform a final geometry optimization of all interesting geometries using VASP with PBE exchange-correlation functional [40]. In this case, we used an energy cutoff of 420 eV, and a mesh of $1 \times 1 \times 1$ \mathbf{k} -points for the geometry optimization and $4 \times 3 \times 3$ for the calculation of formation energies. This leads to a precision in the defect formation energies better than a hundredth of an eV. It is harder to estimate the intrinsic accuracy of DFT functionals in evaluating defect formation energies. In any case, we should remember that we are calculating energy differences of structures that are chemically similar, so we expect that many of the errors are likely to cancel out in this process. We remark that we do not include here any finite-size or band-edge correction, as our present aim is to predict the lowest-energy defects in hexagonal silicon, and this should be largely unaffected by these corrections.

For the analysis of the electronic structure, we employed the modified Becke-Johnson potential of Tran and Blaha [46, 48]. It is by now known that this is the best functional to calculate band gaps of semiconductors and insulators [49]. It is in fact even slightly better on average than the screened hybrid of Heyd and Scuseria from 2006 [106] at only a fraction of the computational effort. Moreover, it was shown that it yields a very good description of the hexagonal phase of silicon and germanium [107–109]. Modified Becke-Johnson has been used in the past to calculate the electronic structure of defects, for example in ZrO_2 [110], in the mixed borate–carbonate $\text{Pb}_7\text{O}(\text{OH})_3(\text{CO}_3)_3(\text{BO}_3)$ [111] or in Mg_2X ($\text{X} = \text{Si}, \text{Ge}, \text{Sn}$) [112]. The DOS calculations were performed using the tetrahedron method with a $2 \times 2 \times 2$ \mathbf{k} -point grid.

Chapter 4

Structure-property relations at silicon grain boundaries

In this chapter, we present the results of silicon GBs obtained with our constrained structural prediction approach, which has been introduced in Chapter 3, for a large and varied family of symmetric and asymmetric tilt boundaries in polycrystalline silicon (Sec. 4.1.1, Sec. 4.1.2 and Sec. 4.1.3). We find a rich polymorphism in the interface reconstructions, with recurring bonding patterns that we classify in increasing energetic order. We also compare the energy calculated with different DFTB parameterizations in Sec. 4.1.4. Then, we compare the stability of the obtained low-energy structures in different group-IV elementary crystals (Sec. 4.1.5). We also classify the grain boundaries into different types according to how the interface reconstructions are affected by removing or adding atoms at the interface region (Sec. 4.2). Finally, a clear relation between bonding patterns and electrically active grain boundary is unveiled and discussed (Sec. 4.3).

4.1 Low-energy grain boundaries

4.1.1 Grain boundaries with rotation axis [110]

In Table 4.1 we present the structures of tilt GBs with rotation axis [110] under investigation, with information on their tilt axis, misorientation angle, GB energy of the lowest-energy structures found in MHM, the total number of atoms in the supercell, and number of atoms at the interface region. An example of the reconstructed lowest-energy structure of $\Sigma 11(113)$ GB is shown in Fig. 4.1.

Our calculations indicate that almost all considered GBs present a strong reconstruction of atomic bonding at the interface, that completely modifies the initial welding of tilted

Table 4.1 Summary of the structures for GBs with rotation axis [110] studied in this work: GB labels, tilt axis, misorientation angle θ , minimum GB energy γ in J/m² after interface reconstruction, the number of atoms at the interface region N_{int} and the total number of atoms in the supercell N_{total}

| label | tilt axis | θ | γ | N_{int} | N_{total} |
|----------------------------|-----------|----------|----------|------------------|--------------------|
| $\Sigma 19\text{a}(331)$ | [110] | 26.5° | 0.339 | 104 | 160 |
| $\Sigma 27\text{a}(552)$ | [110] | 31.6° | 0.381 | 320 | 432 |
| $\Sigma 9(221)$ | [110] | 38.9° | 0.202 | 234 | 432 |
| $\Sigma 11(332)$ | [110] | 50.5° | 0.392 | 184 | 352 |
| $\Sigma 3(111)$ | [110] | 70.5° | 0.013 | 80 | 192 |
| $\Sigma 17\text{b}(334)$ | [110] | 86.6° | 0.462 | 182 | 272 |
| $\Sigma 17\text{b}(223)$ | [110] | 93.4° | 0.440 | 178 | 266 |
| $\Sigma 3(112)$ | [110] | 109.5° | 0.386 | 84 | 188 |
| $\Sigma 11(113)$ | [110] | 129.5° | 0.402 | 184 | 352 |
| $\Sigma 9(114)$ | [110] | 141.1° | 0.378 | 200 | 288 |
| $\Sigma 27\text{a}(115)$ | [110] | 148.4° | 0.623 | 204 | 428 |
| $\Sigma 19\text{a}(116)$ | [110] | 153.5° | 0.616 | 208 | 304 |
| $\Sigma 3(001 \times 221)$ | [110] | 70.5° | 0.497 | 132 | 284 |
| $\Sigma 9(111 \times 115)$ | [110] | 38.9° | 0.433 | 224 | 304 |

crystalline grains. Such reconstructions cannot be obtained by performing standard structural optimizations: a local relaxation would in fact only lead to the closest local minimum, totally ignoring the complexity of the highly-dimensional potential energy surface. An exception is the very symmetric $\Sigma 3(111)$ GB, where all silicon atoms are already conveniently bonded from the start. Not surprisingly, the reconstructed geometries always tend to eliminate dangling bonds and to bring Si–Si bond lengths and bond angles as close as possible to their value in bulk diamond silicon. For example, in Fig. 4.1 the starting interface and reconstructed interface of $\Sigma 11(113)$ GB are shown along [110] axis. The irregular gap between the two grains forms symmetric six-atom rings with atomic bonds differing from the tetrahedral bonds in bulk Si. Those bonds are formed along the [110] direction and called single atomic columns [113, 73], which will be discussed in a later part.

To label and classify the reconstructed GBs, we extend the set of structural units and the notation proposed by Papon and Petit [114]. If we draw [110] projections of the stick-and-ball models of the interface, as in Fig.4.1, we can see that sp^3 -hybridized atoms form cyclic units, whose composing rings can be labeled by the symbols $^k n_{ai}^j$. The notation is easy to interpret: n is the number of edges of the ring, i is the number of single atomic columns (see panel (a) and (b) of Fig.4.2), a indicates either a boat shape ($a = \text{“b”}$) or a nearly flat shape ($a = \text{“f”}$) in the lateral view of the bonding pattern, and j is the number of double lines (if $j = 2$, this index is omitted). A double line, which sometimes is really indicated as a double line in

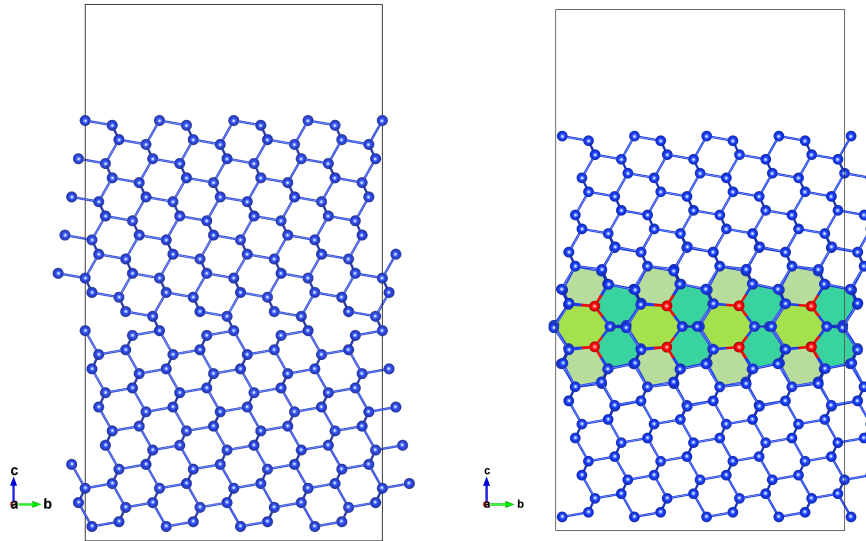


Fig. 4.1 The [110] projection of the starting structure (left panel) and the reconstructed interface (right panel) of $\Sigma 11(113)$ GB. Single-atomic columns aligned along the [110] axis, i.e. perpendicular to the view plane, are highlighted by red atoms.

the stick-and-ball model, is the bonding of an atom of the basic (110) plane with two others atoms situated in the upper and lower planes. It turned out that our simulations yielded a few extra bonding patterns that were absent in the classification of Ref. [114]. These new units are related, specifically, to the existence of silicon atoms with five-fold coordination (see panel (c) of Fig. 4.2). In view of that, we added the superscript $k = 5$ to indicate the presence of five-fold coordinated atoms in the ring. We never found, in most stable reconstructed GBs, silicon atoms with less than 4 nearest neighbors (i.e., with dangling bonds), or with more than 5 nearest neighbors. These units appear only in very high-energy configurations that are quickly dismissed by our structural prediction procedure.

A scheme of the percentage of GBs that contain a specific atomic-ring unit is shown in Fig. 4.3. We see that the most common unit is, not surprisingly, the standard bulk six-atom ring. This is followed by five-membered rings and 6_b and 6_{b1} six-membered rings. Also, 6_1 and 7_1 units appear with a high frequency. Note that 6_{b1} , 6_1 , and 7_1 rings include one single atomic column, making this particular bonding scheme rather common in our reconstructed interfaces. And the rings composed with more atoms, 8_2 and 8_{b2} rings only found in $\Sigma 27a(115)$, are accompanied with higher GB energy, as shown in Table 4.1. The GB energy of the $\Sigma 27a(115)$ reconstructed interface is higher than that of any other GB with a rotation axis of [110].

As an example, the lowest-energy GB reconstructions of the $\Sigma 3(112)$ interface and their classification using atomic-ring units are given in Fig. 4.4. The $\Sigma 3(112)$ interface is one of

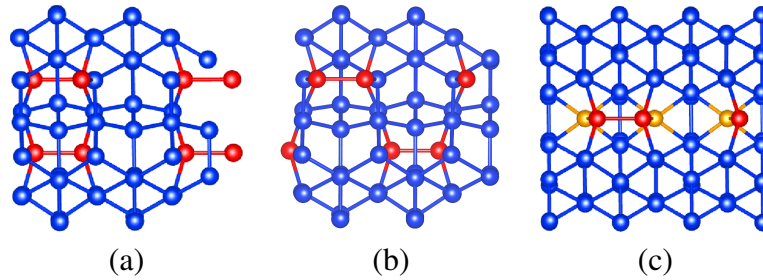


Fig. 4.2 Recurring reconstruction patterns. (a) and (b): A $[11\bar{1}]$ view of the ground state of the $\Sigma 3(112)$ GB, showing two possible types of reconstructed single atomic columns (red atoms), aligned along the $[110]$ rotation axis, the corresponding GB energy of those two patterns is 0.386 and 0.398 J/m^2 , respectively; (c) View of a $[111]$ plane of a low-energy reconstruction of the $\Sigma 3(112)$ GB with 5-coordinated silicon atoms (orange atoms) and single atomic columns (red atoms).

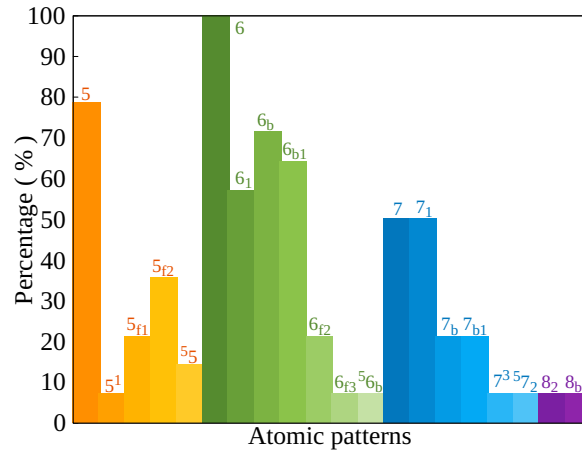


Fig. 4.3 Percentage of GBs that contain a specific atomic-ring unit. We consider the set of lowest-energy $[110]$ GBs of Table 4.2 and Table 4.3. For example, all studied structures contain six-membered rings, so their occurrence is 100%. Only $\Sigma 27a(115)$ contains 8_2 and 8_{b2} rings, and their occurrence is 7.14%.

the most studied in silicon and in germanium [113, 115]. The structure (d) is also known as the mirror-symmetric model of Ziebarth *et al.* [116], while (a) is the corresponding non-symmetric model. In agreement with Ref. [116], we conclude that the non-symmetric model is the ground-state, with a considerably lower GB energy than its symmetric counterpart. We also find that the single atomic columns have two different ways to be formed in the structure, which depends on the coordinates of bonded atoms along $[110]$ axis shown in Fig. 4.2(a) and (b), the two patterns exhibit the same structural view along $[110]$ direction, and the more symmetric pattern in panel (a) is slightly more stable than the pattern in panel (b). Moreover, we find two new reconstruction patterns with intermediate interface energies, shown in panels

(b) and (c) of Fig. 4.4. The three most stable structures exhibit two single atomic columns per unit cell (indicated by red atoms in the panels (a), (b), and (c) of Fig. 4.4), while the higher-energy symmetric model has one column plus a pair of five-fold coordinated atoms (indicated by orange balls). The initial unrelaxed cell is given for comparison in panel (f): it contains five-fold coordinated atoms and dangling bonds, which are responsible for a value of the GB energy about 1 J/m^2 larger than in the optimized ground-state structure.

In those low-energy structures of $\Sigma 3(112)$ GB in Fig. 4.4, even though they contain a variety of atomic rings, the number of single atomic columns in panel (a), (b), (c), and (e) keeps the same, with four atoms forming two columns, and in (d) the GB contains one column and a pair of five-fold coordinated atoms which also include four atoms in total. We find this is not occasional that the total number of atoms composing the single atomic column and bonded with five-fold coordination is always even (seen in Table 4.2 and 4.3), and this number is consistent in most low-energy structures of the $[110]$ GBs with misorientation angle θ exceeding 70.5° .

In Fig. 4.5, we present six low-energy structures of the $\Sigma 11(113)$ GB, where panel (a) is the ground state as we have shown in Fig. 4.1. In the structures presented in Fig. 4.5(a) and (c), there are 8 single atomic columns, which are formed by 16 atoms. In panel (c), the interface contains 7 columns plus a pair of five-fold coordinated atoms. In panel (d), the structure contains 6 columns plus two pairs of five-fold coordinated atoms. The interfaces in panels (e) and (f) contain 5 columns plus three pairs of five-fold coordinated atoms and 4 columns plus four pairs of five-fold coordinated atoms, respectively. The two sites with a single atomic column in the first 6_{f2} ring starting from left in (a) are indicated with “A” and “B”, the atomic site between them is labeled with “C” and the connecting site in the second 6_{f2} ring is “D”. In the second lowest-energy structure, shown in panel (b), the single atomic columns at “A” and “B” break. The atoms at those sites move towards the boundary plane and form zigzag bonds with the two atoms at “C”. At the same time, the atoms at “C” and “D” separate and make each atom at “C” bonded only with one atom at “D”. Then, the atoms at “D” move to each other along $[110]$ axis and form a new atomic column to ensure a fully bonded situation for the atoms. As a result, we obtain over-coordinated atoms at “C” and a new single atomic column at “D”. Another transition structure resulting from the structure in Fig. 4.5(a) is shown in panel (c), where the GB energy (0.493 J/m^2) is basically the same with structure in (b) (0.490 J/m^2), but there is no over-coordinated atom at the interface. The formation of the structure in Fig. 4.5(c) can be described as follows: The single atomic column at “A” in Fig. 4.5(a) breaks and atoms at “C” move towards “A” and away from “D”, a new single atomic column is formed between the atoms at “D”. Similarly, atoms at “C” can also move towards “B” and form an equivalent interface.

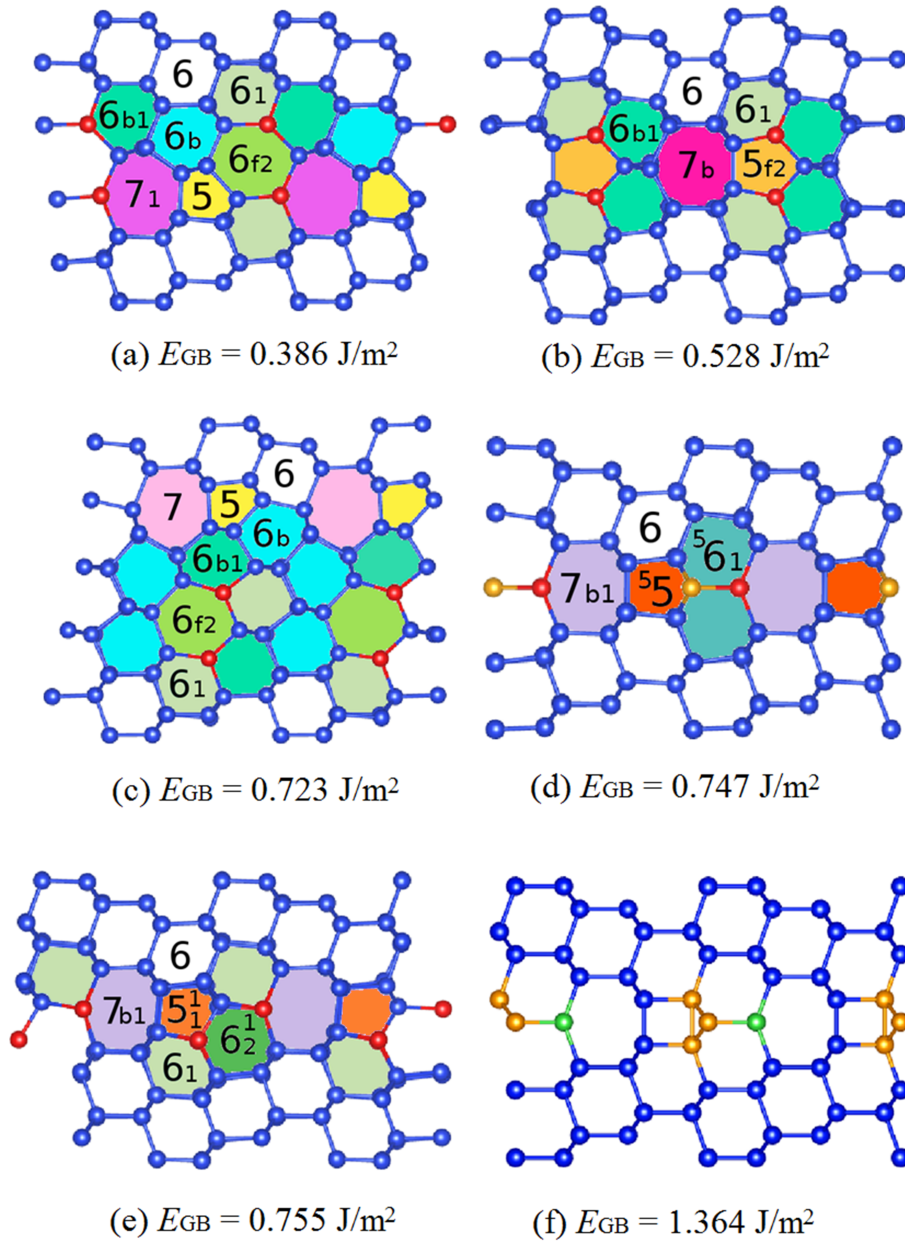


Fig. 4.4 In panels (a) to (e), we present the five lowest energy structures of the $\Sigma 3(112)$ GB. Panel (f) shows the starting structure used for the MHM simulations. For a clearer representation, we always show two unit cells along the boundary. In the figures, identical reconstructed atomic rings are filled with the same color. Red atoms form single atomic columns, orange atoms are five-fold coordinated, and green atoms have dangling bonds. We also present the GB energy and the unit atomic rings composing the interface. The same color scheme for the unit rings is used in Fig. 4.1.

In the higher-energy structures shown in Fig. 4.5(d) to (f), similar structural transition features are found, which means that two single atomic columns break and form one column at another site plus a pair of five-fold coordinated atoms. The stability of the interface decreases with the increasing proportion of five-fold coordinated atoms, as we can see from the given GB energy. For the interface in Fig. 4.5 (f), the GB energy (0.805 J/m^2) is over two times larger as for the interface in Fig. 4.5 (a) (0.391 J/m^2). Regardless the locations of the single atomic columns and over-coordinated atoms, the number of atoms involved those “new” bonds, which are different from the tetrahedral coordination in bulk silicon, always keeps the same during the transitions. This is observed in most GBs reconstructed with single atomic columns, such as $\Sigma 3(112)$ shown in Fig. 4.4, $\Sigma 9(114)$ shown in Fig. 4.6, $\Sigma 17b(334)$ shown in Fig. 4.7, $\Sigma 17b(223)$ shown in Fig. 4.8, $\Sigma 19a(116)$ shown in Fig. 4.9 and $\Sigma 27a(115)$ shown in Fig. 4.10.

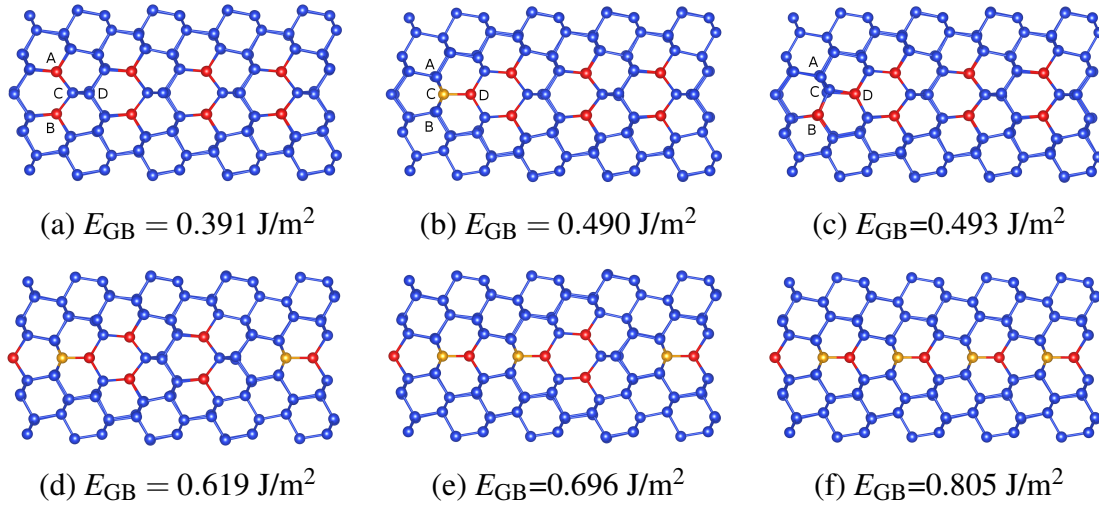


Fig. 4.5 Six low-energy interfaces of the $\Sigma 11(113)$ GB viewed along $[110]$ axis. The single atomic columns and five-fold coordinated atoms are indicated by red and orange atoms, respectively.

In general, we find that the patterns present in the reconstructed interfaces of $[110]$ GBs are highly dependent on the misorientation angle. In fact, for values of this angle up to 70.5° , low-energy reconstructions are composed of five-, six-, and seven-membered rings, without single atomic columns. This is confirmed by experiments, and it is reflected in experimentally-based models [117, 118], originally built for diamond and then extended to other group-IV elements [119]. In contrast to these models, we do not need to introduce dangling bonds to model GBs with larger angles. Our results from structural prediction show instead that at larger angles the inclusion of single atomic columns is enough to restore a four-fold coordination of all silicon atoms and to reduce bond distortions. We

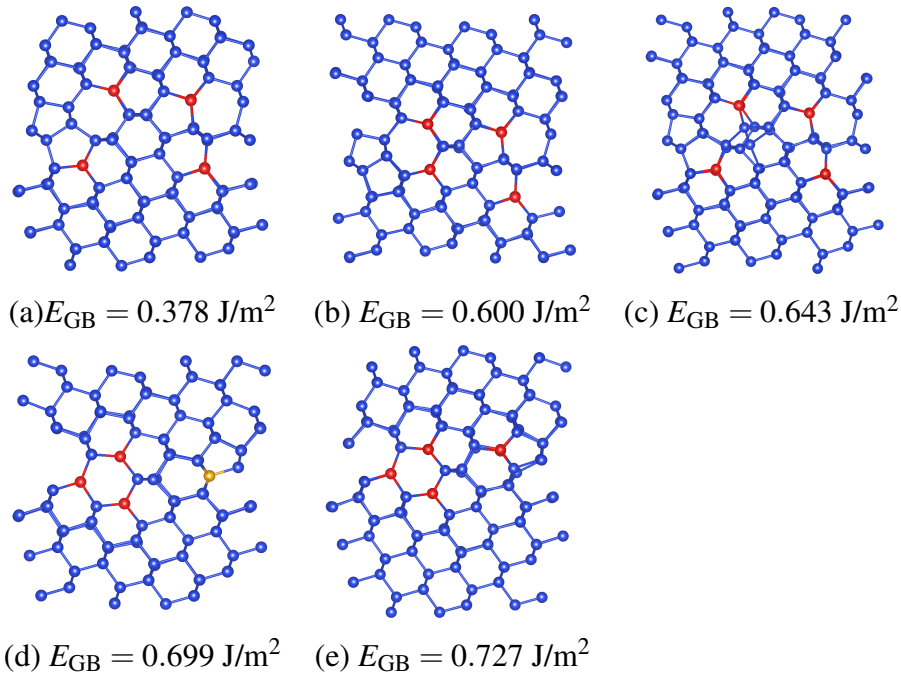


Fig. 4.6 Low-energy structures of the $\Sigma 9(114)$ GB. Four single atomic columns are in (a), (b), (c), and (e); three columns and a pair of five-fold coordinated atoms are in (d). The atoms bonded with single atomic columns and five-fold coordination are indicated by red and orange atoms, respectively.

note that, from high-resolution electron microscopy images [118], it is often not possible to distinguish between single atomic columns and under-coordinated atoms, which may lead to the construction of erroneous empirical models.

The lowest-energy interfaces of the studied GBs with rotation axis $[110]$ are shown with structural patterns in the Tables 4.2 and 4.3.

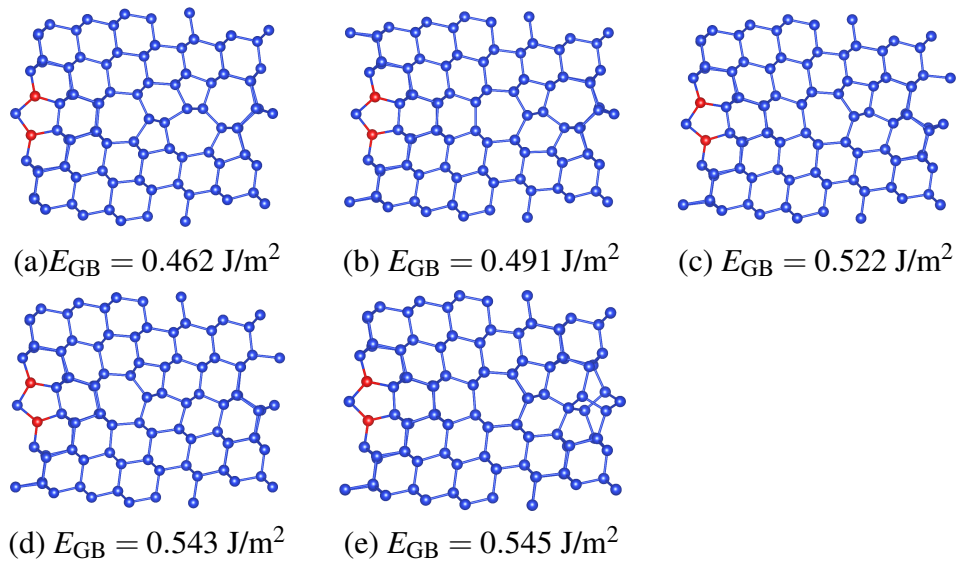


Fig. 4.7 Low-energy structures of the $\Sigma 17b(334)$ GB. Two single atomic columns are in all structures. The atoms bonded with single atomic columns and five-fold coordination are indicated by red and orange atoms, respectively.

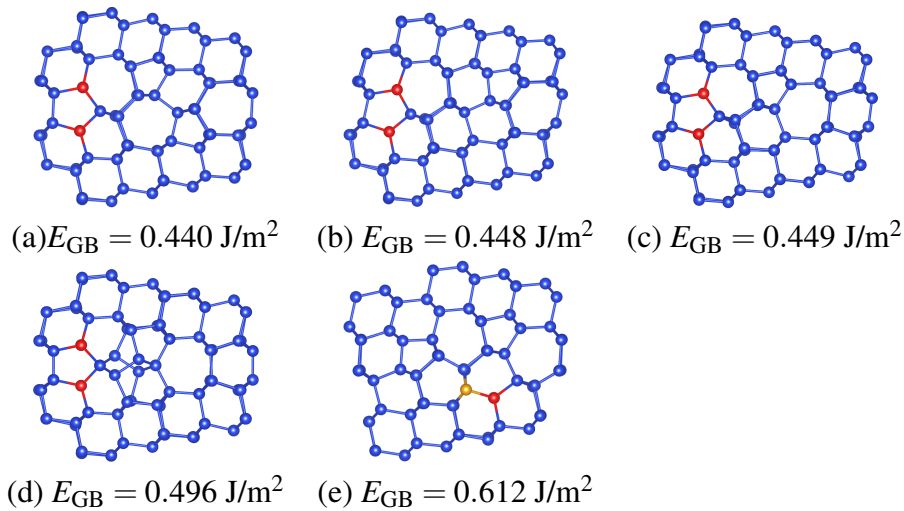


Fig. 4.8 Low-energy structures of the $\Sigma 17b(223)$ GB. Two single atomic columns are in (a) to (d); one column and a pair of five-fold coordinated atoms are in (e). The atoms bonded with single atomic columns and five-fold coordination are indicated by red and orange atoms, respectively.

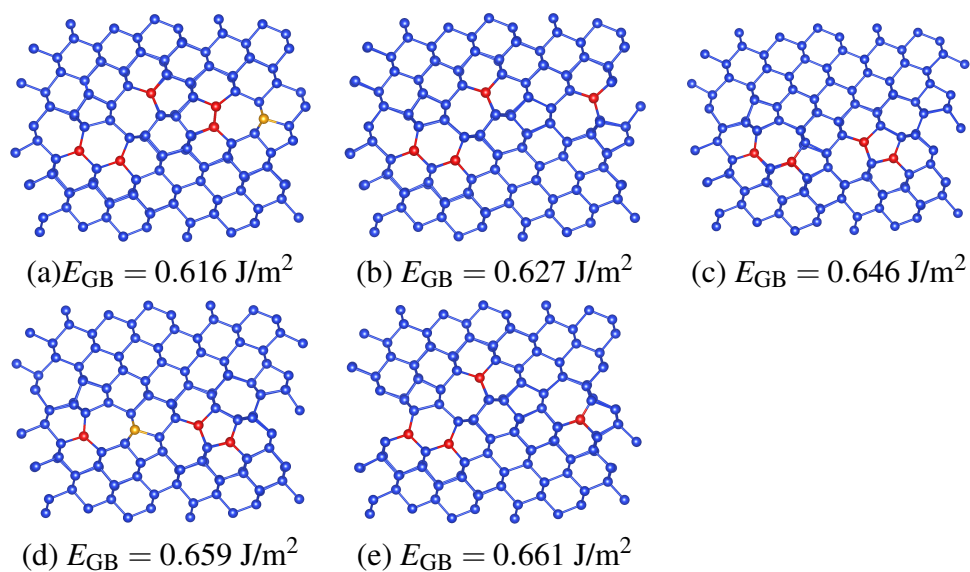


Fig. 4.9 Low-energy structures of the $\Sigma 19a(116)$ GB. Five single atomic columns and a pair of five-fold coordinated atoms are in (a); Four columns are in (b), (c), and (e); three columns and a pair of five-fold coordinated atoms are in (d). The atoms bonded with single atomic columns and five-fold coordination are indicated by red and orange atoms, respectively.

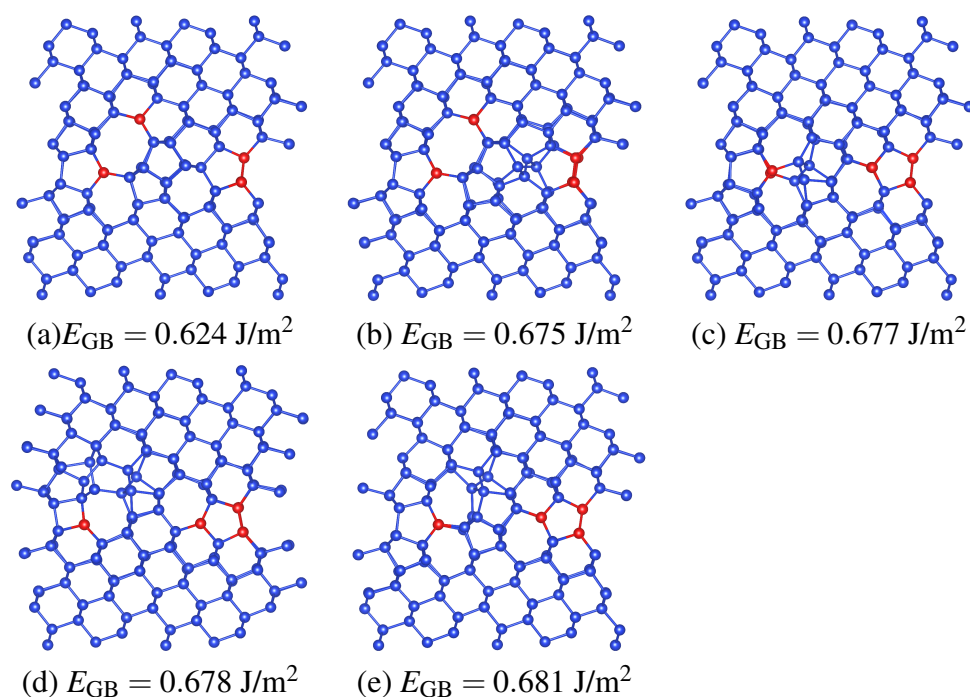


Fig. 4.10 Low-energy structures of the $\Sigma 27a(115)$ GB. Four single atomic columns are in all structures. The atoms bonded with single atomic columns and five-fold coordination are indicated by red and orange atoms, respectively.

Table 4.2 Part I. Summary of misorientation angles θ , GB energies γ and structural patterns for [110] tilt GBs. Atoms forming single atomic columns are indicated in red.

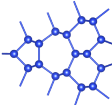
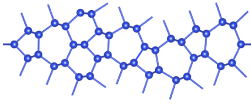
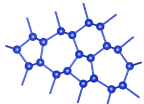
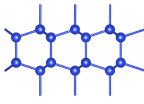
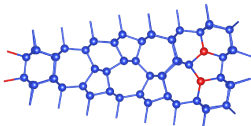
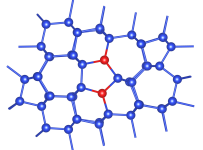
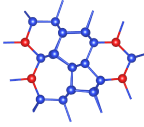
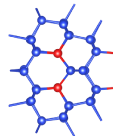
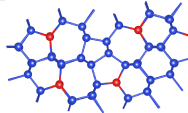
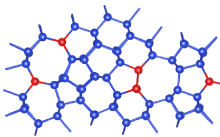
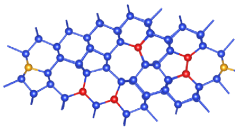
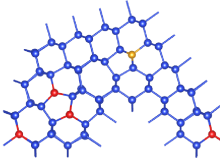
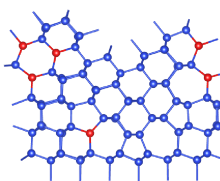
| θ | GB label | γ (J/m ²) | | Patterns |
|----------|-------------------|------------------------------|--|---|
| 26.5° | $\Sigma 19a(331)$ | 0.339 |  | 5 + 6 + 7 |
| 31.6° | $\Sigma 27a(552)$ | 0.381 |  | 5 + 6 + 7 |
| 38.9° | $\Sigma 9(221)$ | 0.202 |  | 5 + 6 + 7 |
| 70.5° | $\Sigma 3(111)$ | 0.013 |  | 6 + 6 _b |
| 86.6° | $\Sigma 17b(334)$ | 0.462 |  | 5 + 5 _{f2} 6 + 6 _b + 6 ₁ + 6 _{b1} 7 + 7 _b + 7 ₁ |
| 93.4° | $\Sigma 17b(223)$ | 0.449 |  | 5 + 5 _{f2} 6 + 6 _b + 6 ₁ + 6 _{b1} 7 + 7 _b + 7 ₁ |
| 109.5° | $\Sigma 3(112)$ | 0.386 |  | 5 6 + 6 _b + 6 _{b1} + 6 _{f2} 7 ₁ |

Table 4.3 Part II. Summary of misorientation angles θ , GB energies γ and structural patterns for [110] tilt GBs. Atoms forming single atomic columns are indicated in red, orange atoms are five-fold coordinated.

| θ | GB label | $E_{GB}(\text{J/m}^2)$ | patterns |
|----------|---------------------|------------------------|---|
| 129.5° | $\Sigma 11(113)$ | 0.402 |  $6 + 6_1 + 6_{b1} + 6_{f2}$ |
| 141.1° | $\Sigma 9(114)$ | 0.378 |  $5 + 5_{f1}$ $6 + 6_b + 6_1 + 6_{b1}$ $7_1 + 7_{b1}$ |
| 148.4° | $\Sigma 27a(115)$ | 0.623 |  $5 + 5^1 + 5_{f1} + 5_{f2}$ $6 + 6_b + 6_1 + 6_{b1}$ $7_1 + 7^3$ $8_2 + 8_{b2}$ |
| 153.5° | $\Sigma 19a(116)$ | 0.616 |  $5 + 5_{f2} + 5^5$ $6 + 6_b + 6_1 + 6_{b1} +$ $6_{f2} + 5^6$ $7_1 + 7_{b1} + 5^7_2$ |
| 70.5° | $\Sigma 3(001x221)$ | 0.497 |  $5_{f2} + 5^5$ $6 + 6_b + 6_1 + 6_{b1} + 5^6_b$ $7_b + 7_{b1}$ |
| 38.9° | $\Sigma 9(111x115)$ | 0.433 |  $5 + 5_{f1}$ $6 + 6_b + 6_1 + 6_{b1} + 6_{f3}$ $7 + 7_1$ |

4.1.2 Grain boundaries with rotation axis [100]

In contrast to the variety of reconstructed patterns shown by the GBs with a [100] tilt axis, we find that all GBs with a [100] tilt axis are characterized by only three structural units: namely atomic spirals formed by three-, four- and five-atom rings oriented along the [100] axis.

As an example, we compare the interfaces of the $\Sigma 5(021)$ GB in Fig. 4.11. The two interfaces in (a) and (c) present similar atomic configurations along the [100] axis and can be hardly distinguished. In contrast, when comparing the structure of the highlighted parts extending along [100] in (b) and (d), a strong reconstruction is showing so that the layer-type interface in the starting structure reconstructs to an atomic spiral along the [100] axis, which dramatically enhances the stability of the interface so that the GB energy drops from 1.883 to 0.393 J/m².

In Table 4.4, more information on investigated structures of GBs with rotation axis [100] is given, and the corresponding structural patterns are listed in the Table 4.5. These results are in agreement with reported experiments [120] and calculations [121, 122, 67]. We also find, for a fixed GB symmetry, that several low-energy reconstructed patterns have similar GB energies. This implies that experimental samples will exhibit a certain degree of disorder, as a mixture of low-energy patterns is expected to coexist at room temperature. Other constraints, related, for example, to the proximity of another GB, may lead to the formation of higher energy reconstructions.

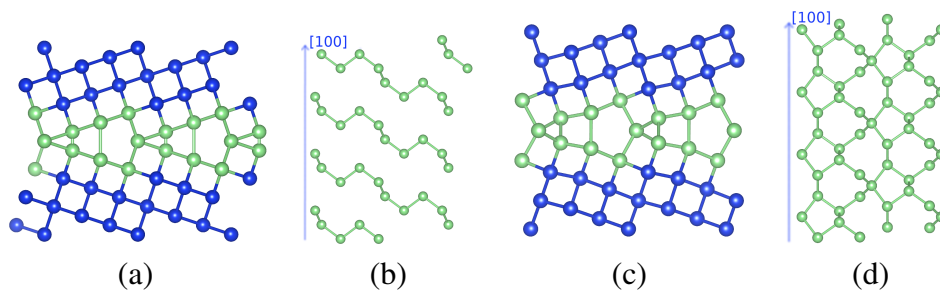
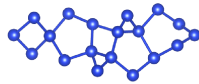
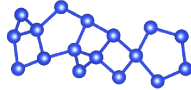
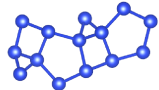
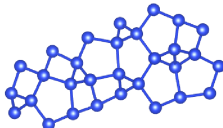
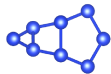
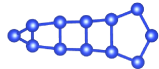
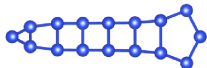


Fig. 4.11 Recurring reconstruction patterns in [100] GBs. (a) and (b): A [100] view of the starting interface of $\Sigma 5(021)$ GB, and the atomic configuration of the interface plane along the [100] axis. (c) and (d): A [100] view of the ground state of the $\Sigma 5(021)$ GB and the atomic spirals along the [100] rotation axis of the reconstructed parts indicated by pale green atoms. The [100] axis is indicated with a light blue arrow line.

Table 4.4 Summary of the structures studied in this work: GB labels, tilt axis, misorientation angle θ , and minimum GB energy γ in J/m^2 after interface reconstruction.

| label | tilt axis | θ | γ | N_{int} | N_{total} |
|--------------------------|-----------|--------------|----------|------------------|--------------------|
| $\Sigma 13\text{a}(051)$ | [100] | 22.6° | 0.672 | 110 | 204 |
| $\Sigma 17\text{a}(041)$ | [100] | 28.1° | 0.601 | 184 | 272 |
| $\Sigma 5(031)$ | [100] | 36.9° | 0.358 | 80 | 160 |
| $\Sigma 29\text{a}(052)$ | [100] | 43.6° | 0.536 | 258 | 464 |
| $\Sigma 5(021)$ | [100] | 53.1° | 0.393 | 46 | 94 |
| $\Sigma 13\text{a}(032)$ | [100] | 67.4° | 0.614 | 98 | 206 |
| $\Sigma 25\text{a}(043)$ | [100] | 73.7° | 0.646 | 294 | 398 |

Table 4.5 Summary of misorientation angles θ , GB energies γ and structural patterns for [100] tilt GBs.

| θ | GB label | $E_{\text{GB}}(\text{J/m}^2)$ | patterns |
|--------------|--------------------------|-------------------------------|---|
| 22.6° | $\Sigma 13\text{a}(051)$ | 0.672 |  |
| 28.1° | $\Sigma 17\text{a}(041)$ | 0.601 |  |
| 36.9° | $\Sigma 5(031)$ | 0.358 |  |
| 43.6° | $\Sigma 29\text{a}(052)$ | 0.536 |  |
| 53.1° | $\Sigma 5(021)$ | 0.393 |  |
| 67.4° | $\Sigma 13\text{a}(032)$ | 0.614 |  |
| 73.7° | $\Sigma 25\text{a}(043)$ | 0.646 |  |

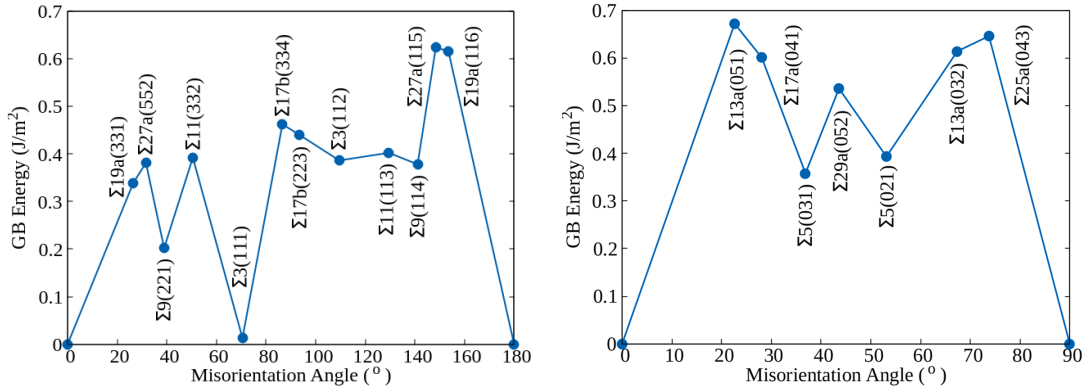


Fig. 4.12 Interface energy γ as a function of the misorientation angle for [110] (left panel) and [100] (right panel) tilt GBs.

4.1.3 Comparison of GB energies

In Fig. 4.12, we plot the GB energies of the ground-state atomic reconstructions, identified by the MHM simulations, of the [110] and the [100] tilt GBs, as a function of the misorientation angle. We can see that the GB energies of the [110] GBs are on average lower than the GB energies of the [100] GBs. Unsurprisingly, the $\Sigma 3(111)$ system has by far the lowest energy [123]. In fact, this is the only system that did not present a significant interface reconstruction during the MHM simulations. The second most stable GB, according to our calculations, is the $\Sigma 9(221)$ interface. This can be understood by noticing that it only includes pairs of five-membered and seven-membered rings, that constitute the 5+7 building blocks also present in low-energy defects of carbon [92]. Interestingly, the combination of 5 and 7-fold atomic rings is also the building block of M-carbon [124] and W-carbon [125]. These patterns appear as well, for example, in low-energy reconstructions of $\Sigma 27a(552)$ and $\Sigma 19a(331)$ GBs (shown in Table 4.2). In contrast, the least stable GBs present more complicated arrangements of ring units, in an attempt to eliminate dangling bonds and to decrease the stretching of the Si–Si bonds. For example, the $\Sigma 27a(115)$ GB, with a GB energy of 0.623 J/m^2 , shows the pattern $5 + 5^1 + 5_{f1} + 5_{f2} + 6 + 6_b + 6_1 + 6_{b1} + 7_1 + 7^3 + 8_2 + 8_{b2}$, while the $\Sigma 19a(116)$ GB, with a GB energy of 0.616 J/m^2 , has $5 + 5_{f2} + {}^5 5 + 6 + 6_b + 6_1 + 6_{b1} + 6_{f2} + {}^5 6 + 7_1 + 7_{b1} + {}^5 7_2$ units (shown in Table 4.2).

For the majority of the GBs studied here, we find that the ground-state structure does not contain five-fold coordinated atoms. There are however exceptions to this rule, namely the $\Sigma 3(001 \times 221)$ and the $\Sigma 19a(116)$ GB. Also for these anomalous cases, we can always find low-lying geometries, just slightly higher in energy, that do not present overcoordination. As we will see in the later part, the presence of five-fold coordinated atoms has important consequences on electronic properties.

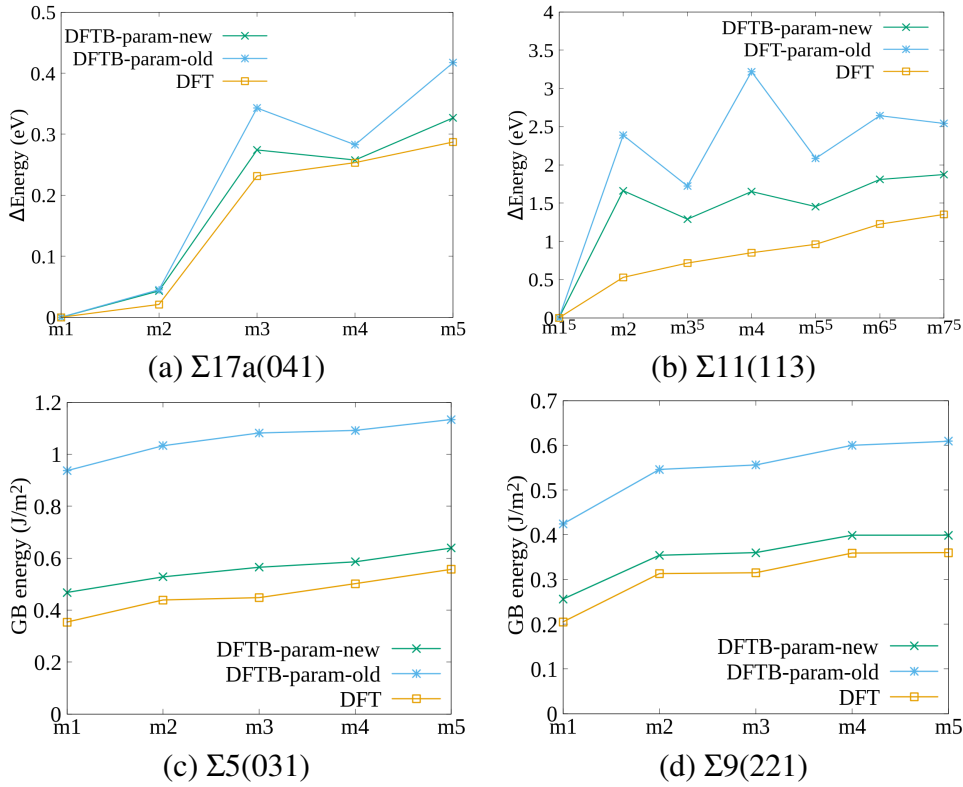


Fig. 4.13 A comparison of energy calculated by DFTB with different parameterizations and DFT. (a) and (b): the difference of total free energy between different structures in $\Sigma 17a(041)$ and (b) $\Sigma 11(113)$ GBs, respectively. (c) and (d): the GB energies of the low-energy structures in $\Sigma 5(031)$ and $\Sigma 9(221)$ GBs. Light blue line: results calculated with DFTB parameterization provided by DFTB+ package; green line: results calculated with our DFTB parameterization; orange line: results obtained with DFT. The structures contain five-fold coordinated defects that are indicated with a superscript “5” on the labels.

4.1.4 Comparison of energy with different DFTB parameterizations

We have introduced the computational details in Chapter 3 that the free energy during structural prediction is calculated by DFTB with tight-binding parameters specially crafted for group-IV elements [55]. Since the most promising structures for reoptimizations are selected by MHM, the accuracy of DFTB parameters in reproducing the energetic properties of GBs is significant to find the ground-state structures. To verify that our parameters are more reliable to calculate the energy than the standard parameters provided by the DFTB+ distributions [82], we compare the energy differences calculated by DFTB with different parameterizations and DFT, as plotted in Fig. 4.13.

We see that, in many cases, there is no significant difference between DFT and the two DFTB calculations (see e.g. Fig. 4.13 (a)), and this is because the tight-binding parameters

available for Si are already rather good, especially when the reconstructions of the interface is such that all Si atoms are four-fold coordinated. Some differences show up when five-fold coordinated atoms are present at the interface. This is visible in Fig. 4.13(b) and it is no surprise that the discrepancy between our parameterization and the standard parameterization appears more pronounced. During the MHM simulation, highly defected structures are explored by the algorithm to reach new minima, and therefore the difference in the reliability of the two parameterizations becomes more severe. Note that the selected structures of the $\Sigma 11(113)$ GB are mainly focusing on the five-fold coordinated defects, thus the comparison of energy starts from structure “m1⁵” which contains five-fold coordinated atoms.

We also find that the DFTB results with our parameterization are a significant improvement for calculating GB energies, as shown by the energies of the $\Sigma 5(031)$ and $\Sigma 9(221)$ GBs that are shown in Fig. 4.13 (c) and (d), respectively. For $\Sigma 5(031)$ GB (Fig. 4.13(c)), the GB energies calculated with our DFTB parameterization are about 0.1 J/m^2 larger than the results of DFT, while the GB energies obtained from standard DFTB parameterization are over two times larger than the results of DFT. And for $\Sigma 9(221)$ GB (Fig. 4.13(d)), our parameterization gives results closer to DFT, so that the difference is between 0.04 to 0.05 J/m^2 . The standard parameterization gives a considerably larger discrepancy. Although the GB energy is always calculated by DFT after we obtain the low-energy structures, the accurate GB energy calculated by DFTB is helpful for estimating the stability of the interfaces, since the supercells are usually large and the DFT calculations are therefore rather costly.

4.1.5 Extension of the study of low-energy GBs to other group-IV elementary crystals

In previous studies, similar models are usually used for describing group-IV GBs, in particular for silicon and germanium GBs, since the atoms in silicon and germanium prefer to bond with each other by σ -bonds. But for carbon, which is well known for its orbital hybridizations, and metallic tin, the ground-state GBs may differ from Si and Ge. Here, we extend the low-energy structures from silicon GBs to other group-IV elementary crystals, including carbon, germanium, and tin. We replace the Si atoms with C, Ge, and Sn atoms, then scale the supercells and atomic positions according to the optimized lattice parameters of diamond C, Ge, and Sn. Finally, the interfaces are reoptimized and the GB energy is calculated with the formula Eq. 3.2. In Table 4.6, the GB energies of the lowest-energy structures for different elements are presented. In Fig. 4.14 the GB energy with respect to different GBs is plotted. The variation of the GB energy of different group-IV elements is displayed. There are similar features for the GBs of all four elements. The GBs with higher energy for silicon

Table 4.6 Summary of the structures studied: GB labels, tilt axis, and GB energy (J/m^2) E_{GB} after reconstructing. The optimized lattice parameters in diamond-like cubic are: $l_{\text{C}} = 3.55$, $l_{\text{Si}} = 5.47$, $l_{\text{Ge}} = 5.76$ and $l_{\text{Sn}} = 6.65$ Å.

| label | C | Si | Ge | Sn |
|-------------------|-------|-------|-------|-------|
| $\Sigma 3(112)$ | 2.851 | 0.386 | 0.320 | 0.171 |
| $\Sigma 5(021)$ | 3.311 | 0.393 | 0.424 | 0.191 |
| $\Sigma 5(031)$ | 3.050 | 0.358 | 0.304 | 0.175 |
| $\Sigma 9(114)$ | 2.615 | 0.378 | 0.328 | 0.175 |
| $\Sigma 11(113)$ | 2.646 | 0.402 | 0.337 | 0.181 |
| $\Sigma 11(332)$ | 2.796 | 0.392 | 0.332 | 0.228 |
| $\Sigma 13a(051)$ | 4.809 | 0.672 | 0.537 | 0.294 |
| $\Sigma 17b(223)$ | 3.011 | 0.449 | 0.348 | 0.198 |
| $\Sigma 17b(334)$ | 3.115 | 0.462 | 0.371 | 0.217 |
| $\Sigma 19a(331)$ | 2.265 | 0.339 | 0.318 | 0.168 |
| $\Sigma 19a(116)$ | 4.172 | 0.616 | 0.464 | 0.286 |
| $\Sigma 27a(115)$ | 4.403 | 0.624 | 0.518 | 0.269 |
| $\Sigma 29a(052)$ | 4.077 | 0.536 | 0.417 | 0.235 |

are also more unstable in carbon, germanium, and tin. For example, the $\Sigma 13(051)$ GB shows the highest energy for all four elements. Also, $\Sigma 19(116)$ and $\Sigma 27a(115)$ GBs have higher energies than an average GB in each of the curves. We also find that the average GB energy of carbon GBs is one magnitude higher than the average energy of GBs of the other three elements. The GBs energy of carbon is higher than 3 J/m^2 in average while the GB energy of the other elements is less than 0.7 J/m^2 (0.672 J/m^2 of $\Sigma 13a(051)$ Si GB). In particular, the Sn GBs have an average GB energy of only 0.2 J/m^2 which is much lower than for the other elements. In addition to the differences in the GB energies for the different elements, the energy curves become flatter when going from carbon to tin. This reflects a smaller energy discrepancy among the GBs for tin than for the three other elements in the plot.

We now move from the general lowest-energy GBs to specific GBs. Here, we compare the energy of five low-energy interfaces for each GB with a special focus on the interfaces containing five-fold coordinated atoms. We compare the energy of the five low-energy interfaces for each GB, especially the interfaces containing defect bonds, namely five-fold coordinated atoms. In Fig. 4.15, we compare the GB energy of interfaces in $\Sigma 3(112)$ and $\Sigma 9(114)$ GBs. The energy ranking of the interfaces is usually consistent across all group-IV elements if the interface structures contain only four-fold coordinated atoms. This is different for interfaces with five-fold coordinated atoms. For these interfaces, the GB energy of the C GBs increases significantly compared to the GBs of the other three elements. As shown in

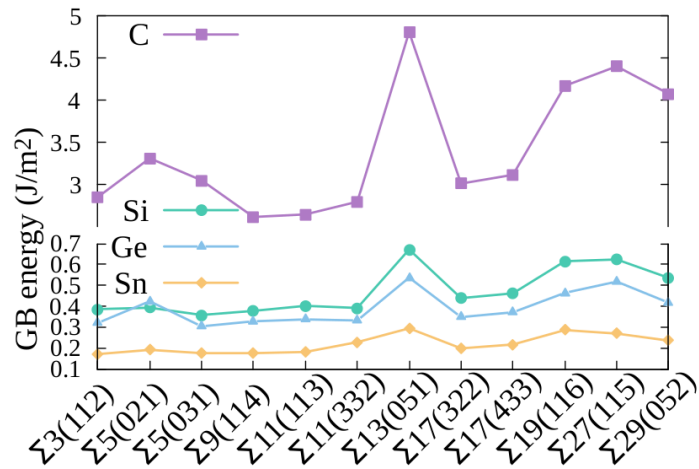


Fig. 4.14 GB energy of the ground-state GBs consisting of carbon (purple squares), silicon (green dots), germanium (light blue triangles), and tin (orange rhombuses) atoms, respectively.

Fig. 4.15(a), the interface with the fourth lowest GB energy for Si becomes the highest-energy interface for C. More precisely, the $m4^5$ interface of $\Sigma3(112)$ GB is about 1.38 J/m^2 higher in GB energy than $m5$. A similar result is found for $\Sigma9(114)$ GB, where the GB energy curve shows a sharp peak at $m3^5$ with a GB energy of 6.24 J/m^2 .

In contrast to the situation in C GBs, five-fold coordinations in Ge and Sn GBs are less unstable. As shown in Fig. 4.15(a), the GB energy of the $m4^5$ interface in both Ge and Sn is lower than the one of the $m3$ interface. This was different in Si where the $m3$ interface had lower energy than the $m4^5$ interface. In Fig. 4.15(b), the GB energies of the most stable interfaces for the $\Sigma27a(115)$ GB are shown. Here, the stability of five-fold coordination is more even more visible. The $m3^5$ interface is now the lowest-energy structure in the Ge and Sn GBs. In the Si GB, it is the one with the third lowest energy.

These differences between the coordinations of C and Ge/Sn are in agreement with previous studies. These studies reported hyper-coordinated atoms for Ge and Sn [126–129] but hardly any over-coordinated atoms in carbon allotropes. These over-coordinated atoms of carbon usually appear under high pressure [130].

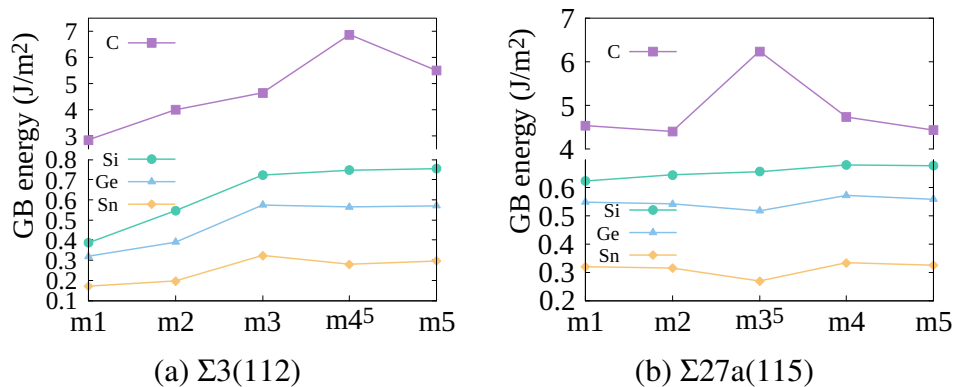


Fig. 4.15 GB energy of the five lowest-energy interfaces in (a) $\Sigma 3(112)$ and (b) $\Sigma 27a(115)$ GBs. C, Si, Ge, and Sn GBs are represented by purple squares, green dots, light blue triangles, and orange rhombuses, respectively. The low-energy structures are labeled with m1 to m5, and the structures containing five-fold coordinated atoms are indicated by a superscript “5”.

4.2 Are the interfaces more stable after removal of atoms?

During our simulations, we observe that in many cases the lowest-energy reconstruction is attained only after adding (or removing) atoms to (from) the interface region. We tested systematically all possible modifications of the atomic structure, until reaching a configuration equivalent to the starting one, differing by the simple addition of a full atomic plane. The influences on structural reconstructions by removal of atoms from the interface in tilt copper GBs have also been stressed in previous studies [131, 72, 74] in which the interface reaches new structural phases with lower energy for certain GBs.

We notice that in those studied copper GBs when a plane of copper atoms is removed from the interface, the reconstructed GB will recover the structure obtained from the initial interface. But in silicon tilt GBs, we found that the GBs can be classified into two types: for type-I GBs, when one plane of atoms is removed, the interface recovers the structure from the initial interface, while for type-II GBs, the interfaces reach new configurations and the recoveries only occur with two planes of atoms being removed. To characterize the removal of atoms, we use a dimensionless parameter $\lambda = \frac{N_{\text{rm}}}{N_{\text{plane}}}$, where N_{rm} is the number of removed atom at the interface region, and N_{plane} is the number of atoms in a perfect boundary plane.

As an example, we present the lowest-energy structures found in the $\Sigma 5(021)$ GB after the different number of atoms were removed from the starting interface in Fig. 4.16. Note that, the atomic positions of removed atoms at the interface region are random that this will not affect the results of the reconstructions. As we can see, the ground-state structure is obtained after two atoms are removed ($\lambda = 1$). The reconstructed structure in panel (f) ($\lambda = 2$) is equal to the structure in panel (a) ($\lambda = 0$), which consists of the spiral patterns presented in Fig. 4.11. When one atom is removed, the interface (panel (b)) contains over-coordinated and dangling-bonded atoms, which lead to a high GB energy of it. Compared with the ground-state structure (Fig. 4.16 (c)), the unsaturated atom can be regarded as an extra interstitial atom which leads to an over-bonding of the neighbor atoms. We find that, for GBs with the rotation axis [100], the dangling bonds are only found at the interfaces when the odd number of atoms are removed. And when pairs of atoms are removed, the under- or over-coordinated atoms hardly appear. The reconstructed structure in panel (d), where three atoms are removed, the GB energy of is also higher than the structures in panel (a), (c), and (e). This is because parts of bonds are stretched.

For a better comparison, we plot the GB energy as a function of λ in Fig. 4.17 for all studied GBs. The plots are separated into four parts. In the panels (a) and (c) are the results of type-I GBs with rotation axis [100] and [110], respectively, where the range of λ is from 0 to 1 since the interfaces at $\lambda = 1$ recover the structures of $\lambda = 0$. While in panels (b) and (d), the results of type-II [100] and [110] GBs are plotted with a range of λ from 0 to 2.

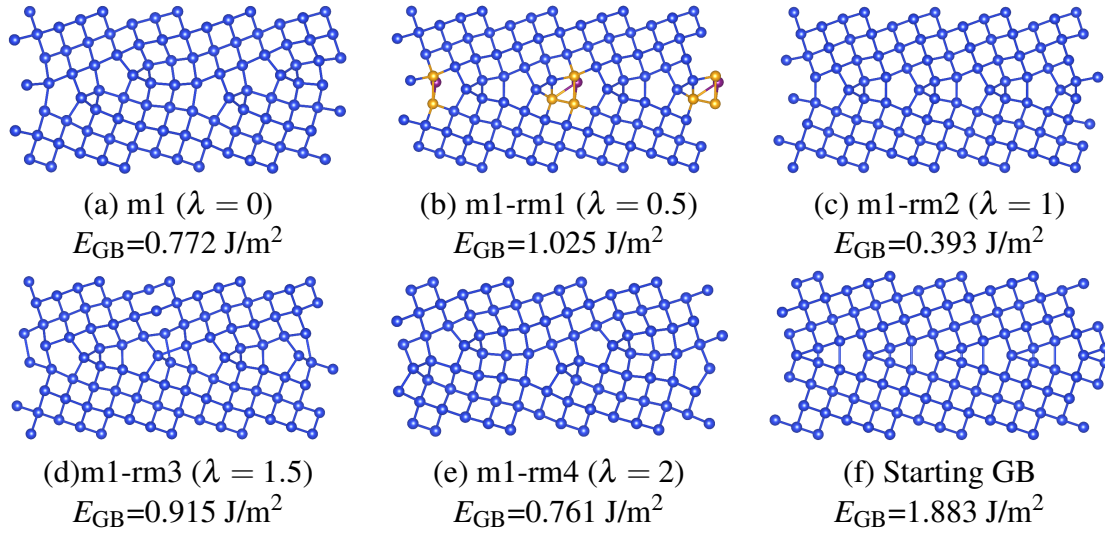


Fig. 4.16 The lowest-energy structures found in $\Sigma 5(021)$ GB, from panel (a) to (e), different number of atoms are removed from the initial interface region, and panel (f) shows the starting interface. Here we use the label “rm” to indicate the removal of atoms and this is followed by a number to indicate how many atoms are removed. For a clear representation, each panel shows two unit cells along the boundary. In the unit cell, there are two atoms per (021) plane, $N_{\text{plane}}=2$. The blue atoms represent the full bonded Si atoms, orange atoms represent over-coordinated atoms and violet atoms represent the atoms with dangling bonds.

In general, we find that removing atoms from the interfaces leads to structures with higher energies after reconstruction of the interfaces, especially for type-I GBs (with $0 < \lambda < 1$). For example, in Fig. 4.17 (a) and (c), the ground-state interfaces of type-I GBs are only obtained from the starting structures or when a whole plane of atoms is removed ($\lambda = 1$).

But for type-II GBs (Fig. 4.17(b) and (d)), adjusting the number of atoms at the interfaces is more essential for reconstructing the lower-energy structures. For example in $\Sigma 5(021)$ $\Sigma 13a(032)$, $\Sigma 25a(043)$ and $\Sigma 17b(223)$ GBs, the reconstructed interfaces of the starting structures are much higher in energy. And the ground-state interfaces can only be obtained when a whole plane of atoms is removed. Detailed information on the GB energies due to the removal of atoms can be found in Table 4.7 and 4.8.

By drawing the boundary planes in a perfect silicon supercell, and associated with the information presented in Table 4.7 and 4.8, we find the classification of type-I and -II GBs is not random, so that it is predictable before the structural reconstruction. To investigate the mechanism, we start from the basic geometry of bulk silicon. As we know, the diamond cubic structure consists of two of the same face-centered cubic with a displacement of $(0.25, 0.25, 0.25) \cdot l_0$, where l_0 is the lattice constant of the cubic structures. For instance, a bulk silicon cell is shown in Fig. 4.18(c), where the atoms in the two face-centered cubic structures are

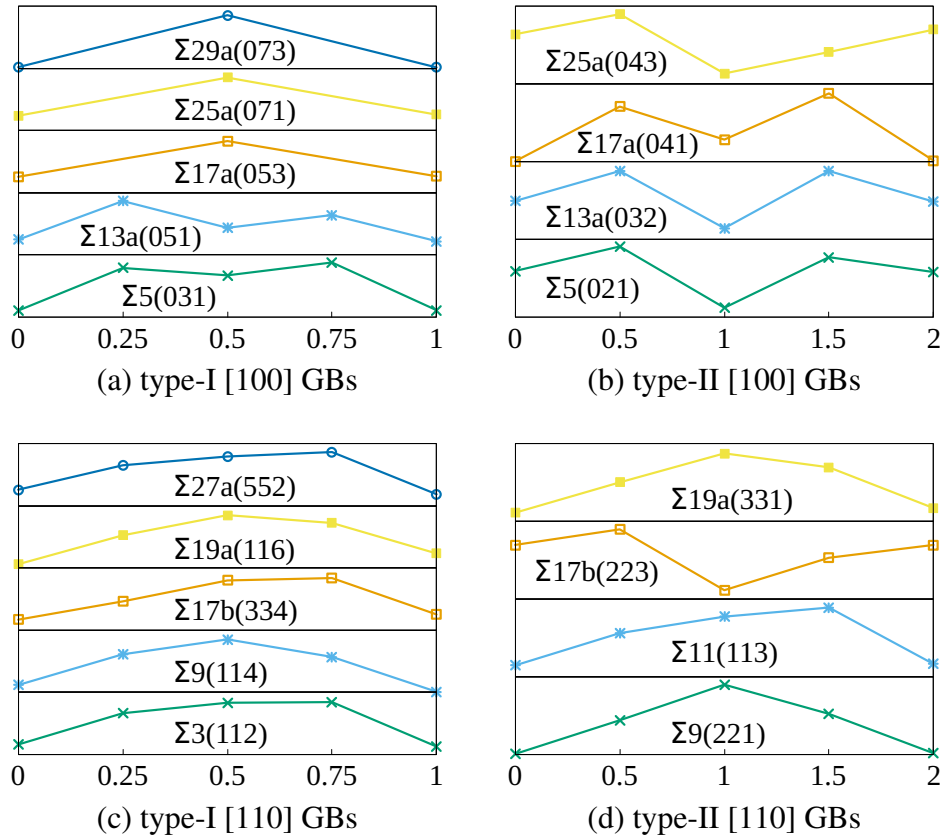


Fig. 4.17 The GB energy varies with respect to the atomic fraction of the boundary plane λ . Panels (a) and (b) show the results of GBs with rotation axis [100], panels (c) and (d) show the results of GBs with rotation axis [110]. The presented results start from the atomic structures obtained by the initial structures until the equivalent structures, in panels (a) and (c) $0 \leq \lambda \leq 1$, in panels (b) and (d) $0 \leq \lambda \leq 2$.

Table 4.7 The GB energy E_{GB} of type-I GBs with respect to the atomic fraction in the boundary plane. N_{plane} is the number of atoms in the perfect boundary plane. The equivalent atomic configurations of a GB are indicated by the underline. For the GBs with $N_{plane}=2$, there are not any data when $\lambda=0.25$ and 0.75 . This is indicated by the symbol "–".

| λ | | 0 | 0.25 | 0.5 | 0.75 | 1 |
|-------------------|-------------|------------------------------|-------|-------|-------|--------------|
| Lable | N_{plane} | E_{GB} (J/m ²) | | | | |
| $\Sigma 5(031)$ | 4 | <u>0.358</u> | 0.756 | 0.687 | 0.807 | <u>0.361</u> |
| $\Sigma 13a(051)$ | 4 | <u>0.680</u> | 0.885 | 0.743 | 0.811 | <u>0.672</u> |
| $\Sigma 17a(053)$ | 2 | <u>0.597</u> | - | 0.816 | - | <u>0.600</u> |
| $\Sigma 25a(071)$ | 2 | <u>0.657</u> | - | 0.934 | - | <u>0.665</u> |
| $\Sigma 29a(073)$ | 2 | <u>0.510</u> | - | 0.912 | - | <u>0.508</u> |
| $\Sigma 3(112)$ | 4 | <u>0.409</u> | 0.762 | 0.880 | 0.888 | <u>0.386</u> |
| $\Sigma 9(114)$ | 4 | <u>0.378</u> | 0.715 | 0.878 | 0.686 | <u>0.304</u> |
| $\Sigma 11(332)$ | 4 | <u>0.392</u> | 0.736 | 0.702 | 0.651 | 0.477 |
| $\Sigma 17b(334)$ | 4 | <u>0.462</u> | 0.571 | 0.696 | 0.710 | 0.493 |
| $\Sigma 19a(116)$ | 4 | <u>0.616</u> | 0.742 | 0.850 | 0.796 | <u>0.663</u> |
| $\Sigma 27a(552)$ | 4 | <u>0.381</u> | 0.503 | 0.547 | 0.569 | 0.358 |

Table 4.8 The GB energy E_{GB} of type-II GBs with respect to the atomic fraction in the boundary plane. N_{plane} is the number of atoms in the perfect boundary plane. The equivalent atomic configurations of a GB are indicated by an underline. The GB energies of structures of $\Sigma 13a(032)$ with $\lambda=0.5$ and 1.5 are rather close, but the atomic structures are actually different.

| λ | | 0 | 0.5 | 1 | 1.5 | 2 |
|-------------------|-------------|------------------------------|-------|-------|-------|--------------|
| Lable | N_{plane} | E_{GB} (J/m ²) | | | | |
| $\Sigma 5(021)$ | 2 | <u>0.772</u> | 1.025 | 0.393 | 0.915 | <u>0.761</u> |
| $\Sigma 13a(032)$ | 2 | <u>0.698</u> | 0.790 | 0.614 | 0.791 | <u>0.696</u> |
| $\Sigma 17a(041)$ | 2 | <u>0.601</u> | 0.770 | 0.668 | 0.811 | <u>0.603</u> |
| $\Sigma 25a(043)$ | 2 | <u>0.818</u> | 0.906 | 0.646 | 0.740 | <u>0.838</u> |
| $\Sigma 9(221)$ | 6 | <u>0.202</u> | 0.524 | 0.864 | 0.585 | <u>0.209</u> |
| $\Sigma 11(113)$ | 8 | <u>0.391</u> | 0.653 | 0.787 | 0.861 | <u>0.402</u> |
| $\Sigma 17b(223)$ | 2 | <u>0.697</u> | 0.785 | 0.440 | 0.624 | <u>0.697</u> |
| $\Sigma 19a(331)$ | 4 | <u>0.339</u> | 0.476 | 0.607 | 0.544 | <u>0.360</u> |

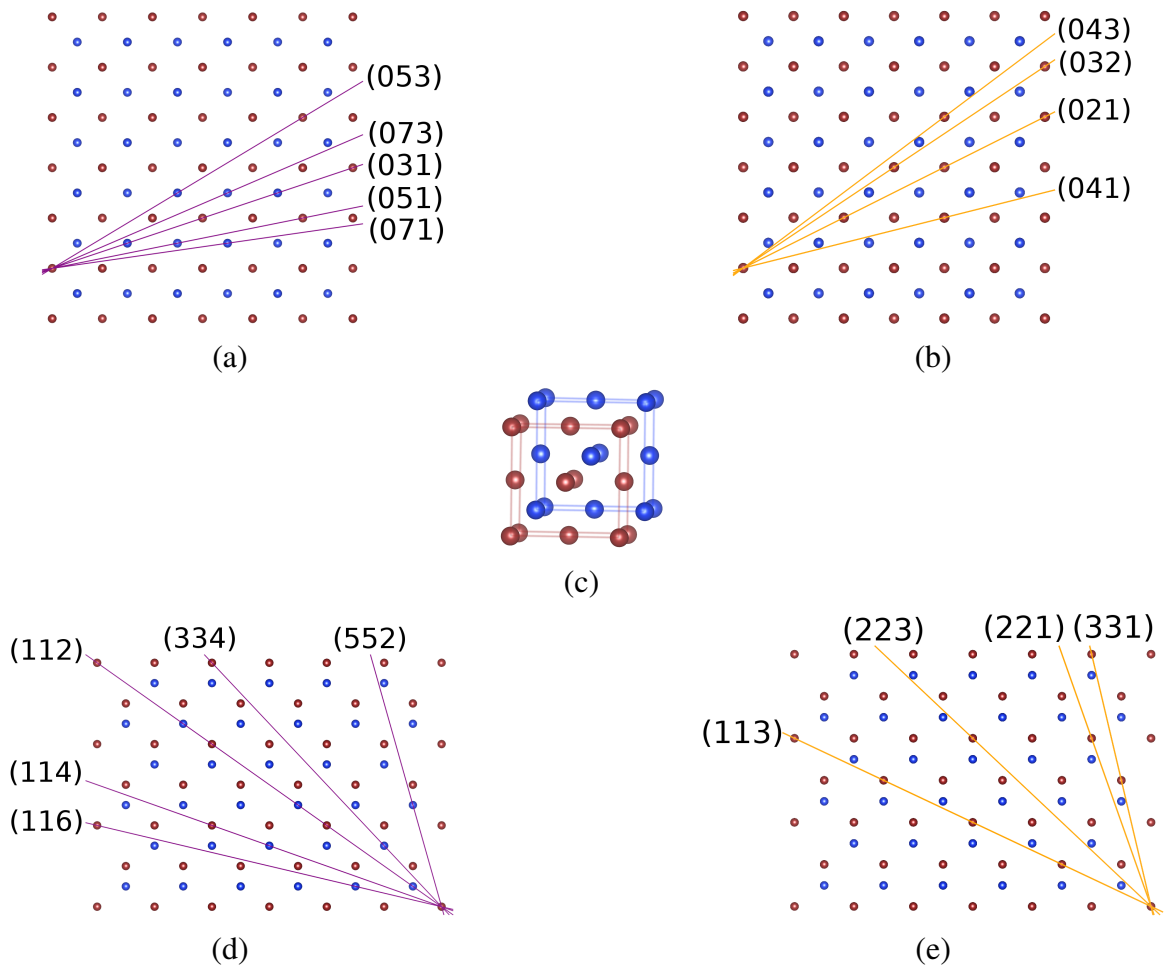


Fig. 4.18 The interface planes are drawn in a $3 \times 3 \times 3$ silicon unit cell. Panels (a) and (d) show the planes of type-I GBs with purple lines, while the planes of type-II GBs are shown by orange lines in (b) and (e). In panel (c), a unit cell of bulk silicon is presented, and two face-centered cubics are represented by brown and blue atoms, respectively.

indicated by brown and blue atoms, respectively. In panels (a)(d) and (b)(e) of Fig. 4.18, the boundary planes of type-I and -II GBs are drawn in a $3 \times 3 \times 3$ silicon supercell, respectively. We find that all the boundary planes of type-I GBs follow the directions that cross both brown and blue atoms, while the boundary planes of type-II GBs only cross brown (or blue) atoms. This shows us that we can identify the silicon planes, which contribute to both face-centered cubic substructures, as type-I GBs.

To construct the interface planes of type-I GBs, we use a simple geometric way. In Fig. 4.19, we put two schemes for type-I boundary planes of GBs with the rotation axis $[100]$ and $[110]$, respectively. The direction of those boundary planes are determined by angles α_{100} and β_{110} , respectively. The tangent of those angles can be expressed as

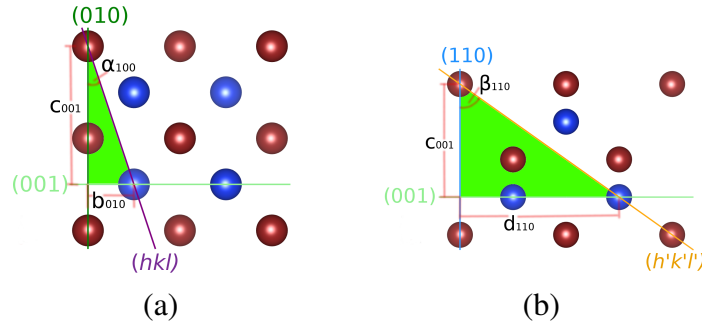


Fig. 4.19 Schematic of interface planes for type-I GBs in a cubic silicon unit cell, (a) and (b) show the planes of GBs with [100] and [110] rotation axis, respectively. The Si atoms in different FCC are brown and blue atoms, the (100), (010), and (110) planes are indicated by light green, deep green, and light blue lines. The interface plane are represented by purple and orange lines with Miller indices (hkl) and $(h'k'l')$.

$\tan \alpha_{100} = \frac{b_{010}}{c_{001}} = \frac{|l|}{|k|}$ and $\tan \beta_{100} = \frac{d_{110}}{c_{001}} = \frac{\sqrt{2}}{2} \cdot \frac{|l'|}{|k'|}$, where b_{010} and c_{001} are the possible distances between the layers that are composed of blue or maroon atoms along [010] and [001] directions, respectively. The calculated values of them are:

$$b_{010} = 0.25 * l_0 + 0.5 * n * l_0, \quad (4.1)$$

$$c_{001} = 0.25 * l_0 + 0.5 * m * l_0. \quad (4.2)$$

Where m, n are 0, 1, 2, 3... . d_{110} is the distance between the two non-equivalent layers along [110] direction, so that $d_{110} = \frac{\sqrt{2}}{4} * l_0 + \frac{\sqrt{2}}{2} q * l_0$ with $q = 0, 1, 2, 3, \dots$. After we substitute the possible value of b_{010} , c_{001} , b_{110} , we obtain:

$$\frac{|l|}{|k|} = \frac{2n + 1}{2m + 1} \quad (4.3)$$

$$\frac{|l'|}{|k'|} = \frac{2q + 2}{2m + 1} \quad (4.4)$$

Since in [100] GBs, the Miller index h is always 0 and in [110] GBs $h' = k'$, the Miller indices of the boundary planes in type-I GBs can be written as $(0, 2m + 1, 2n + 1)$ and $(2m + 1, 2m + 1, 2q + 2)$ for [100] and [110] GBs, respectively. Using the relation between coincidence lattice density and Miller indices of the boundary plane in Eq. 2.42, we can calculate Σ , then easily distinguish the types of studied GBs. For example, when $m = 1$ and $n = 0$, we obtain the GB $\Sigma 5(031)$, where $\Sigma = \frac{1}{2} * (3^2 + 1^2) = 5$. When $m = 0$ and $q = 0$, we have the GB $\Sigma 3(112)$, where $\Sigma = \frac{1}{2} * (1^2 + 1^2 + 2^2) = 3$. According to the results of the interface reconstructions shown in Fig. 4.17, these two GBs are indeed belong to type-I GBs.

In contrast, for the GBs with boundary planes that the Miller indices do not satisfy Eqs. 4.3 and 4.4, they belong to type-II GBs.

There is also another more visualized way to roughly distinguish the type of a GB before reconstructions, we can compare the interfaces after a whole plane of atoms is removed with the initial interfaces. For example, in Fig. 4.20 and 4.21 we present the interfaces of $\Sigma 5(031)$ and $\Sigma 5(021)$ GBs. We removed the whole plane of atoms at the interface (highlighted by red dots), then we shift the top grains along a vector between the two neighbor atoms in different planes, in Fig. 4.20 is Si_1Si_5 and in Fig. 4.21 is Si_1Si_3 . Strictly speaking, the shift of top grains can also follow other paths to fill the vacancies, such as from Si_6 to Si_1 and Si_7 to Si_1 in $\Sigma 5(031)$ interface (Fig. 4.20), and from Si_4 to Si_1 in $\Sigma 5(021)$ interface (Fig. 4.21), but the results are equivalent so we only present the simplest cases.

By comparing the interfaces in Fig. 4.20 (b) and (d), it shows clearly that the two interfaces in $\Sigma 5(031)$ GB are in same configurations. But for $\Sigma 5(021)$ GB, the result is different that the interface is unable to recover the structure of the starting GB by simply shifting the grain after the removal of atoms. In Fig. 4.21 (a), all the atoms are full-bonded, while in Fig. 4.21 (c), atoms at sites of Si_5 and Si_6 are only bonded with other three atoms. During the structural reconstruction, this inequivalent interface in $\Sigma 5(021)$ GB reconstruct to different structures, while in $\Sigma 5(031)$ GB the reconstructions are the same. The results are consistent with our classification that $\Sigma 5(031)$ and $\Sigma 5(021)$ belong to type-I and -II GBs, respectively.

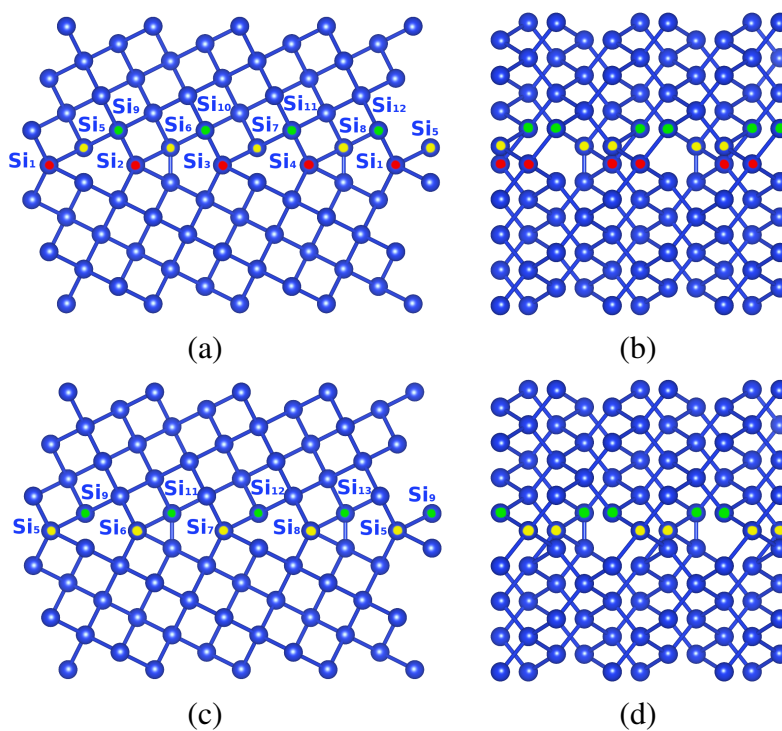


Fig. 4.20 An example of a type-I [100] GB in which atoms are removed from the interface. The panel shows the starting interface of the $\Sigma 5(031)$ GB viewed along [100] direction, the atoms of interface plane are highlighted by red dots, and with labels Si₁ to Si₄. The atoms in the planes above the interface plane are indicated by yellow and green dots and with labels from Si₅ to Si₁₂. The interface in the view of [010] direction is shown in panel (b). In panel (c), the atoms Si₁ to Si₄ are removed, and the top grain is shifted by a vector $\vec{Si_1Si_5}$. The interface viewed along [010] direction is shown in (d).

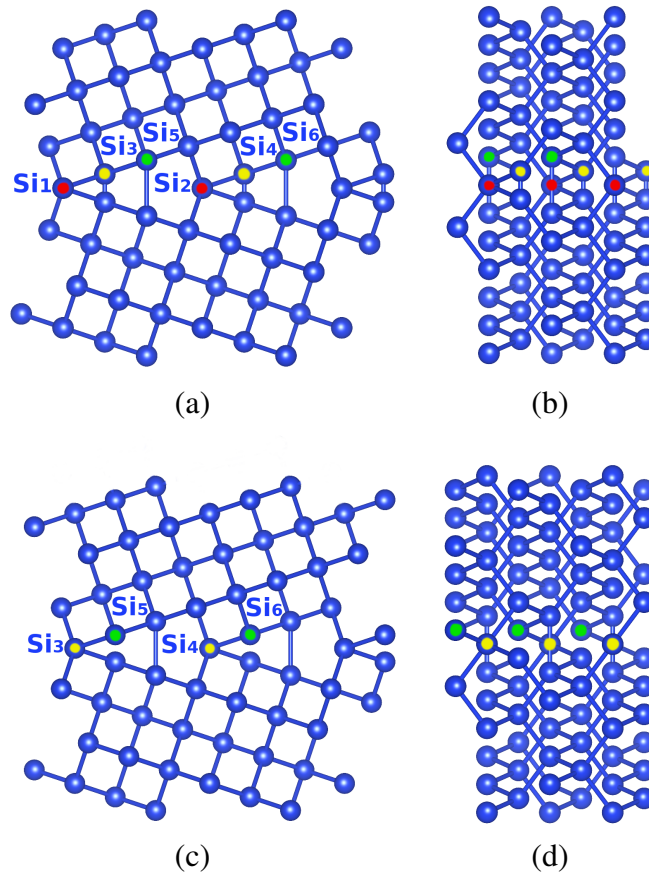


Fig. 4.21 An example of a type-II [100] GB in which atoms are removed from the interface. The panel shows the starting interface of the $\Sigma 5(021)$ GB viewed along [100] direction, the atoms of interface plane are highlighted by red dots, and with labels Si₁, Si₂. The atoms in the planes above the interface plane are indicated by yellow and green dots and with labels from Si₃ to Si₆, and the interface in the view of [010] direction is shown in panel (b). In panel (c), the atoms Si₁ and Si₂ are removed, and the top grain is shifted by a vector Si₁Si₃, the interface viewed along [010] direction is shown in (d).

4.3 Electronic properties of reconstructed interfaces

We now turn to the discussion of the electronic properties of the GBs and how the structure at the interface can affect the transport of charge carriers. We calculated the total density of states (DOS) and partial DOS, where we separate contributions from atoms belonging to bulk and interface layers, for all lowest-energy reconstructed supercells. As an example, we show, in Fig. 4.22, the partial DOS in an energy interval around the band gap for two polymorphs of the $\Sigma 3(112)$ GB: the asymmetric and mirror-symmetric models of Ziebarth (see panels (a) and (d) of Fig. 4.4). These structures correspond to our ground state and the structure with the fourth lowest energy, with GB energies of 0.386 and 0.747 J/m², respectively. Both interface reconstructions have been observed in experiments [113] and contain single atomic columns. In the symmetric one, we can also find five-fold coordinated atoms, that are not present in the asymmetric interface.

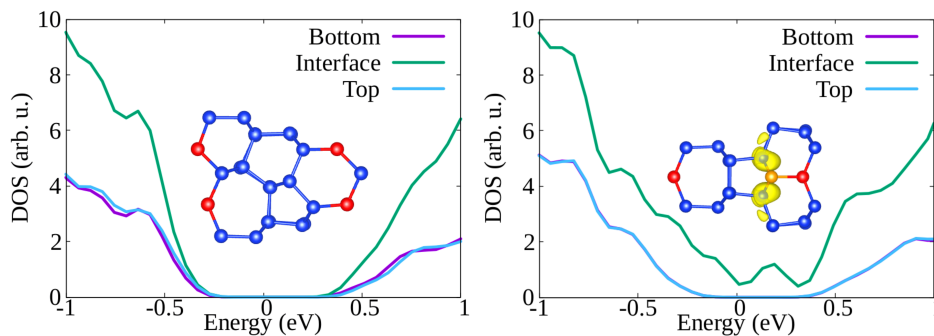


Fig. 4.22 Contributions to the DOS of the $\Sigma 3(112)$ GB coming from atoms in the top and bottom bulk layers, and atoms in the interface region. The left panel shows the DOS calculated for the non-symmetric model of Ziebarth (lowest-energy structure in Si) and in the right panel for the corresponding mirror-symmetric model (structure with the fourth lowest energy), respectively. In the inset, we can see [110] projections of the reconstruction patterns. In the right panel, we can also see the partial charge density corresponding to the DOS energy interval from -0.1 to 0.2 eV. The Fermi energy is set to zero.

Looking at the left panel of Fig. 4.22, we can observe that the contributions to the DOS coming from bulk-like atoms or interface atoms are rather similar and similar to those of tetrahedrally coordinated atoms in monocrystalline silicon. In particular, there are no deep defect states in the gap. In contrast, the DOS of the symmetric structure containing five-fold coordinated atoms (right panel of Fig. 4.22) displays a broad peak in the middle of the band-gap. In the inset, in which we plot the charge density coming from the electronic states around the Fermi level, we can clearly see that the electronic density corresponding to the states in the gap is localized on the five-fold coordinated atoms. We remind the reader that

localized trapping states can act as electron-hole recombination centers, and therefore are responsible for the reduction of the electrical performance of, e.g., a solar device.

Calculated DOS of lowest-energy GBs can be found in Fig. 4.23 and 4.24. These calculations prove consistently that single atomic columns, often present at the interface of [110] GBs, and spiral rings, typical of reconstructions of [100] GBs, do not yield states in the gap, and are therefore benign for electron and hole transport in solar devices. In contrast, we found a perfect correlation between the existence of localized defect states in the gap and the presence of five-fold coordinated atoms.

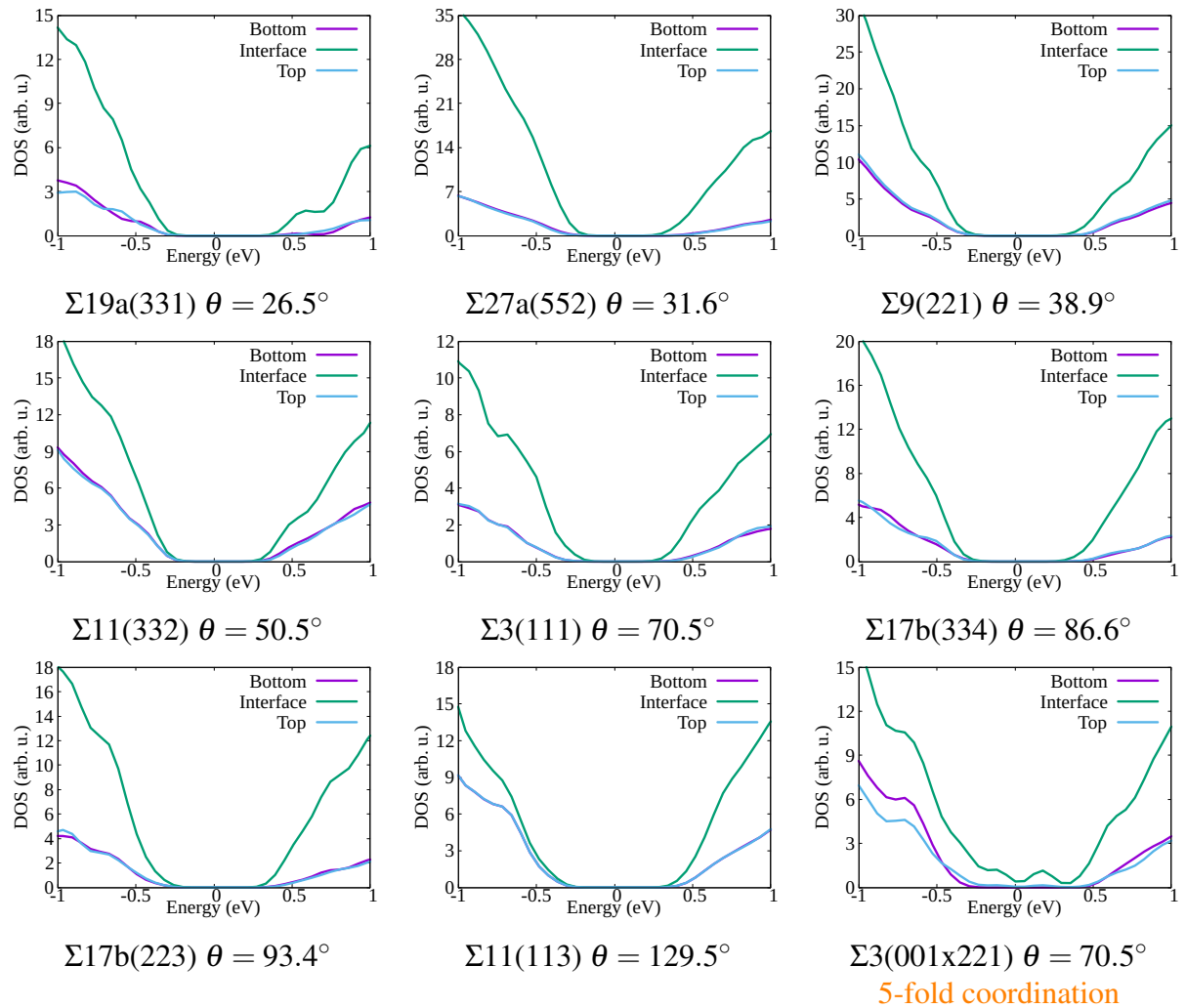


Fig. 4.23 Part I. Densities of states close to the band gap. The Fermi energy is set to zero.

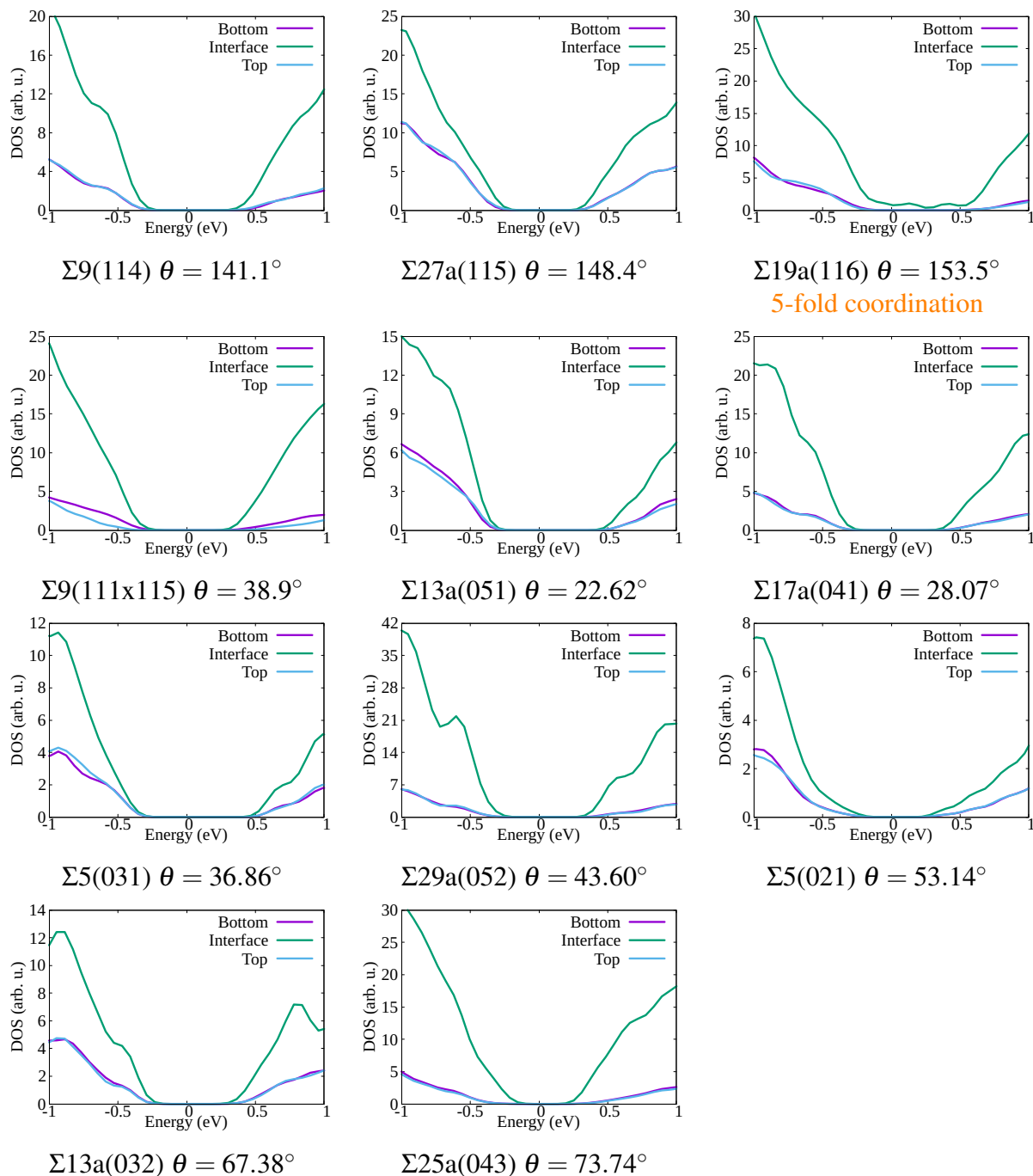


Fig. 4.24 Part II. Densities of states close to the band gap. The Fermi energy is set to zero.

Chapter 5

Simulation of diamond/graphite interface in crystalline carbon

Diamond-graphite structures have recently drawn wide attention because of their special compositions of sp^2 and sp^3 -hybridized carbon atoms and potential applications in electronic devices. However, only a few of them at certain interfaces of diamond have been studied and very little knowledge about the constructed patterns exists. In this chapter, we study the formation of diamond-graphite structures in various diamond interfaces with our constrained structure prediction approach, which has been introduced in Chapter 3. First, in Sec. 5.2.1, we present the transition between diamond and graphite at (001) diamond interface. Then, in Sec. 5.2.2 and 5.2.3, we extend the study of graphitizations in diamond to different interfaces which are parallel to the [110] and [100] axis, respectively. Finally, we calculate the DOS of the obtained diamond-graphite structures to determine these new carbon allotropes are semiconductors or they have metallic characteristics.

5.1 Diamond-graphite: a new carbon allotrope

Carbon is well known for its ability to form diverse types of bonds, leading to a diverse family of carbon allotropes. The most-well known allotropes composed of sp^3 or sp^2 -hybridized atoms are diamond and graphite, respectively. Those two materials are extremely different from the structural and electronic points of view: diamond is the hardest material existing in nature and exhibits a large band gap, while graphite is a soft semi-metal made of two-dimensional gap graphene layers [132, 133]. In spite of these remarkable differences, diamond-graphite composite nanostructures have been reported in the literature [19, 20, 22–24].

Graphitization of diamond occurs, for example, when the system is at high temperature [19, 20]. A mechanism for this graphitization process was proposed by De Vita *et al.* [134]. By performing molecular dynamics simulations of the (111) diamond surface, they observed that the atomic bonds between (111) layers break and the puckered layers flatten to ABC stacked hexagonal graphene planes parallel to the surface. The temperature for graphitization can be decreased by the use of a metal catalyst like Ni [22].

Diamond-graphite hybrid structures also appear in a variety of the systems, such as the epitaxial growth of diamond on graphite edges [135], on stretched diamond nanopillars [136], on polished (110) textured diamond plates [25], or between (113) diamond surfaces [23].

The combination of diamond and graphene results in nanocomposites that are interesting both mechanically and electronically [21, 23, 25]. The superhard diamond provides mechanical strength while the graphene domains enable high fracture toughness [23, 136]. Moreover, the large band gap of the diamond can be tuned by the zero-gap graphene layers. For example, Ref. [25] found that with increasing thickness of graphene, the band gap of diamond-graphite composites decreases to ~ 0.25 eV, and can even become metallic [21]. Similarly, a transition from sp^2 to sp^3 -hybridized atoms in graphite can open a pseudogap in graphite [137].

All the results suggest that a systematical study of diamond-graphite structures is essential to understand the mechanism of transition between diamond and graphite. Unfortunately, existing studies in literature are only focusing on a few interfaces, specifically on the $\{111\}$ [134, 138, 22, 25, 24, 23], $\{112\}$ [135], $\{113\}$ [23] and $\{001\}$ [21, 24, 136] diamond planes. This leaves a large gap in the study of diamond-graphite structures to fill, which motivates the study of this chapter. In Chapter 4, our structural prediction approach for interfaces has succeeded in finding the recurrent patterns in a large family of silicon GBs. In this chapter, we apply this approach to study the reconstructions of interfaces in diamond, and in this study, we focus on the formation of diamond-graphite hybrid structures.

5.2 Reconstructions of diamond interfaces

5.2.1 Reconstructions of (001) diamond interface

In Fig. 5.1 we present the low-energy interfaces containing sp^2 -hybridized atoms in the (001) diamond supercell. The sp^2 -hybridized atom layers are perpendicular to the interface plane and form AA-stacked graphene terminated by sp^3 -hybridized atoms bonded to the (001) diamond planes. The reconstructed interface in Fig. 5.1(a) is consistent with the sp^2 junction designed in a new carbon phase, O20-carbon Ref. [21]. In our results, this junction can be

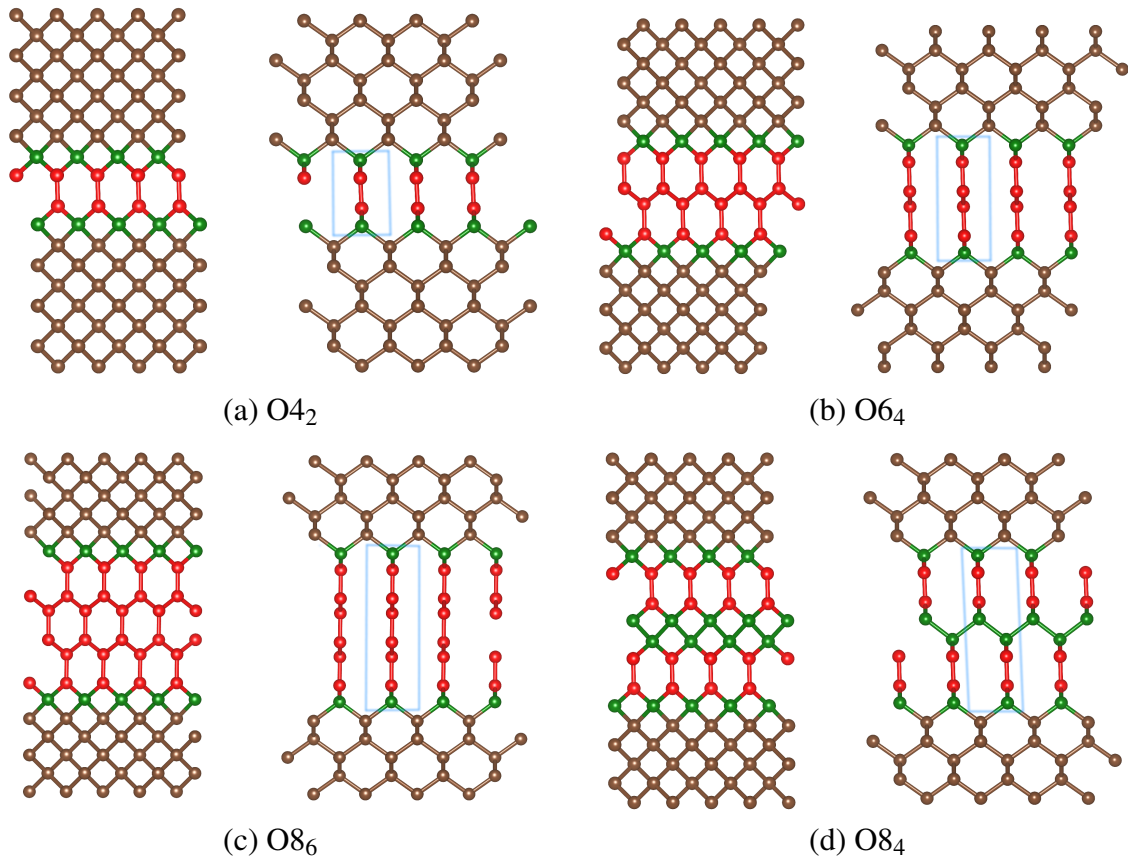


Fig. 5.1 Different reconstructed interfaces containing sp^2 -hybridized layers along the [001] direction. For a better view, each structure is presented along the [100] and $[\bar{1}10]$ directions. The structures are shown in order of increasing total energy. Interface unit cells are indicated by light blue rectangles, sp^2 -hybridized atoms are denoted in red, and sp^3 -hybridized atoms are denoted in green and brown.

regarded as a basic structural unit. The reconstructed interfaces in Fig. 5.1(b) and (c) are extensions of the junction, while the interface shown in Fig. 5.1(d) can be seen as composed of two connected junctions with a dislocation along (001) plane. This so-called O8-carbon structure was reported in the study of bending diamond nanopillars [136].

The structural units of the reconstructed interfaces have orthorhombic symmetry, and they belong to the O-type carbon family [21, 136]. Following the naming rule [21], we use a notation Om_n to name the interfaces, where O indicates orthorhombic symmetry, and m is the number of atoms in the unit cell. We found interfaces with the same number of atoms in the unit cell, but the different number of sp^2 -hybridized atoms. Therefore, we add an additional subscript n indicating the number of sp^2 -hybridized atoms. Based on this naming rule, the interfaces in Fig. 5.1 are labeled as O4₂- (a), O6₄- (b), O8₆- (c) and O8₄-carbon (d). In Table 5.1 we show the bond length of different types of atomic bonds.

We observe that the σ -bonds between sp^3 and sp^2 -hybridized atoms are slightly shorter than the bonds between sp^3 and sp^3 -hybridized atoms in the bulk parts. The C–C double bonds along [001] near the interfaces are compressed, becoming longer and approaching their value in graphite (1.42 Å [139]) closer to the center of the sp^2 -hybridized layers. For example, along the [001] axis the sp^2 – sp^2 bonds in O8₆-carbon near the bulk interfaces are 1.41 Å, while the bonds in the central layer are 1.43 Å. We also note that the sp^2 – sp^2 bonds along the zigzag direction, which extends parallel to the (001) plane, are slightly longer than the bonds in graphite.

| Type of bonds | O4 ₂ | O6 ₄ | O8 ₆ | O8 ₄ |
|----------------------------|-----------------|-----------------|-----------------|-----------------|
| sp^3 – sp^3 | 1.56 | 1.55 | 1.55 | 1.55 |
| sp^2 – sp^3 | 1.49 | 1.49 | 1.49 | 1.49 |
| sp^2 – sp^2 (vertical) | 1.36 | 1.40 | 1.41-1.43 | 1.37 |
| sp^2 – sp^2 (zigzag) | - | 1.43 | 1.43 | - |

Table 5.1 Bond length (in Å) between different hybridized atoms in structures shown in Fig. 5.1. The bond between green–green atoms in O8₄ is 1.58 Å. The C–C bond in bulk diamond is 1.54 Å. The C–C bonds are represented by different notations: sp^3 – sp^3 (the σ bond between the sp^3 -hybridized atoms in the junctions and diamond surfaces, namely the green and brown atoms in Fig. 5.1), sp^2 – sp^3 (the σ bond between sp^2 and sp^3 -hybridized atoms) and sp^2 – sp^2 (the bond between sp^2 -hybridized atoms). Bonds along [001] and $[\bar{1}10]$ axes are indicated with “vertical” and “zigzag” in the parentheses, respectively.

To check the energetic stability of the reconstructed interfaces, we re-optimized the structures with DFT. The energy per atom in the interface region is listed in Table 5.1. The relative energy per atom μ is calculated by the formula $\mu = \Delta E/N_{\text{int}}$, with $\Delta E = E_{\text{tot}} - E_0$ and E_{tot} is the total energy of reconstructed supercell, E_0 is the energy of starting supercell

| Interface | ΔE (eV) | μ (eV/atom) | N_{sp^2} |
|-------------------------|-----------------|-----------------|------------|
| O4 ₂ -carbon | 11.812 | 0.369 | 16 |
| O6 ₄ -carbon | 16.415 | 0.342 | 32 |
| O8 ₆ -carbon | 19.753 | 0.309 | 48 |
| O8 ₄ -carbon | 22.898 | 0.358 | 32 |

Table 5.2 The energy calculated with DFT (GGA-PBE), ΔE is the difference between total energy of the reconstructed interfaces and the starting structure with vacuum, μ is the energy per atom of sp^2 and sp^3 -hybridized atoms and N_{sp^2} is the number of sp^2 -hybridized atoms.

with vacuum, and N_{int} is number of sp^2 -hybridized atoms and the connected sp^3 -hybridized atoms. We find that the structures are relatively stable with small energy per atom μ . As expected, the energy decreases with respect to the length of the graphene layers. For example in O4₂ μ is 0.369 eV/atom and in O8₆ it drops to 0.309 eV/atom. The results suggest that the main instability is raised by the compressed σ bonds and double bonds near the bulk interfaces. Therefore, when the graphene layers are longer, atoms at the interface region become more stable. We can assume that if the graphene layers extend to infinite, the energy per atom will tend to the value of AA-stacked graphite with the same interlayer distance.

Note that, even if μ decreases with the length of graphene layers increasing, the system is still getting more unstable because of the small interlayer distance (2.51 Å) between graphene layers. In Fig. 5.2 we plot the energy per atom in AA- and AB-stacking graphite with respect to the interlayer distance. We see clearly that the energy increases dramatically when the graphene layers get closer. In particular, when the interlayer distances of AA- and AB-stacking graphene layers are less than 2.95 and 2.76 Å, respectively, the cubic diamond becomes more stable than graphite. This is essential for understanding the formation of graphite structures between diamond interfaces.

5.2.2 Reconstructions of interfaces parallel to the [110] axis

The (001) diamond supercell is just one particular case of all interfaces parallel to the [110] axis in the diamond. Now we discuss other cases. In general, we find that the reconstructed interfaces containing graphene layers can be classified into two types: type-I reconstructions where the puckered {111} diamond layers flatten and form hexagonal graphene layers; and type-II reconstructions, where the graphene layers are formed perpendicularly to the interface plane. In this latter case, the length of the graphene layers is usually shorter than in type-I reconstructions.

In Fig. 5.3, we present the two different reconstructed types of diamond-graphite structures in the (112) and (331) supercells. We find that [0001] direction of the formed graphene

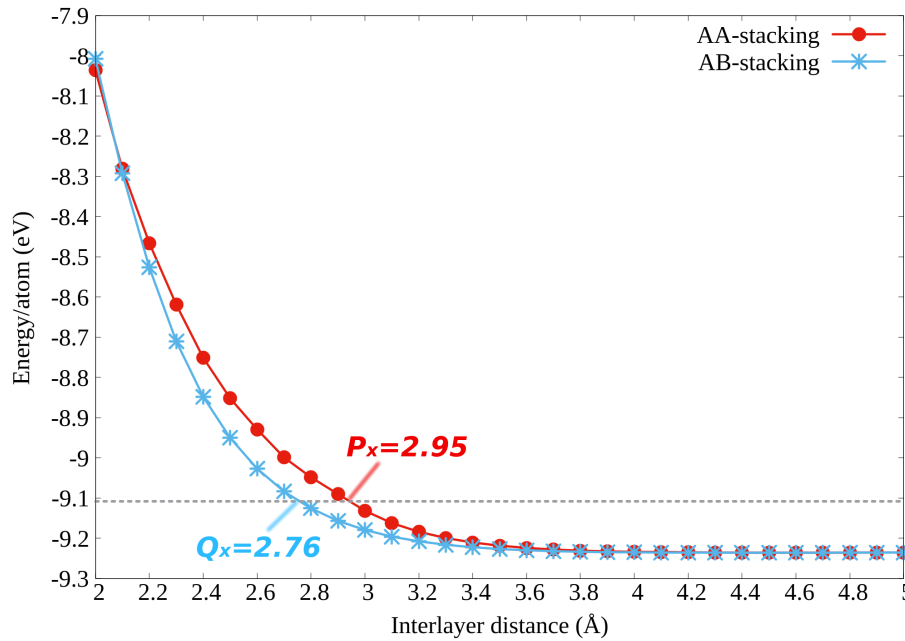


Fig. 5.2 The energy per atom as a function of the interlayer distance in AA- (red line) and AB-stacking (blue line) graphite. The energy is calculated with GGA-PBE, and dashed-line indicates the energy per atom of bulk diamond, -9.109 eV. The cross points of dashed line on AA- and AB-stacking curves are labeled as P_x and Q_x , respectively, and the corresponding interlayer distances are $P_x=2.95$ Å and $Q_x=2.76$ Å.

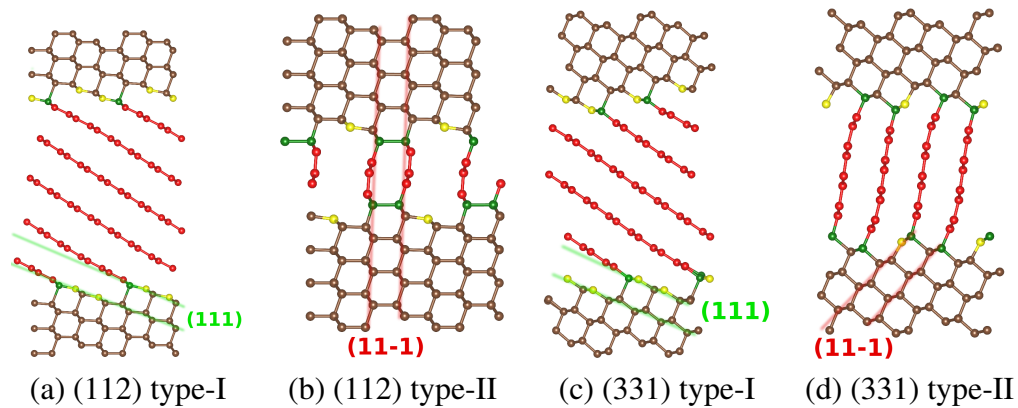


Fig. 5.3 The reconstructed interfaces between (112) planes ((a) and (b)), and (331) planes ((c) and (d)), panels (a) and (c) present the type-I reconstruction, while panels (b) and (d) present the type-II reconstruction. The red atoms indicate the sp^2 -hybridized atoms, brown, green, and yellow atoms are sp^3 -hybridized, where the green atoms are connected to red atoms and yellow atoms are unsaturated. For a clear presentation, the panels show two unit cells of (112) interface along the interface planes. The (111) and $(11\bar{1})$ diamond planes are indicated by green and red lines.

layers is perpendicular to the $[110]$ axis in diamond, and the connecting direction of graphene between the top and bottom bulks interfaces is along the $[1\bar{1}00]$ direction of the graphene plane.

To label the diamond-graphite interface we use the ratio between the number of $\{111\}$ diamond planes and the number of graphene planes connected to them [138, 25]. For example, in Fig. 5.3(a), the ratio is 1 : 1 and the structure is described by a 1 : 1 registry, while Fig. 5.3(b) has a 3 : 2 registry. The study of Ref. [135] suggests that when three $\{111\}$ planes of the diamond match with two $\{0001\}$ planes of graphite the interface strain energy is minimized, leading to a 3 : 2 registry for the diamond-graphite structures with vertical graphene layers. This stabilization was further demonstrated in later studies [138, 25, 22], and in our simulations presented later. But we also find vertical graphene layers forming at the diamond interface with 1 : 1 registry, like the structures present in the (001) supercells discussed in Sec. 5.2.1 and the type-II interface presented in Fig. 5.3(d).

As we mentioned in Sec. 5.2.1, the stability of the graphene layers is highly dependent on the interlayer distance. Therefore, in order to verify the correlation between this distance and the number of graphene layers, we measured this quantity in each reconstructed interface shown in Fig. 5.3. The separations of the graphene layers range from 3.01–3.63 Å in Fig. 5.3(a), 2.62–3.57 Å in Fig. 5.3(b), 2.82–3.42 Å in Fig. 5.3(c) and 2.62–2.72 Å in Fig. 5.3(d). These values are not substantially smaller than the threshold distance for AA-stacking graphite shown in Fig. 5.2, suggesting that these structures are potentially stable. However, if we add an extra graphene layer to the structure depicted in Fig. 5.3(b), connected between the unsaturated (yellow) atoms, the interlayer distance becomes around $3.57/2 = 1.785$ Å, leading to a significant destabilization.

The formation of graphene layers with a 3 : 2 registry could, on one hand, lead to sufficient interlayer distance between the graphene layers and, on the other hand, reduce the number of unsaturated carbon atoms rather than forming a single graphene layer (3 : 1 registry). This can also explain the number of vertical graphene layers on the (111) diamond interface, where the interlayer distance is rather large (4.36 Å [138]). In this case, it is possible to form an extra graphene layer while still allowing for a reasonable value of the interlayer distance reasonable. This leads therefore to a mixture of 2 : 1 and 1 : 1 registries, as reported in experiments [138, 22, 25].

This analysis begets the question if it is possible to predict the registry ratio of diamond-graphite, based on the number of unsaturated diamond atoms at the interface and the distance between the graphene layers. The first step is to figure out the favored atoms for the formation of covalent bonds between graphene and diamond. As an example of this procedure, we take the supercells containing the (112) and (331) interfaces planes, as shown in Fig. 5.4. For

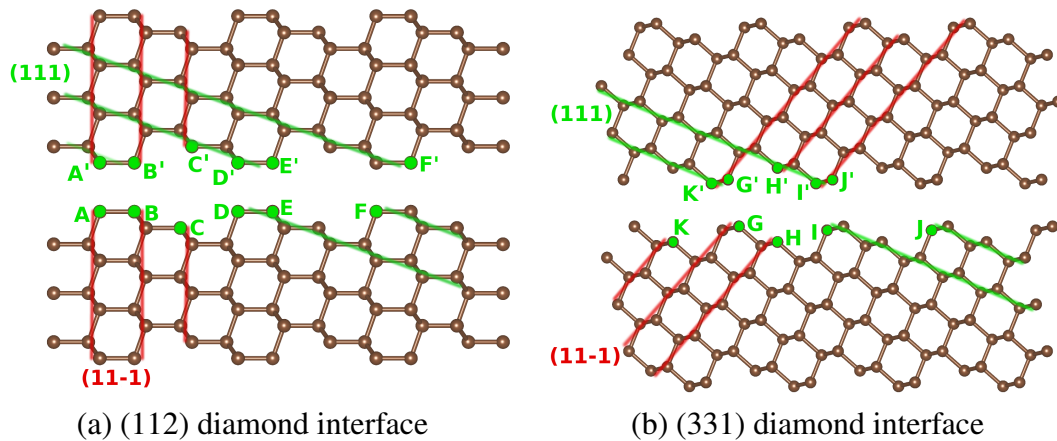


Fig. 5.4 Examples of the initial diamond bulk parts in the supercells with (112) (left panel) and (331) (right panel) interface planes. The bulks parts are put together for a better presentation, as in the actual simulations the interface regions are much larger. The (111) and $(11\bar{1})$ diamond planes are indicated by green and red lines, the atomic positions, where the terminated atoms bind to graphene layers, are highlighted in green and labeled with capital letters.

clarity, we only depict the top and bottom bulk layers, and we indicate the $\{111\}$ diamond planes and the termination atoms.

For the type-I reconstruction of the (112) interface (see Fig. 5.3(a)) the graphene layers are bonded at the A, D, and E atoms on the bottom bulk interface and the B', D', and E' atoms on the top bulk interface. This allows for a stable interlayer distance ranging from 3.01 to 3.63 Å, and for an optimal 1 : 1 registry, that minimizes the number of unsaturated diamond atoms at the interface.

For a type-II reconstruction, the situation is more complicated. Indeed, the distances between the terminal atoms in the (112) interface (see Fig. 5.4(a)) are $|AB| = 1.55$ and $|BC| = 2.19$ Å, making impossible the formation of a 1 : 1 registry. This is not the case, however, for the (331) interface (see Fig. 5.4(b)), where the distances are now $|FG|=3.57$ and $|GH|=2.19$ Å, suggesting that a 1 : 1 registry is indeed capable, with small distortion, of leading to stable structures. This is consistent with our result shown in Fig. 5.3(d), where the interlayer distance varies from 2.62 to 2.72 Å. Of course, the type-II reconstruction is not unique. For example, the lowest energy type-II reconstruction is shown in Fig. 5.3(b), where the graphene layers are bonded between the A and B and the A' and B' atoms on the top and bottom bulk interfaces, respectively. However, and as expected the MHM also finds other type-II structures where the graphene layers are formed between AA' and BC', or AB' and CC' with 3 : 2 registry (see Fig. 5.5). More diamond-graphite structures can be found in Fig. 5.6.

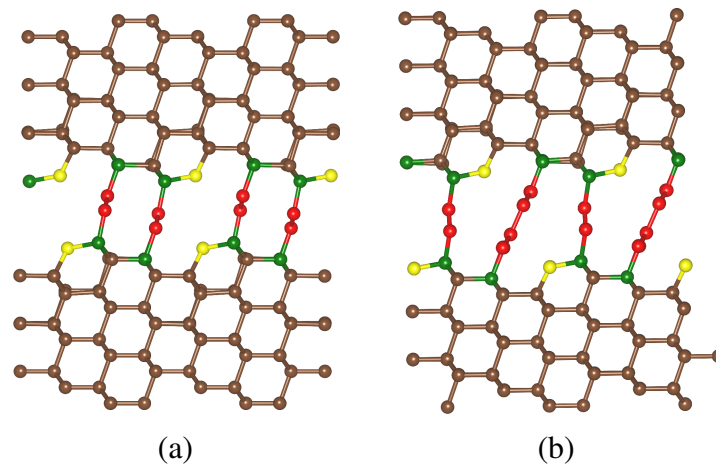


Fig. 5.5 Two type-II reconstructions at (112) interfaces. The red atoms indicate the sp^2 -hybridized atoms, brown, green and yellow atoms are sp^3 -hybridized, where the green atoms are connected to red atoms and yellow atoms are unsaturated. For a clear presentation, the panels show two unit cells of (112) interface along the interface planes.

In summary, the ratio between the number of graphene layers and $\{111\}$ diamond planes tries to reach a registry ratio of 1 : 1, unless the distance between the terminal atoms is too small. This destabilizes the system, leading to registries containing fewer graphene layers per diamond plane.

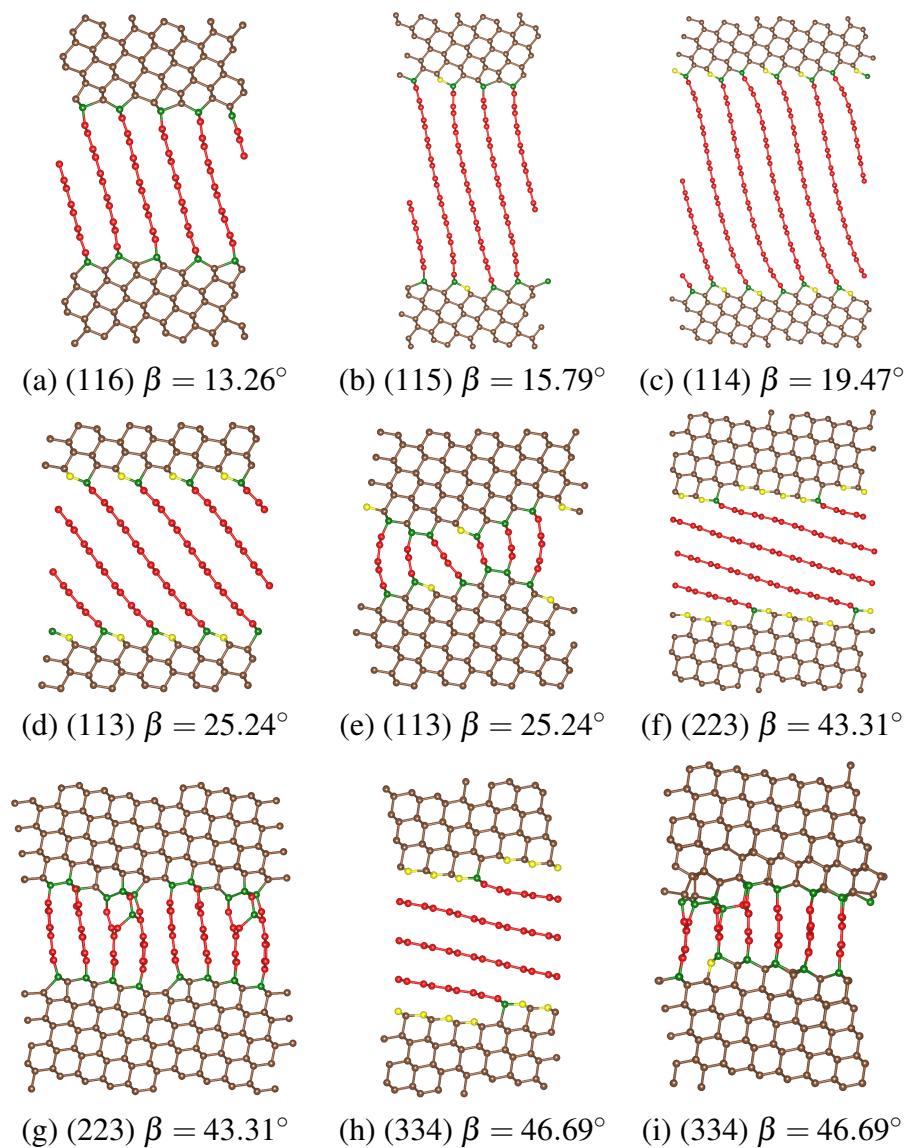


Fig. 5.6 Part-I. Diamond-graphite structures found at interfaces parallel to [110] axis, the structures are labeled by the Miller indices (hkl) of interface planes; β is the angle between interface plane and (001) diamond plane. sp^2 -hybridized atoms are indicated in red, sp^3 -hybridized atoms are in green, yellow and brown, where the green atoms are connected to sp^2 -hybridized atoms and the yellow atoms are unsaturated.

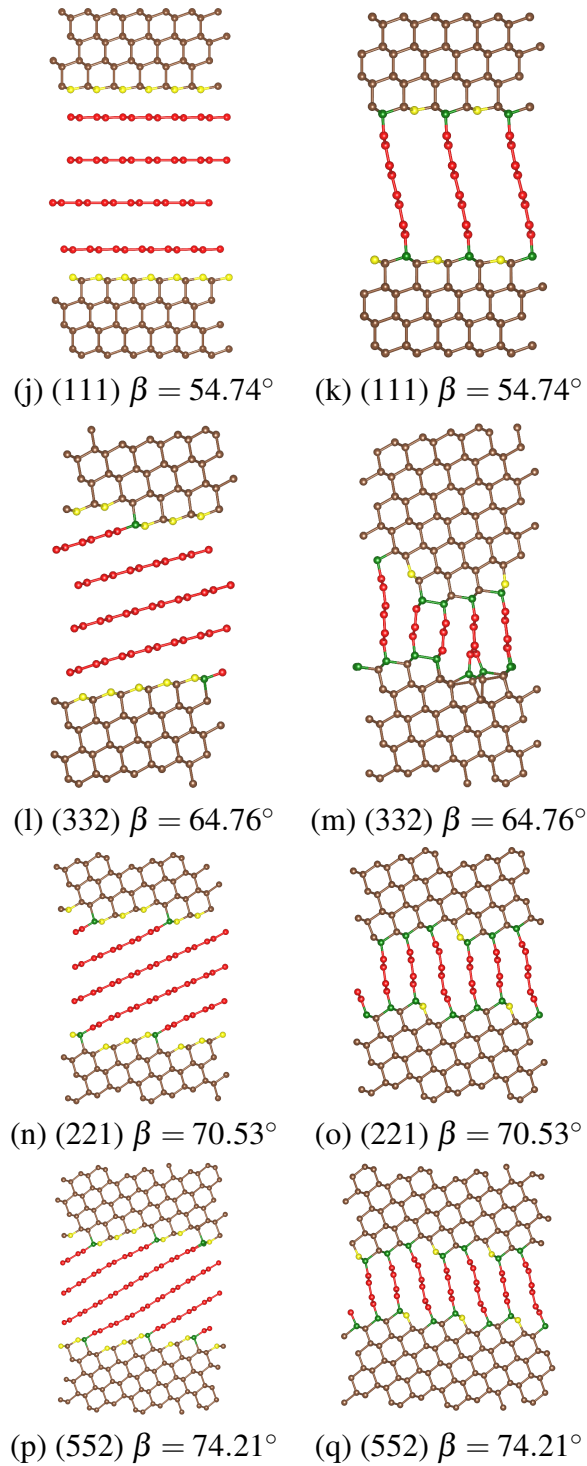


Fig. 5.6 Part-II. Diamond-graphite structures found at interfaces parallel to [110] axis, the structures are labeled by the Miller indices (hkl) of interface planes; β is the angle between interface plane and (001) diamond plane. sp^2 -hybridized atoms are indicated in red, sp^3 -hybridized atoms are in green, yellow and brown, where the green atoms are connected to sp^2 -hybridized atoms and the yellow atoms are unsaturated.

5.2.3 Reconstructions of interfaces parallel to the [100] axis

We now discuss the formation of diamond-graphite structures at interfaces parallel to the [100] axis. We investigate reconstructions for 9 different supercells. As an example, we present in Fig. 5.7(a) to (c) and (d) to (f) the results for the (021) and (031) interfaces, respectively. We find that the graphene layers are more distorted but follow the same reconstructed patterns. In particular, the layers are bonded with the top and bottom {111} diamond planes and can be regarded as an extension of the 111 diamond planes, as shown in Fig. 5.7(b) and (e). Furthermore, the [0001] stacking of the formed graphene layers is nearly parallel to the $[\bar{1}01]$ direction in diamond, as shown in Fig. 5.7(c) and (f). Such reconstruction type, which we find to be stable only between interfaces parallel to [100] axis, has not been previously reported in the literature. Among the interfaces studied in Sec. 5.2.2, we also find similar structures of fractional domains, but with large distortions and high interface energy. In the reconstructed interfaces of the (021) and (031) supercells, the interlayer distance varies from 2.79 to 3.24 Å and from 2.61 to 3.06 Å, respectively. This is in good agreement with the graphite stability region depicted in Fig. 5.2.

In Fig. 5.8, we present the diamond-graphite structures found in other studied interfaces. We find the number of unsaturated atoms at the interface planes is influenced by the planar angle φ between the interface plane and (001) diamond plane. In Table. 5.3 we present the density of unsaturated atoms, $\rho = \frac{N_{\text{unsat}}}{A}$, where N_{unsat} is the number of unsaturated atoms and A is the area of interface. ρ increases with the angle φ .

| Interface | φ | μ (eV) | N_{unsat} | A (Å ²) | ρ |
|-----------|-----------|------------|--------------------|-----------------------|--------|
| (001) | 0 | 0.215 | 0 | 50.74 | 0 |
| (017) | 8.13 | 0.236 | 2 | 45.13 | 0.0443 |
| (015) | 11.31 | 0.262 | 2 | 32.54 | 0.0615 |
| (014) | 14.04 | 0.074 | 2 | 26.31 | 0.0760 |
| (013) | 18.43 | 0.056 | 2 | 20.18 | 0.0991 |
| (025) | 21.80 | 0.098 | 4 | 34.37 | 0.1164 |
| (037) | 23.20 | 0.074 | 6 | 48.60 | 0.1235 |
| (012) | 26.57 | 0.113 | 4 | 28.37 | 0.1410 |
| (035) | 30.96 | 0.037 | 6 | 37.21 | 0.1612 |
| (023) | 33.69 | 0.041 | 4 | 23.01 | 0.1738 |
| (034) | 36.87 | 0.048 | 6 | 31.91 | 0.1880 |

Table 5.3 The angle between interface plane and (001) plane φ , the energy difference per atoms between the reconstructed structure and starting structure at the interface μ . A is the area of the interface, ρ is the density of unsaturated atoms at the interfaces. The energy was calculated with DFTB.

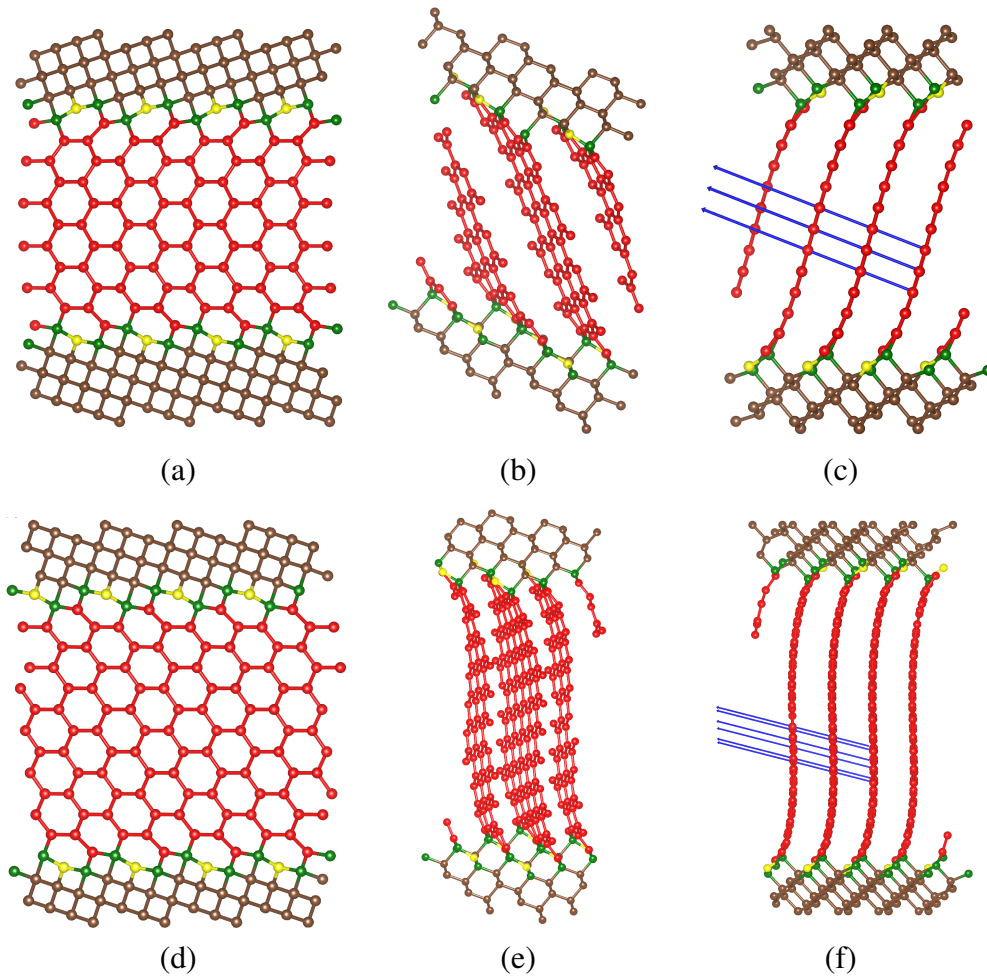


Fig. 5.7 Diamond graphene structures found at (021) and (031) interfaces. (a) and (d): (021) and (031) interfaces viewed along [100] direction; (b) and (e): (021) and (031) interfaces viewed along [110] direction; (c) and (f): rotations of (021) (a) and (031) (d) interfaces viewed counterclockwise with [001] axis with 114° and 122° , respectively, the blue arrow lines present the graphene-stacking directions. Here we present a $2 \times 2 \times 1$ supercells of each structure. sp^2 -hybridized atoms are indicated in red, sp^3 -hybridized atoms are in green, brown, and yellow, where the green atoms are connected to sp^2 -hybridized atoms and yellow atoms are with dangling-bonds.

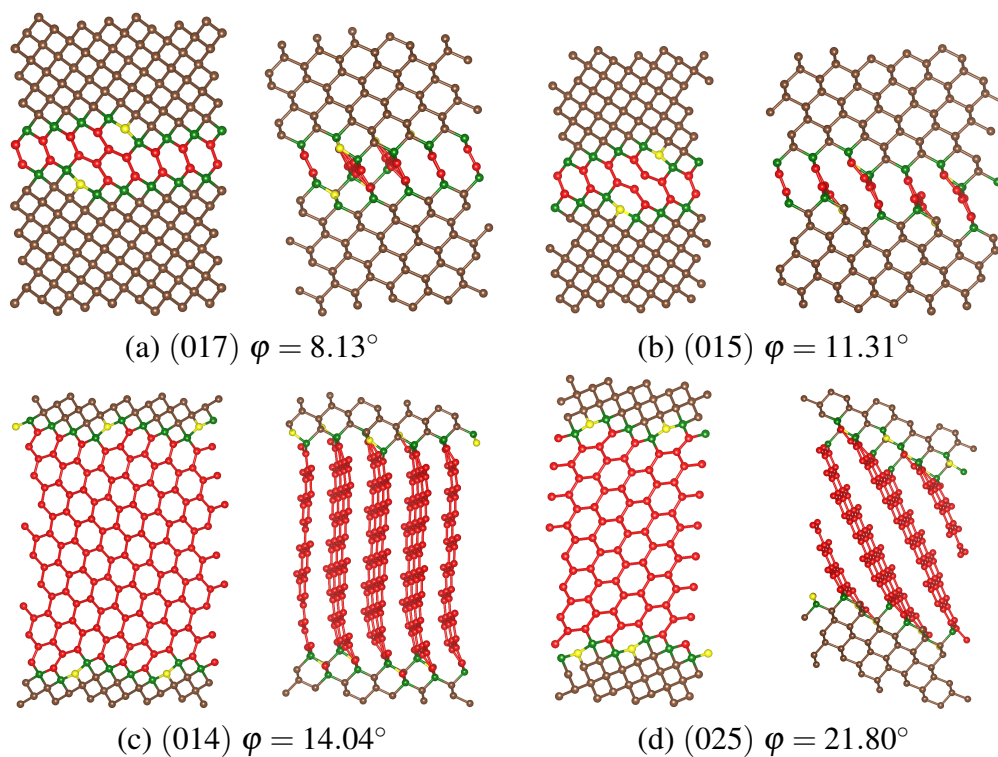


Fig. 5.8 Part-I. Diamond-graphite structures at different studied interfaces. φ is the planar angle between the interface plane and (001) diamond plane. sp^2 -hybridized atoms are indicated in red, sp^3 -hybridized atoms are in green, yellow, and brown, where the green atoms are connected to sp^2 -hybridized atoms and the yellow atoms are unsaturated.

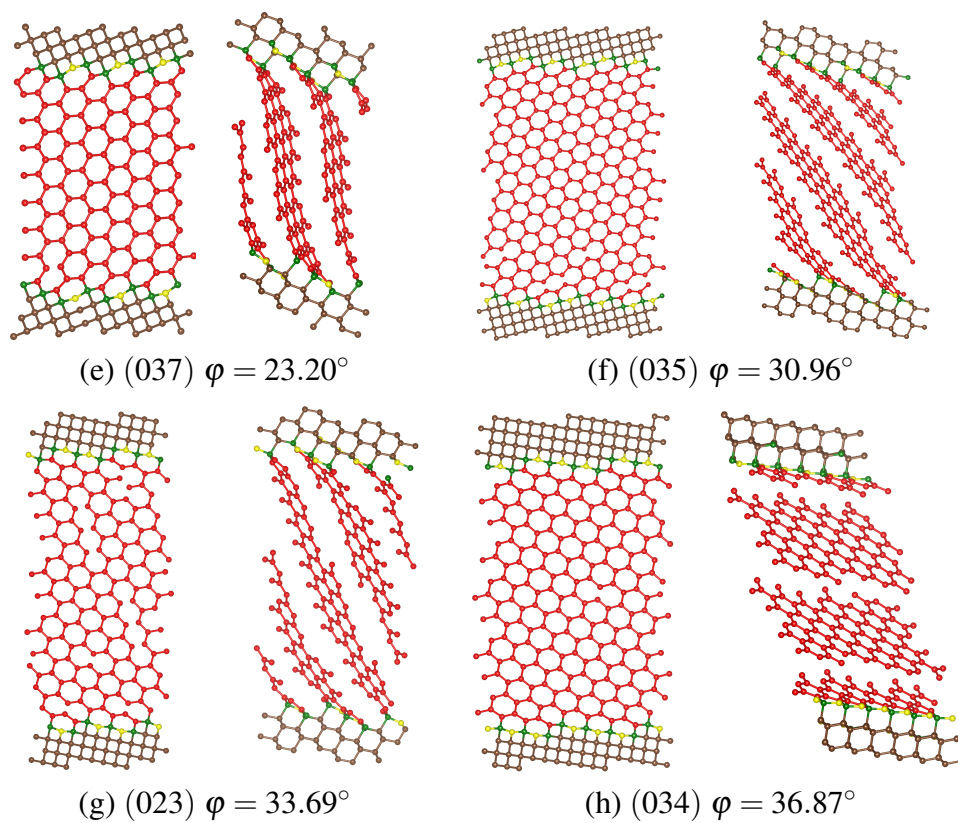


Fig. 5.8 Part-II. Diamond-graphite structures at different studied interfaces. φ is the planar angle between the interface plane and (001) diamond plane. sp^2 -hybridized atoms are indicated in red, sp^3 -hybridized atoms are in green, yellow, and brown, where the green atoms are connected to sp^2 -hybridized atoms and the yellow atoms are unsaturated.

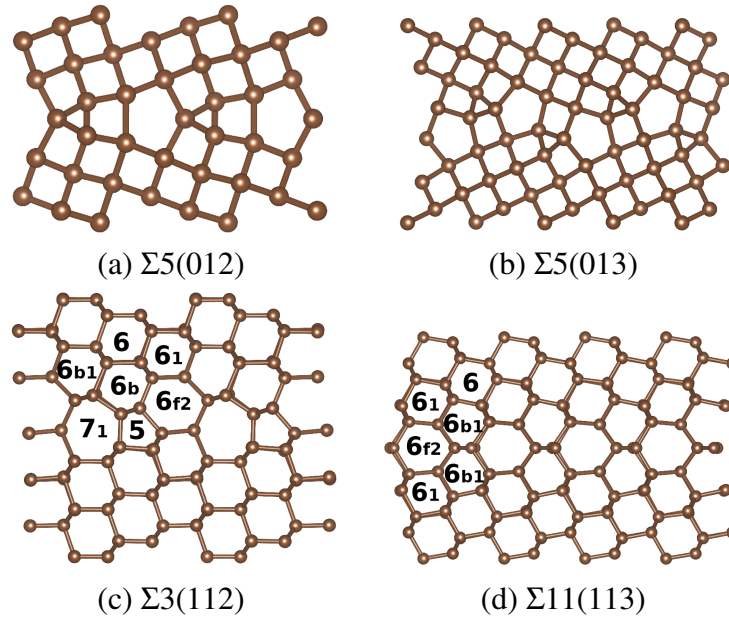


Fig. 5.9 The lowest-energy interfaces found in carbon grain boundaries. (a) $\Sigma 5(021)$ GB; (b) $\Sigma 5(031)$ GB; (c) $\Sigma 3(112)$ GB; (d) $\Sigma 3(113)$ GB. The atomic-ring patterns in GBs with $[110]$ rotation axis are indicated in the panels.

5.3 Diamond-graphite structures in tilt grain boundaries

In this section, we study the interface reconstructions in tilt carbon GBs. In order to be consistent, the supercells of GBs are built in the same way as the Si GBs. We find that the lowest-energy reconstructed interfaces are in good agreement with the recurrent patterns proposed in silicon (Chapter 4). For example, Fig. 5.9 presents the lowest-energy structures found in carbon GBs $\Sigma 5(012)$, $\Sigma 5(013)$, $\Sigma 3(112)$ and $\Sigma 11(113)$, they are consistent with the lowest-energy patterns presented in Table 4.5, 4.2, and 4.3.

The diamond-graphite structures usually appear with much higher energy. The graphene layers formed in GBs with the rotation axis of $[110]$ can also be classified into two types by the extension directions as in Sec. 5.2.2. For example in Fig. 5.10 (a) and (b), we present two examples of interfaces in $\Sigma 3(112)$, for the parts bonded with top bulk layers, the graphene layers are similar to type-I (Fig. 5.3(a)) and type-II (Fig. 5.3(b)) reconstructions, but near the bottom bulk layers, the bonds are in large distortions while for GBs with rotation axis of $[100]$ axis, the graphene layers are more neatly arranged, as shown in Fig. 5.10 (c) and (d), the layers are bent to bonded with the $\{111\}$ diamond planes in the top and bottom bulk layers compared to reconstruction at pure (021) interface (Fig. 5.7(b)). Such bending of graphene layers is because of the misorientation of the two bulk grains that the $\{111\}$ diamond planes are no longer parallel in the top and bottom parts while the graphene layers

are still formed by flattening the puckered $\{111\}$ planes. As a result, the distortions of bonds in $[110]$ GBs or bending of graphene layers in $[100]$ GBs decrease the stability of the diamond-graphite structures in carbon GBs, and it is true that those structures are normally observed at the pure diamond interfaces [138, 25, 23], and in GBs only reported after catalytic transformation [22].

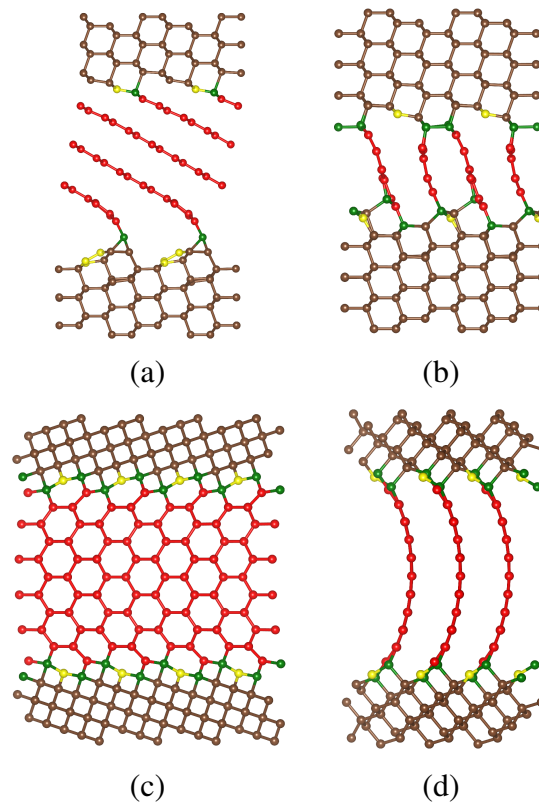


Fig. 5.10 Diamond-graphite structures found in $\Sigma 3(112)$ and $\Sigma 5(021)$ carbon GBs. (a) and (b) are two different types of graphene layers forming at $\Sigma 3(112)$ GB interface. (c) and (d) present the graphitization of $\Sigma 5(021)$ GB interface viewed along $[100]$ direction and a rotation of 114° counterclockwise by $[001]$ axis. sp^2 -hybridized atoms are indicated in red, sp^3 -hybridized atoms are in green, yellow, and brown, where the green atoms are connected to sp^2 -hybridized atoms and the yellow atoms are unsaturated.

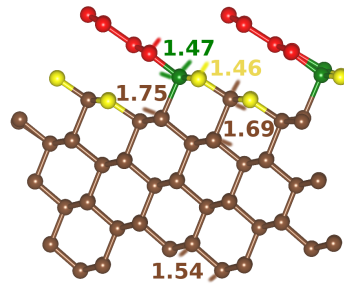


Fig. 5.11 An example of the C–C σ bonds near the bottom bulk surface in (331) type-I reconstructed interface. The red atoms indicate the sp^2 -hybridized atoms, brown, green, and yellow atoms are sp^3 -hybridized, while yellow atoms are unsaturated. The unit of bond length is Å, and the specific bond lengths at the surface are: red–green is 1.47 Å, green–yellow is 1.46 Å (not shown in the figure), yellow–brown is 1.46 Å, brown–brown is 1.69 Å and green–brown is 1.75 Å, the bond in the bulk layer is 1.54 Å.

5.4 Variation of atomic bonds in diamond-graphite

We now turn to discuss how the formation of graphene layers affects the bonds in the supercells. In Sec. 5.2.1 Table 5.1, we notice the σ -bonds between sp^2 and sp^3 -hybridized atoms are usually compressed and the bonds between sp^2 -hybridized atoms are different along armchair and zigzag directions. We find the same features in all the other diamond-graphite structures. We plot the distributions of C–C bond length in type-I and type-II reconstructions of (331) interface and (021) reconstructed interface in Fig. 5.12. As expected, the bonds in the bottom and top bulk parts are kept the same (1.54 Å), since those parts are constrained as rigid bulks, but in the interface region, some of the σ -bonds are under compression, especially the bonds between sp^2 and sp^3 -hybridized carbon atoms and the ones bonded with the unsaturated atoms. Apart from those compressed σ -bonds, stretched bonds are also found between the two neighbor {111} diamond planes at the bulk interfaces. This is because the {111} diamond planes at the interfaces are flat and the bonds between the planes are stretched. In Fig. 5.11 we present an example of the bottom bulk part of the (331) type-I reconstructed interface shown in Fig. 5.3(c). The compressed σ -bonds are about 5% shorter than the C–C bond in bulk diamond (1.54 Å), while the stretched σ -bonds show a maximum length of 1.75 Å, is about 13.6% larger than the bond in the diamond. Our results on compressed bonds are consistent with previous studies: the σ -bonds between sp^2 and sp^3 -hybridized atoms are always compressed [25, 136]. However, in the literature the stretched σ -bonds are ignored, since the diamond-graphite structures are built manually to fit either parameters of bulk diamond [138, 22, 25, 140] or low-energy surface reconstructions [23].

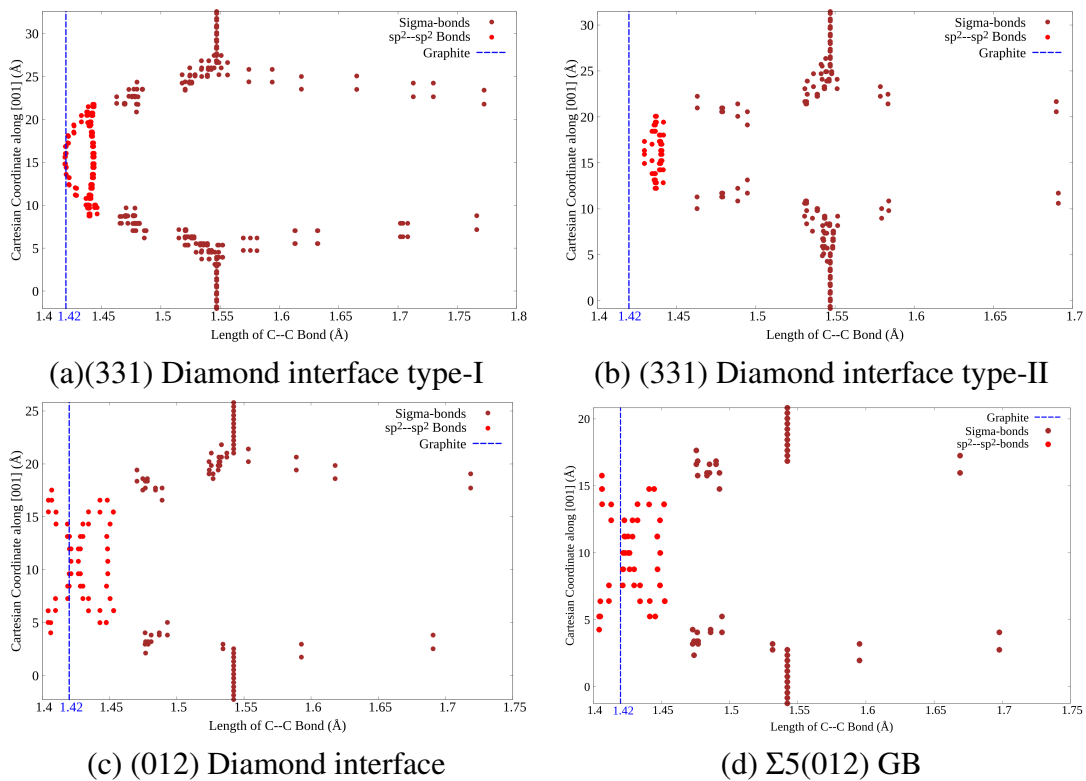


Fig. 5.12 The distributions of bond length along the coordinates of [001] axis. (a) and (b): the two types of reconstructed graphene layers at (331) diamond interfaces; (c) diamond-graphite structure at (012) interface; (d) diamond-graphite structure in $\Sigma 5(012)$ GB. Red points indicate the sp^2-sp^2 bonds, brown points indicate the sp^2-sp^3 and sp^3-sp^3 σ -bonds. The blue vertical dashed line indicates the C-C bond length in graphite, 1.42 Å.

For the sp^2-sp^2 bonds, we notice that the lengths are anisotropic in the graphene layers, especially in type-I [110] and [100] reconstructions. For example in type-I (331) (Fig. 5.12(a)) reconstructed interface, the sp^2-sp^2 bonds which are perpendicular to [110] direction (about 1.42 Å) are shorter than those along zigzag direction parallel to [110] axis (about 1.44 Å). But in type-II (331) (Fig.5.12(b)) reconstructed interface, the discrepancy in bond length of sp^2-sp^2 bonds is small and the bonds are larger than those in graphite.

The distributions of sp^2-sp^2 bonds in the (012) diamond interface and the grain boundary $\Sigma 5(012)$ are similar, although the graphene layers are curved in GB. In contrary to the bonds at (331) interfaces, part of the sp^2-sp^2 bonds near the interface planes are compressed. At the central parts of the graphene layers, those bonds get closer to the value of graphite, while the sp^2-sp^2 bonds along the armchair directions which are parallel to the interface plane are nearly consistent and stretched.

5.5 Electronic properties of diamond-graphite structures

Finally, we discuss the electronic properties of the diamond-graphite structures. Two examples of diamond-graphite structures are chosen, which are formed at the interfaces parallel to [110] and [100] axis, respectively. The calculated DOS of them are shown in Fig. 5.13. We observe metallic characteristics in these diamond-graphite structures that peak electronic states appearing around the Fermi energy. By calculating the partial charge density near the Fermi energy, we see clearly that the electronic density corresponding to the states around the Fermi level is localized at the unsaturated sp^3 -hybridized atoms (see Fig. 5.13(c)) or the sp^2 -hybridized atoms bonded with the atoms on diamond surfaces (see Fig. 5.13(d)). Our results are in good agreement with the previous studies [141, 142] that the π -like graphitic states and the σ -like diamond states result in localized electronic states at the diamond/graphite interface.

We also take another example of diamond-graphite structures which is found at (111) diamond interface to compare the electronic properties. The difference is that we hydrogenate the unsaturated atoms and the sp^2 -hybridized atoms which are connected to the sp^3 -hybridized atoms. As shown in Fig. 5.14, we calculated the DOS, the partial charge density, and roughly plotted the band structures.

We find that: in Fig. 5.14(a), (b), and (c), the structure has a metallic feature that around the Fermi energy there is a peak of electronic states, and those electronic states at the Fermi energy are mainly contributed from the sp^2 -hybridized atoms which are connected to the diamond surface and the unsaturated atoms on the diamond surfaces. Then, in Fig. 5.14(d), (e), and (f), we saturated the dangling-bonded atoms on diamond surfaces with hydrogen

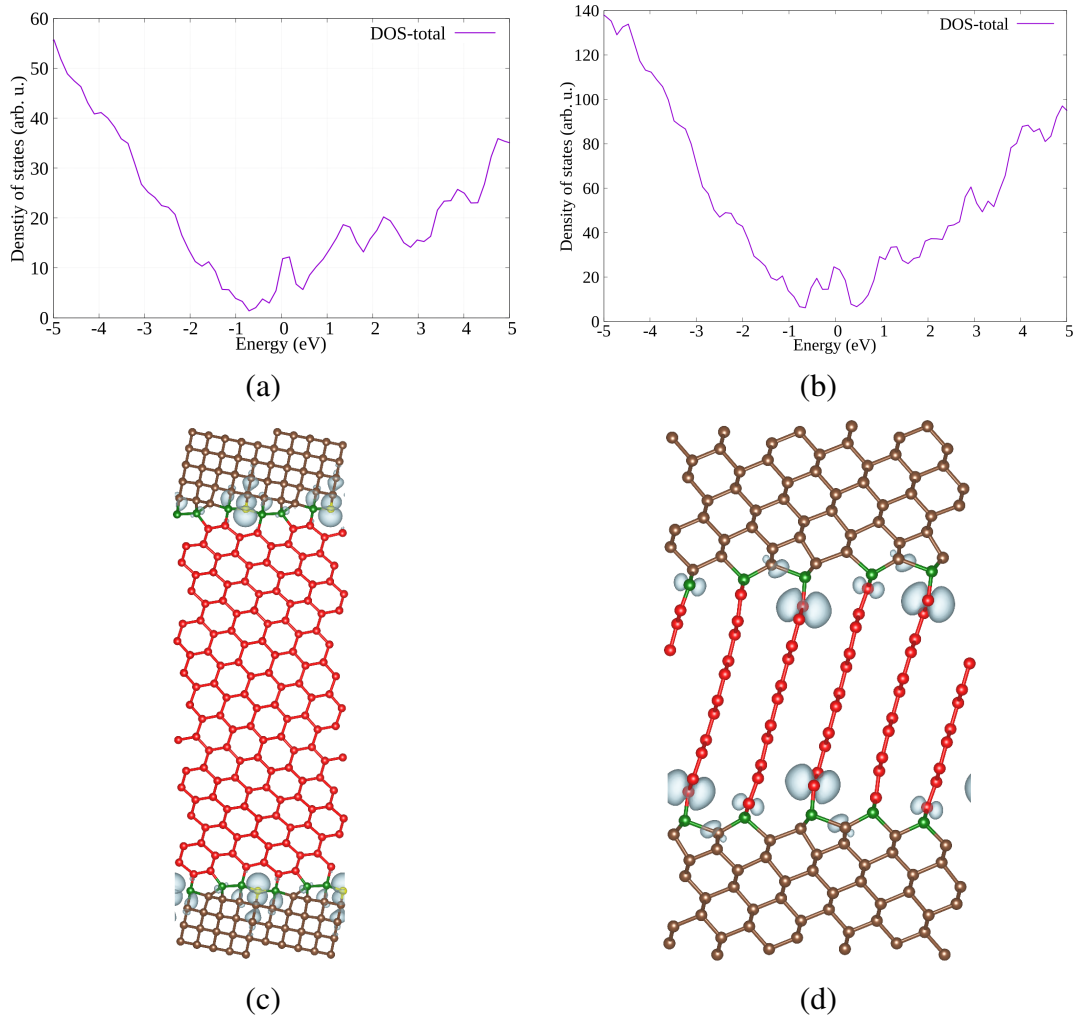


Fig. 5.13 Panels (a) and (b) present the total DOS of the diamond-graphite structures formed at interfaces (032) and (116), respectively. The Fermi energy is set to 0 eV. Panels (c) and (d) present the partial charge density corresponding to the Fermi energy interval from -0.1 to 0.1 eV. Red atoms indicate the sp^2 -hybridized atoms, brown and green atoms indicate sp^3 -hybridized atoms, where green atoms are bonded with the sp^2 -hybridized atoms.

atoms. As a result, the amount of electronic states around the Fermi energy decreases, but it is metallic. The partial charge density (panel (d)) proves that the effects from the unsaturated atoms are eliminated, while the electronic states are from the sp^2 -hybridized atoms that are connected to the diamond surface. Finally, to eliminate the effects from the sp^2 -hybridized atoms near the diamond surfaces, we hydrogenated those atoms, as shown in Fig. 5.14. As we expected, the electronic states around the Fermi energy disappear that the structure present semiconductor feature that it has an indirect bandg ap of 0.34 eV (panel (h)). The results suggest high potential applications of the diamond-graphite structures for electronic devices in the future.

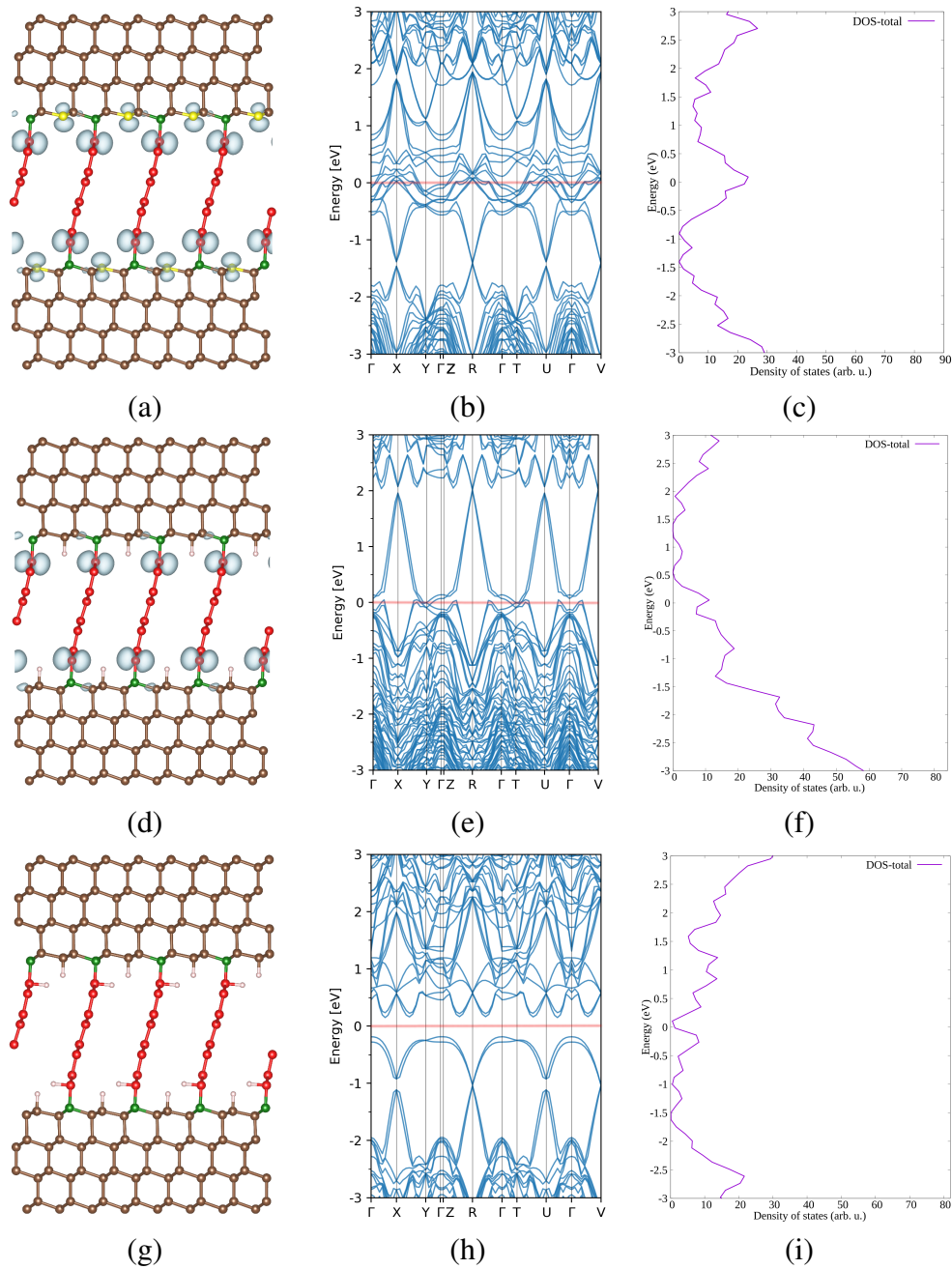


Fig. 5.14 Panel (a) presents the graphite structure formed at (111) diamond interface, while in panels (d) and (g) different number of atoms are hydrogenated. In panels (a) and (d) the partial charge density corresponding to the Fermi energy interval from -0.2 to 0.2 eV are also presented. Panels (b), (e) and (h) present the band structures calculated with GGA-PBE, the red lines indicate the Fermi energy. Panels (c), (f) and (i) show the DOS. The Fermi energy is set to 0 eV in all plots. Red atoms indicate the sp^2 -hybridized atoms, brown, green and yellow atoms indicate sp^3 -hybridized atoms, where green atoms are bonded with the sp^2 -hybridized atoms and yellow atoms are unsaturated. Hydrogen atoms are indicated by pink atoms.

Chapter 6

Structural prediction of point defects in hexagonal silicon

The importance of hexagonal Lonsdaleite silicon-germanium has been growing lately due to its possible uses in optoelectronic devices [143–146, 107, 109]. However, very little is known about defects in the hexagonal phases of group-IV semiconductors. In this chapter, we perform an exhaustive structure prediction study of the most energetically favorable intrinsic defects in Lonsdaleite silicon, using the constrained approach introduced in Chapter 3. In Sec. 6.1, we explain why we are interested in the hexagonal phase of silicon. Then, in Sec. 6.2, the geometric structures of these defects are presented. Finally, in Sec. 6.3, we calculate the density of states of the defective supercells to determine which defects lead to electronic states in the band gap, potentially affecting the performance of optoelectronic devices based on hexagonal group-IV crystals.

6.1 Hexagonal phase is interesting

Most technologically relevant semiconductors crystallize in either a face-centered cubic or a hexagonal closed-packed lattice. These closely related atomic arrangements differ by the stacking of atomic planes: an *ABC* stacking leads to the cubic phase, while the *ABAB* stacking results in a hexagonal symmetry. For an elemental semiconductor, the two phases are commonly labeled as “diamond” and “Lonsdaleite” structure, respectively, while for binary the terminology “zincblende” and “wurtzite” is used. The latter structures are obviously obtained through the coloring of the two sublattices of the former structures.

The energy difference between cubic and hexagonal packing is often very small, so the preferred choice for a certain composition is rather subtle and hard to predict. This is

understandable, as the nearest neighbors and next-nearest neighbors are the same in the ideal wurtzite and zincblende structures. For example, carbon, silicon, germanium, GaAs, etc. have a cubic structure [147, 148], while ZnO, ZnS, CdS, and CdSe are known to crystallize in the hexagonal phase [148].

The ground-state crystal structure of silicon, the most common semiconductor, is the diamond phase. This is perhaps the most studied crystal in solid-state physics, and every imaginable experimental probe or theory has been applied to it. However, many other low-energy phases of silicon, respecting the tetrahedral arrangement of the atoms, are possible [100, 91, 144–146], and some have been experimentally synthesized [149–154].

In recent years, the interest in the Lonsdaleite phase of silicon and germanium has been growing. In fact, several methods have been reported for the growth of hexagonal silicon, such as the diamond anvil cell technique at high pressures [155], the deposition of microcrystallites during laser ablation of SiO₂ films [156], the vapor-liquid-solid method [157, 151], and the crystal structure transfer method [150, 152]. Moreover, the latter method was shown to lead to large and stable regions of the pure hexagonal phase [150].

The importance of the hexagonal phase stems from theoretical calculations that predicted a tunable direct band gap for Si_{1-x}Ge_x alloys [143–146, 107], which can increase the efficiency of light emission for these semiconductors. This has been recently confirmed by Fadaly *et al.* [109] that demonstrated experimentally efficient light emission from direct band-gap hexagonal Ge and SiGe alloys. Furthermore, by controlling the composition of the hexagonal SiGe alloy, they succeeded in changing continuously the emission wavelength over a broad range, while preserving the direct band gap [109]. This seminal result opened the way for the use of group-IV materials in optoelectronic applications.

It is well known that technological applications of semiconductors are extremely sensitive to the presence of defects, and can be seriously hindered, or sometimes even enabled, by them. The defects of cubic silicon have already been extensively studied both experimentally and theoretically. In fact, by now we have a detailed knowledge of which point defects are likely to exist in cubic silicon, their electronic properties, and their influence on functioning optoelectronic devices [26]. However, that knowledge is still to a large extent lacking for its hexagonal counterpart.

It is therefore our objective to fill this gap and perform an extensive study of structure-property relations of point defects in lonsdaleite silicon. In this chapter, we will be focusing on the defect geometries and formations energies at zero temperature, while deferring finite temperature properties to future studies. Supercells are built for the selected point defects and simple local relaxations of the atomic positions are performed at fixed cell parameters. Such an approach is somehow unsatisfactory: in the best case, many defects that are energetically

| Defect | Hexagonal Si Energy (eV) | Cubic Si Energy (eV) |
|------------------------------------|-----------------------------|------------------------------------|
| Fourfold coordinated defect (FFCD) | [2.52, 2.65] | 2.42 [158] |
| Tetrahedral (T) interstitial | [2.52, 2.60] | 4.09 [159], 3.96 [160] |
| Split (X) interstitial | [2.54, 3.27] | 3.31 [158], 3.67 [159], 3.66 [160] |
| Hexagonal (H) interstitial | [2.73, 3.25] | 3.31 [158], 3.77 [159], 3.69 [160] |
| Extended split (EX) interstitial | [3.40, 4.63] | |
| FFCD2 | [3.43, 3.44] | |
| Pentagonal (P) interstitial | [3.52, 4.97] | |
| EX2 interstitial | [3.82, 4.53] | |
| EX3 interstitial | [3.82, 4.68] | |
| Vacancy (V) | 3.78 | 3.17 [158] |
| EX4 interstitial | [3.94, 4.99] | |
| Double (XT) interstitial | [4.11, 4.35] | |
| Frenkel | 4.26 | 4.32 [158] |
| Di-vacancy | [5.48, 6.50] | |

Table 6.1 PBE formation energy (in eV) of the lowest-energy point defects in hexagonal Si, compared (when possible) to the equivalent defect in cubic silicon. The square brackets in the column of hexagonal Si energies denote energy intervals for the possible orientations of each defect. Note that in the hexagonal lattice we obviously can not have a tetrahedral interstitial due to symmetry, but there is a interstitial with similar geometry, so we decided to keep the nomenclature.

unfavored are unnecessarily included in the study, in the worse case relevant low-energy defects are not included. We propose therefore to identify *a priori* the most stable defect configurations using structure prediction. This preliminary step is particularly relevant when new materials are studied – as in this case, where the hexagonal symmetry implies that the number of possible point defects is considerably larger than for cubic silicon – but it can also lead to surprises for well-studied materials. For example, the four-fold coordinated defect (FFCD) of cubic silicon was neglected for a long time in defect studies as it was not stable in force-fields calculations and was only found very late using density functional theory [158].

6.2 Geometric properties of the low-energy point defects

A summary of the lowest-energy point defects stemming from our simulations of hexagonal silicon can be found in Table 6.1, while in Fig. 6.1 we show the geometries of the defects. The crystallographic information files for all defects with energies ranging from 2.52 eV to 7.00 eV.

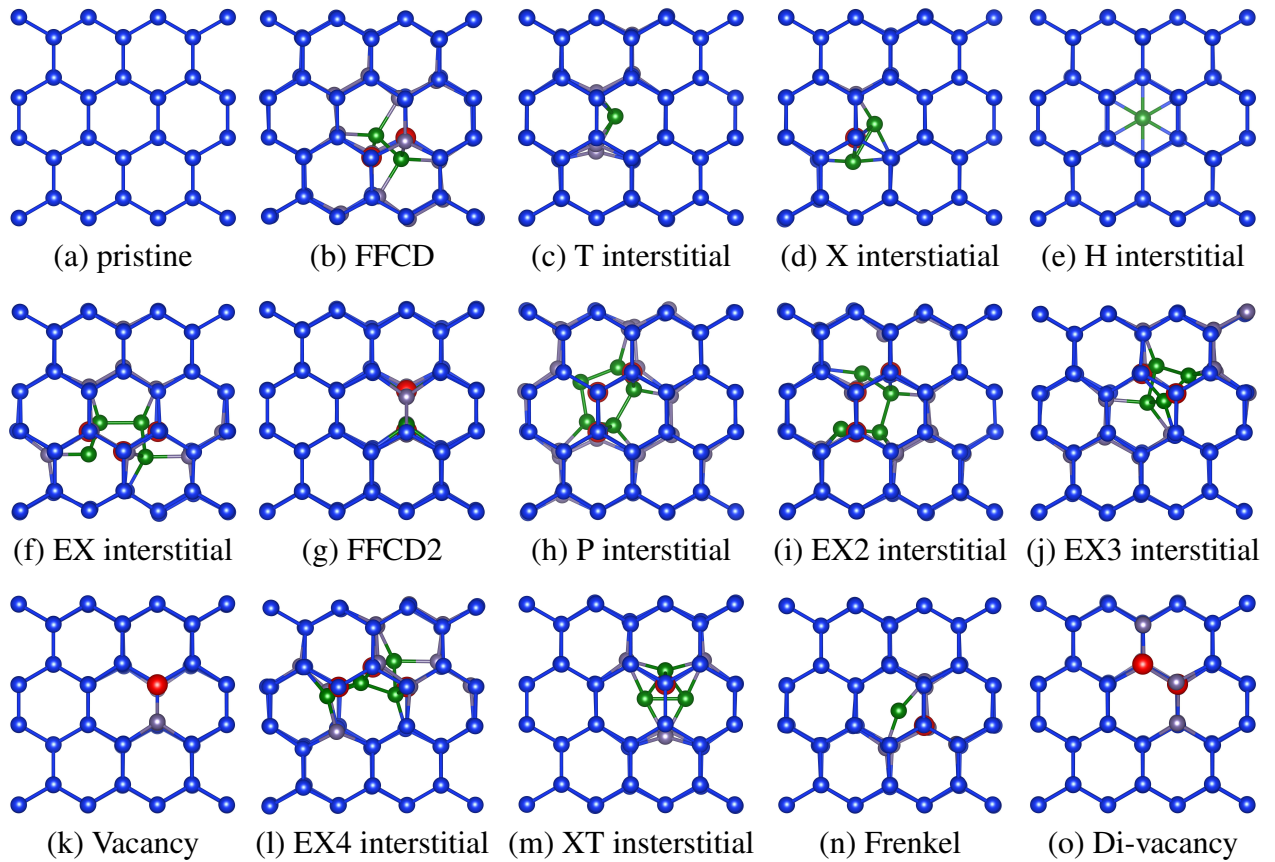


Fig. 6.1 Geometries of the lowest energy defects of hexagonal silicon that stemmed from our simulations. Vacancies are depicted in red, interstitial atoms are in green, while atoms that are slightly displaced from their bulk positions are in grey.

From the analysis of the runs, we found out that our structural prediction runs were able to identify the hexagonal counterparts of all common defects already known for cubic silicon. Furthermore, as the hexagonal lattice contains fewer equivalent sites than the cubic lattice, we found a series of variants of these defects. Note that a similar symmetry breaking has also been observed in some polymorphs of SiC [161, 162].

To make the analysis clearer, we grouped defects with similar spatial arrangements and reported their energy range in Table 6.1. In general, these variant defects can have quite different energies depending on their orientation. For example, we found two split (X) interstitials, oriented along different crystallographic directions, that possess quite different formation energies (2.54 eV and 3.27 eV). Another interesting example is the FFCDD that possesses energy ranging from 2.52 to 3.44 eV, depending on its orientation with respect to the hexagonal c -axis. This anisotropic behavior suggests the possibility to observe in the experimental samples defect alignment along certain crystallographic directions.

Of course, our simulations also yielded a plethora of more complex defects, some of them with energies in the same range as the most common defects. The lowest of these are also listed in Table 6.1. In Table 6.1 we also compare the energy of the well-known point defects of the cubic (diamond) Si lattice [158] with their hexagonal counterparts. Perhaps not surprisingly, the energy to create a single vacancy [see Fig. 6.1(k)] in hexagonal silicon is essentially the same as for the cubic lattice. We also find that removing two neighboring silicon atoms [see Fig. 6.1(o)] is substantially more convenient (by around 2 eV) than creating two isolated vacancies.

The situation is very different for the interstitials, as their energy is considerably lower in the hexagonal phase. This is true for the tetrahedral (T), split (X), hexagonal (H), and extended split (EX) interstitials, with the difference in energy between cubic and hexagonal silicon around 1 eV. These defects are expected therefore to be much more common in samples of hexagonal silicon.

The lowest-energy point defect of hexagonal silicon, as in cubic silicon [158], is the fourfold coordinated defect (FFCD) [see Fig. 6.1(b)]. This defect results from the rotation of two atoms, allowing to preserve the bond lengths and angles with respect to their bulk values, leading to a rather stable configuration. In particular, we observed that when the interstitials are aligned along the $[11\bar{2}0]$ direction they possess lower energy than when aligned along the $[11\bar{2}1]$ direction [see the FFCD2 defect depict in Fig. 6.1(g)].

In terms of formation energy, the second-lowest energy defect is the tetrahedral interstitial [see Fig. 6.1(c)]. We note that, strictly speaking, this defect does not exhibit tetrahedral symmetry, as this is incompatible with the symmetry of the hexagonal lattice. We decided nevertheless to keep the nomenclature to simplify the discussion. The formation of this defect in this lattice requires the displacement of some of its surrounding atoms. The formation energy of this defect in the hexagonal lattice is ≈ 1 eV lower than in the cubic lattice, meaning that this defect becomes as stable as the FFCD.

The X interstitial appears afterwards [see Fig. 6.1(d)]. In the diamond lattice, this defect is usually described as a dumbbell configuration formed by two silicon atoms oriented along the $[110]$ direction [163]. Moreover, a vacancy is located between these interstitials. In the hexagonal lattice, the silicon atoms can orient along the $[11\bar{2}0]$ or the $[11\bar{2}1]$ lattice direction, where the former configuration is more stable.

The H interstitial follows in terms of energy [see Fig. 6.1(e)]. In this defect, the interstitial atom is located at the center of the characteristic hexagons formed by the silicon atoms. The H interstitial is considerably important in Lonsdaleite since its formation energy can be rather small. In fact, we found it to vary from 2.73 eV, when located at the center of an

irregular hexagon, to 3.25 eV, when located at the center of the regular hexagons seen in the c direction. Note that this latter value is close to the energy of this defect in the cubic lattice.

Next comes the EX interstitial [see Fig. 6.1(f)]. Similar to the X interstitial, this defect is also a dumbbell configuration. However, two additional atoms leave their pristine position and form a relatively symmetric “U”-shaped motif with the dumbbell interstitials. In total, three Si-sites are vacant. In the Lonsdaleite the dumbbell interstitials are also oriented along the $[11\bar{2}0]$ direction. We note that the shape of the “U” can change due to the symmetry of the hexagonal lattice. Furthermore, we found several configurations where the atoms did not manage to form this U-shape. Instead, they can fold to form a squared-shape [see Fig. 6.1(j)] or even an L-shape [see Fig. 6.1(l)]. In terms of energy, the U-shaped configurations have the lowest energy, as low as 3.40 eV, while certain configurations of the squared- and L-shape achieve 3.82 and 3.94 eV, respectively. We also observed another higher energy configuration (4.51 eV or higher) resembling the EX, but where two vacancies form a line in the c direction and are closer to one of the dumbbell interstitials.

The simulations with the 288-atom cell also yielded defects that are similar to the X and EX interstitial, the difference being that they possess also one vacant site. In particular, the latter is quite stable [see Fig. 6.1(i)].

The Frenkel defect [Fig. 6.1(n)] occurs when an atom abandons its lattice position in favor of an interstitial position. In both types of lattice, this defect has characteristic energy of around 4.30 eV.

Additionally, we would like to mention a couple of complex defect configurations: one where the interstitials form a pentagonal structure, with 4 vacancies and energy of 3.52 eV [see Fig. 6.1(h)]; the second can be seen either as an FFCD combined with 3 interstitials forming a triangle-shape or as an EX combined with an additional dumbbell interstitial. It has a formation energy of 3.82 eV. Finally, we also found several interesting defects with energies between 4 and 5 eV, including combinations of the aforementioned interstitials, such as the XT di-interstitial [see Fig. 6.1(m)], the hexagonal analogous of the modified triangle, W, and Z di-interstitials [164], and many other complex defects.

We note that the concentration of point defects depends on the free energy of formation, which can be approximated as the sum of the internal energy at zero temperature and the vibrational free energy. For cubic silicon, the calculation of the phonon contribution was performed for the neutral vacancy, the hexagonal and split self-interstitials, and the FFCD defect in Ref. [165], as well as for the vacancy in Ref. [166]. At high temperatures, the vibrational free energy associated with a point defect in silicon is of the order of 1 eV. This stabilization term is especially large for the vacancy and it turns out to be similar for all studied interstitials. We expect a similar situation for the hexagonal system due to its

bonding similarity to cubic silicon. Unfortunately, we have to keep in mind a recent critical study [167] that casts serious doubts on the convergence of calculations of the vibrational free energy.

6.3 Electronic properties of the low-energy point defects

In order to gain some insight into the change of electronic properties induced by the presence of these defects, we computed the density of states (DOS) for the most interesting defect structures. These results are presented in Fig.6.2, where we plot the DOS for selected defects in an energy window around the band gap, as this is the region of most interest for optoelectronics. In all plots, the contribution to the DOS from the bulk region is perfectly visible by comparing to the DOS of pristine hexagonal silicon, depicted as a green line. In most cases, the states associated with the defects are found in the energy region close to the band gap. Note that, for some interstitials, we also find localized states at the bottom of the valence band (not shown).

Both vacancies and di-vacancies can have a profound effect on the electrical properties of Lonsdaleite silicon. In fact, we find several deep states in the gap.

Turning now our attention to defects that do not change the initial number of atoms of the 288-atom cell, we find that the FFCD does not lead to any defect states in the band gap, although we do find a localized state at the bottom of the conduction band. This situation is rather different when the interstitials align along the $[11\bar{2}1]$ direction (as in the FFCD2 structure), as we witness the appearance of a shallow state close to the top of the valence band. Finally, the Frenkel defect has a shallow state at the same position as the FFCD2, and also a localized state close to the bottom of the conduction band. In any case, the high formation energy of this defect is expected to limit its occurrence in experimental samples.

Finally, we analyze the modification to electronic band structure induced by the presence of interstitials. The lowest-energy defect of this kind, the T interstitial, exhibits a localized shallow state in the band gap close to the valence band edge. Both the X and the pentagonal interstitial do not induce electronic states in the band gap, but we can easily identify states coming from these defects in the valence band. The H and XT interstitials have deep states localized approximately in the middle of the band gap. Finally, the EX3 defect leads to defect states both at the top of the valence band and at the bottom of the conduction band. While the XT interstitial has a large formation energy and can be safely disregarded, optimized growth processes should consider reducing the occurrence of H interstitials.

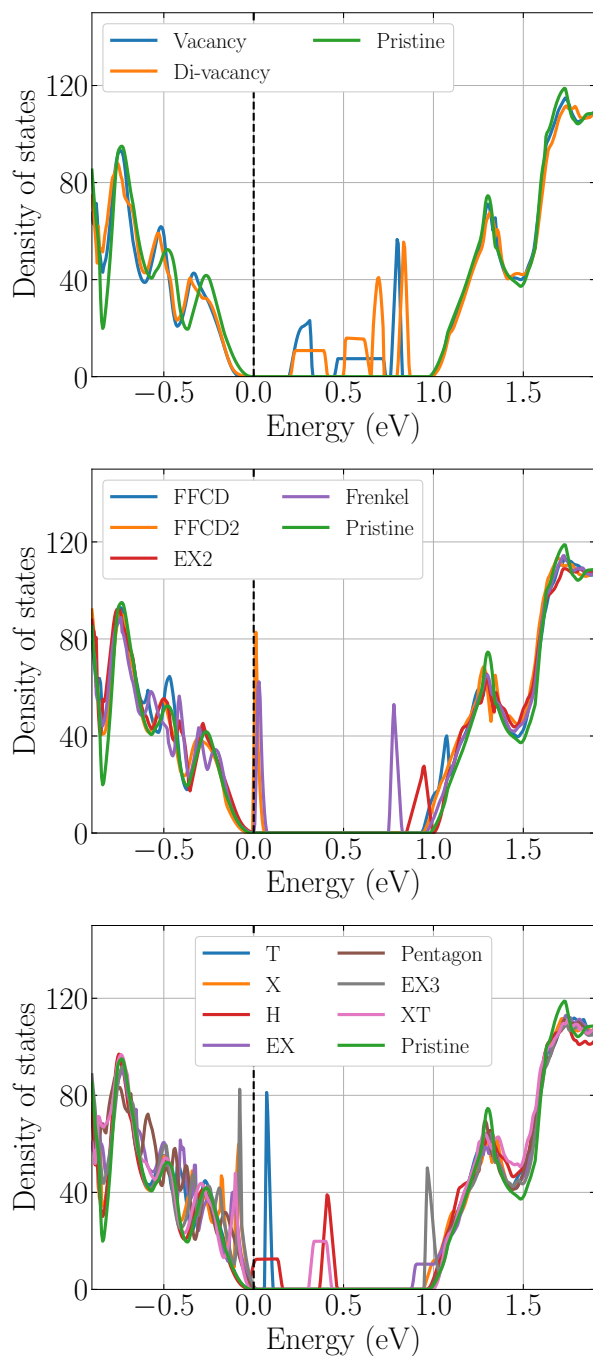


Fig. 6.2 Comparison between the DOS (around the band gap) of the pristine structure and the DOS of the structures containing defects: (top panel) vacancy and di-vacancy, (middle panel) defects conserving the number of atoms, (bottom panel) interstitial defects. All DOS were aligned to a characteristic peak in the valence band. For the pristine structure, this peak is located 3.1 eV below the Fermi level.

Chapter 7

Summary and Conclusions

In this thesis, we presented an efficient constrained structure prediction algorithm to study the structural reconstructions of interfaces and point defects in group-IV elementary crystals. In the following, a brief summary of the main results is presented.

In Chapter 3 we developed an *ab initio* global structural prediction method, which is based on the minima hopping method combined with adequate constraints. Our approach is fully unbiased and is capable of building the lowest-energy reconstructions of interfaces and yielding the atomic configuration of low-energy defects, regardless of the chemistry or the crystal symmetry of the material. Energies and forces are evaluated with tight-binding parameters that can ensure, at the same time, accuracy comparable with the one of density-functional calculations and numerical efficiency. The developed approach is quite general, as it can be used to study GBs or heterogeneous interfaces of any chemical composition, and it can be particularly useful in the investigation of systems with either low symmetry or where defect complexes are expected to play an important role.

Applying our constrained structural prediction approach, we investigated a large family of tilt grain boundaries in silicon in Chapter 4. Our structural prediction approach efficiently reconstructs all interfaces, restoring fourfold coordination, with bond lengths and angles comparable to those in diamond silicon. We note that in many cases, it was essential to add or remove atoms in the interface layer to reach the ground-state structure. We systematically classify the GBs into two types: in type-I GBs, the reconstructed interfaces recover the structures when the number of atoms removed or added is equal to the number of a whole perfect boundary plane. In type-II GBs, the interfaces reach new reconstructions when a plane of atoms is removed or added and they recover the reconstructions of the starting interface only when the number of removed or added atoms is equal to two whole planes of atoms.

The analysis of the recurrent bonding patterns in the GB structures with the lowest interface energies allowed us to classify the reconstructed patterns in few families. In particular, we systematically find single atomic columns in [110] GBs and spiral rings in [100] GBs. Both these defects are electrically benign, as they do not yield states in the band-gap, which could trigger non-radiative electron-hole recombination. On the other hand, we can also find few geometries with relatively low interface energy that contain fivefold coordinated silicon atoms. These defects create localized states in the gap and are therefore expected to deteriorate charge-carrier lifetimes in electronic devices.

By extending the study of low-energy structures to other group-IV elementary crystals (carbon, germanium, and tin), we find that the obtained structural patterns are also stable in Ge and Sn GBs. Furthermore, the GB energy of the same atomic configuration decreases with respect to the atomic number, from C to Sn. The order of the low-energy interfaces in a specific GB is consistent for all group-IV elements except for interfaces with five-fold coordinated atoms. Then, the structures are considerably more unstable in C GBs, while the structures in Ge and Sn GBs are more stable. In some structures, a higher-energy interface in a Si GB even becomes the ground-state structure in Ge and Sn GBs.

Move to Chapter 5, we investigate the reconstructed diamond-graphite hybrid structures in cubic diamond along different interfaces. Our study demonstrated that the graphene layers are formed from the $\{111\}$ diamond planes and between the interfaces parallel to [110] direction, the diamond-graphite structures can be classified into two types by the extended directions of graphene layers, and the number of graphene layers is limited by the distances between the terminated atoms for equilibrium interlayer distances. In type-I reconstructions, the graphene layers are formed by flattening the puckered $\{111\}$ diamond planes and because of the large distances between the terminated atoms, the ratio between graphene layers and connected $\{111\}$ diamond planes is 1 : 1. In type-II reconstructions, the graphene layers are nearly perpendicular to the interface planes and since the distance between terminated atoms is smaller, the ratio between graphene layers and $\{111\}$ diamond planes varies can be 1 : 1 and 2 : 3 or a mixture of both. For the interfaces parallel to the diamond [100] axis, the graphene layers are usually formed only in one pattern, that the layers are terminated at the $\{111\}$ diamond planes and stacking along [-101] direction of the cubic diamond. We also compared the formation of diamond-graphite structures in carbon GBs, that the graphene layers are formed with similar features, but the bonds at the bulk interfaces are largely distorted for GBs of [110] rotation axis, while for GBs of [100] rotations axis the graphene layers are bent by the misorientation of two bulk grains. And these factors explained the rare observations of diamond-graphite structures in carbon grain boundaries.

By comparing the C–C bonds in these structures, we found the σ -bonds are affected by the different hybridizations of atoms, that sp^3 – sp^2 bonds are normally compressed, compared to the bonds in the diamond. And the bonds of unsaturated atoms are also compressed while the bonds between the $\{111\}$ diamond planes are stretched at the interfaces. We also found the C double bonds between sp^2 atoms are dependent on the length of graphene layers, and bonds near the interfaces are smaller than the bonds at the central parts of graphene layers. Furthermore, the sp^2 – sp^2 bonds are anisotropic in the structures because of the limitation of supercell size. The calculations of DOS revealed localized electronic states at the unsaturated atoms of diamond or the sp^2 -hybridized atoms which are connected to the diamond surfaces.

Finally, in Chapter 6 we presented a systematic investigation of the structure of lowest-energy point defects in the Lonsdaleite phase of silicon with our constrained structural prediction method. A plethora of low-energy point defects is identified by us, including the analogous to all relevant defects known for diamond silicon.

A comparison of similar defects in the two hexagonal and cubic lattices reveals that some interstitial defects have lower energy in Lonsdaleite silicon, meaning that they will be more common in synthesized samples of hexagonal silicon than in diamond silicon. We note that in the Lonsdaleite phase, the four-fold coordinated defect, the tetrahedral interstitial, and the split interstitial are the defects with the lowest formation energy (around 2.5 eV), while the vacancy is more than 0.5 eV higher than in cubic silicon. This latter difference is, in our opinion, very important for the emerging hexagonal silicon technology. At typical temperatures where silicon devices are thermally processed (around 1000–1100 K), both interstitials and vacancies seem to exist in roughly equal measure [165]. In fact, although the energy of the vacancy is considerably higher than the one for the interstitials, it is compensated by a larger entropy contribution. Assuming a similar behavior of the entropy for the hexagonal case, we conclude that vacancies should be significantly less common in hexagonal silicon than in its cubic counterpart. Moreover, defects of the hexagonal silicon lattice admit several variants due to symmetry breaking and can have quite different energies depending on their relative orientation in the crystal lattice.

Analysis of the electronic density of states of the structures containing the defects reveals that the fourfold-coordinated defect is electronically benign, but that the tetrahedral and split interstitials exhibit localized shallow states slightly above and below the top of the valence band, respectively. Deep states in the gap were found for the vacancies and for the hexagonal and double interstitials.

References

- [1] Hans Lüth. *Solid surfaces, interfaces and thin films*, volume 4. Springer, 2001. ISBN 978-3-319-10756-1.
- [2] Dieter Wolf and Sidney Yip. *Materials interfaces: atomic-level structure and properties*. Springer Science & Business Media, 1992. ISBN 978-0-412-41270-7.
- [3] G. Palumbo and K.T. Aust. *Materials Interfaces*, chapter Special Properties of Sigma Grain Boundaries, page 190. Chapman & Hall, London, 1990. ISBN 978-0-412-41270-7.
- [4] Arvind Shah, Pedro Torres, Reto Tschärner, Nicolas Wyrsch, and Herbert Keppner. Photovoltaic technology: the case for thin-film solar cells. *Science*, 285(5428):692–698, 1999. ISSN 0036-8075, 1095-9203.
- [5] Craig AJ Fisher and Hideaki Matsubara. The influence of grain boundary misorientation on ionic conductivity in YSZ. *J. Eur. Ceram. Soc.*, 19(6-7):703–707, 1999. ISSN 0955-2219.
- [6] Yonglai Fu. Grain-boundary effects on the electrical resistivity and the ferromagnetic transition temperature of $\text{La}_{0.8}\text{Ca}_{0.2}\text{MnO}_3$. *Appl. Phys. Lett.*, 77(1):118–120, 2000. ISSN 1077-3118, 0003-6951.
- [7] Yukio Sato, Takahisa Yamamoto, and Yuichi Ikuhara. Atomic structures and electrical properties of ZnO grain boundaries. *J. Am. Ceram. Soc.*, 90(2):337–357, 2007. ISSN 1551-2916, 0002-7820.
- [8] Tatsuo Saga. Advances in crystalline silicon solar cell technology for industrial mass production. *NPG Asia Materials*, 2(3):96, 2010. ISSN 1884-4057.
- [9] Fumitada Iguchi, Noriko Sata, and Hiroo Yugami. Proton transport properties at the grain boundary of barium zirconate based proton conductors for intermediate temperature operating SOFC. *J. Mater. Chem.*, 20:6265–6270, 2010. ISSN 1364-5501, 0959-9428.
- [10] Pinshane Y Huang, Carlos S Ruiz-Vargas, Arend M Van Der Zande, William S Whitney, Mark P Levendorf, Joshua W Kevek, Shivank Garg, Jonathan S Alden, Caleb J Hustedt, Ye Zhu, et al. Grains and grain boundaries in single-layer graphene atomic patchwork quilts. *Nature*, 469(7330):389–392, 2011. ISSN 1476-4687.
- [11] Junwen Li, David B Mitzi, and Vivek B Shenoy. Structure and electronic properties of grain boundaries in earth-abundant photovoltaic absorber $\text{Cu}_2\text{ZnSnSe}_4$. *ACS Nano*, 5(11):8613–8619, 2011. ISSN 1936-086X.

- [12] B. Ali, M. Shahram, and S. Saeede. Photovoltaic cells technology: principles and recent developments. *Opt. Quant. Electron.*, 45(2):161–197, 2013. ISSN 1572-817X, 0306-8919.
- [13] Ying Zhou, Liang Wang, Shiyu Chen, Sikai Qin, Xinsheng Liu, Jie Chen, Ding-Jiang Xue, Miao Luo, Yuanzhi Cao, Yibing Cheng, et al. Thin-film Sb_2Se_3 photovoltaics with oriented one-dimensional ribbons and benign grain boundaries. *Nature Photonics*, 9(6):409–415, 2015. ISSN 1749-4893, 1749-4885.
- [14] Rajamani Raghunathan, Eric Johlin, and Jeffrey C Grossman. Grain boundary engineering for improved thin silicon photovoltaics. *Nano Lett.*, 14(9):4943–4950, 2014. ISSN 1530-6992.
- [15] Xiaoliang Wang, Yanyan Zhao, Kristian Mølhave, and Hongyu Sun. Engineering the surface/interface structures of titanium dioxide micro and nano architectures towards environmental and electrochemical applications. *Nanomaterials*, 7(11):382, 2017. ISSN 2079-4991.
- [16] Yaqing Chen, Zhaohe Dai, Chuanxin Weng, Guorui Wang, Xuelu Liu, Xin Cong, Pingheng Tan, Luqi Liu, and Zhong Zhang. Engineering the interface in mechanically responsive graphene-based films. *RSC Adv.*, 8:36257–36263, 2018. ISSN 2046-2069.
- [17] Michael Herbig, P Choi, and Dierk Raabe. Combining structural and chemical information at the nanometer scale by correlative transmission electron microscopy and atom probe tomography. *Ultramicroscopy*, 153:32–39, 2015. ISSN 1879-2723, 0304-3991.
- [18] Hui Gu, Isao Tanaka, Rowland M Cannon, Xiaoqing Pan, and Manfred Rühle. Intergranular glassy phases in the low-CaO-doped HIPed Si_3N_4 ceramics: a review. *Int. J. Mater. Res.*, 101(1):66–74, 2010. ISSN 2195-8556.
- [19] Trevor Evans and P. F. James. A study of the transformation of diamond to graphite. *Proc. R. Soc. Lond.*, A277:260–269, 1964. ISSN 0370-1662.
- [20] Davies G. and Evans. Graphitization of diamond at zero pressure and at a high pressure. *Proc. R. Soc. Lond.*, A328:413–427, 1972. ISSN 0370-1662.
- [21] Yinqiao Liu, Xue Jiang, Jie Fu, and Jijun Zhao. New metallic carbon: Three dimensionally carbon allotropes comprising ultrathin diamond nanostripes. *Carbon*, 126: 601–610, 2018. ISSN 0008-6223.
- [22] Semir Tulić, Thomas Waitz, Mária Čaplovičová, Gerlinde Habler, Marián Varga, Mário Kotlár, Viliam Vretenár, Oleksandr Romanyuk, Alexander Kromka, Bohuslav Rezek, and Viera Skákalová. Covalent diamond–graphite bonding: Mechanism of catalytic transformation. *ACS Nano*, 13(4):4621–4630, 2019. ISSN 1936-086X.
- [23] Péter Németh, Kit McColl, Rachael L. Smith, Mara Murri, Laurence A. J. Garvie, Matteo Alvaro, Béla Pécz, Adrian P. Jones, Furio Corà, Christoph G. Salzmann, and Paul F. McMillan. Diamond-graphene composite nanostructures. *Nano Letters*, 20(5): 3611–3619, 2020. ISSN 1530-6984, 1530-6992.

- [24] Sheng cai Zhu, Xiao zhi Yan, Jin Liu, Artem R. Oganov, and Qiang Zhu. A revisited mechanism of the graphite-to-diamond transition at high temperature. *Matter*, 3(3): 864–878, 2020. ISSN 2590-2385.
- [25] K. P. S. S. Hembram, Sohyung Lee, Hyunsik Im, Hyunsu Ju, Sang-Hun Jeong, and Jae-Kap Lee. The surface hybridization of diamond with vertical graphene: a new route to diamond electronics. *Mater. Horiz.*, 7:470–476, 2020. ISSN 2051-6355.
- [26] Koji Sueoka, Eiji Kamiyama, Piotr Śpiewak, and Jan Vanhellefont. Review—Properties of Intrinsic Point Defects in Si and Ge Assessed by Density Functional Theory. *ECS J. Solid State Sci. Technol.*, 5(4):P3176–P3195, 2016. ISSN 2162-8777, 2162-8769.
- [27] M. Born and R. Oppenheimer. Zur quantentheorie der molekeln. *Annalen der Physik*, 389(20):457–484, 1927. ISSN 0003-3804.
- [28] P. Hohenberg and W. Kohn. Inhomogeneous electron gas. *Phys. Rev.*, 136(3B): B864–B871, nov 1964. ISSN 1536-6065, 0031-899X.
- [29] Robert G. Parr. *Density Functional Theory of Atoms and Molecules*. Springer Netherlands, Dordrecht, 1980. ISBN 978-94-009-9027-2.
- [30] Carlos Fiolhais, Fernando Nogueira, and Miguel AL Marques. *A primer in density functional theory*, volume 620. Springer Science & Business Media, 2003. ISBN 978-3-540-37072-7.
- [31] Helmut Eschrig. *The fundamentals of density functional theory*, volume 2. Springer, 2003. ISBN 978-3-322-97620-8.
- [32] E Eberhard and RM Dreizler. *Density Functional Theory. An Advanced Course*. Springer Berlin, 2011. ISBN 978-3-642-14090-7.
- [33] V. Sahni, J. Gruenebaum, and J. P. Perdew. Study of the density-gradient expansion for the exchange energy. *Phys. Rev. B*, 26:4371–4377, Oct 1982. ISSN 2469-9969, 2469-9950.
- [34] David C. Langreth and M. J. Mehl. Beyond the local-density approximation in calculations of ground-state electronic properties. *Phys. Rev. B*, 28:1809–1834, Aug 1983. ISSN 2469-9969, 2469-9950.
- [35] John P. Perdew and Karla Schmidt. Jacob’s ladder of density functional approximations for the exchange-correlation energy. *AIP Conference Proceedings*, 577(1):1–20, 2001. ISSN 0094-243X, 1551-7616.
- [36] W. Kohn and L. J. Sham. Self-consistent equations including exchange and correlation effects. *Phys. Rev.*, 140:A1133–A1138, Nov 1965. ISSN 1536-6065,0031-899X.
- [37] John P. Perdew and Yue Wang. Accurate and simple analytic representation of the electron-gas correlation energy. *Phys. Rev. B*, 45:13244–13249, Jun 1992. ISSN 2469-9969, 2469-9950.

- [38] J. P. Perdew and Alex Zunger. Self-interaction correction to density-functional approximations for many-electron systems. *Phys. Rev. B*, 23:5048–5079, May 1981. ISSN 2469-9969, 2469-9950.
- [39] S. H. Vosko, L. Wilk, and M. Nusair. Accurate spin-dependent electron liquid correlation energies for local spin density calculations: a critical analysis. *Canadian Journal of Physics*, 58(8):1200–1211, 1980. ISSN 0008-4204, 1208-6045.
- [40] John P Perdew, Kieron Burke, and Matthias Ernzerhof. Generalized gradient approximation made simple. *Phys. Rev. Lett.*, 77(18):3865, 1996. ISSN 1079-7114, 0031-9007.
- [41] E. I. Proynov, S. Sirois, and D. R. Salahub. Extension of the lap functional to include parallel spin correlation. *International Journal of Quantum Chemistry*, 64(4):427–446, 1997. ISSN 1097-461X, 0020-7608.
- [42] Troy Van Voorhis and Gustavo E Scuseria. A novel form for the exchange-correlation energy functional. *The Journal of chemical physics*, 109(2):400–410, 1998. ISSN 1089-7690, 0021-9606.
- [43] Michael Filatov and Walter Thiel. Exchange-correlation density functional beyond the gradient approximation. *Physical Review A*, 57(1):189, 1998. ISSN 1094-1622, 1050-2947.
- [44] John P Perdew, Stefan Kurth, Aleš Zupan, and Peter Blaha. Accurate density functional with correct formal properties: A step beyond the generalized gradient approximation. *Physical review letters*, 82(12):2544, 1999. ISSN 1079-7114, 0031-9007.
- [45] Joseph B Krieger, Jiqiang Chen, Gerald J Iafrate, and Andreas Savin. Construction of an accurate self-interaction-corrected correlation energy functional based on an electron gas with a gap. In *Electron Correlations and Materials Properties*, pages 463–477. Springer, 1999. ISBN 978-1-4615-4715-0.
- [46] Axel D. Becke and Erin R. Johnson. A simple effective potential for exchange. *J. Chem. Phys.*, 124(22):221101, 2006. ISSN 1089-7690, 0021-9606.
- [47] Axel D Becke and Marc R Roussel. Exchange holes in inhomogeneous systems: A coordinate-space model. *Physical Review A*, 39(8):3761, 1989. ISSN 1094-1622, 1050-2947.
- [48] Fabien Tran and Peter Blaha. Accurate band gaps of semiconductors and insulators with a semilocal exchange-correlation potential. *Phys. Rev. Lett.*, 102:226401, Jun 2009. ISSN 1079-7114, 0031-9007.
- [49] Pedro Borlido, Thorsten Aull, Ahmad W. Huran, Fabien Tran, Miguel A. L. Marques, and Silvana Botti. Large-scale benchmark of exchange–correlation functionals for the determination of electronic band gaps of solids. *J. Chem. Theory Comput.*, 15(9): 5069–5079, Jul 2019. ISSN 1549-9626.
- [50] D. Porezag, Th. Frauenheim, Th. Köhler, G. Seifert, and R. Kaschner. Construction of tight-binding-like potentials on the basis of density-functional theory: Application to carbon. *Phys. Rev. B*, 51:12947–12957, May 1995. ISSN 2469-9969, 2469-9950.

- [51] G. Seifert, D. Porezag, and Th. Frauenheim. Calculations of molecules, clusters, and solids with a simplified lcao-dft-lda scheme. *International Journal of Quantum Chemistry*, 58(2):185–192, 1996. ISSN 1097-461X, 0020-7608.
- [52] Pekka Koskinen and Ville Mäkinen. Density-functional tight-binding for beginners. *Computational Materials Science*, 47(1):237–253, Nov 2009. ISSN 0927-0256.
- [53] M. Elstner, D. Porezag, G. Jungnickel, J. Elsner, M. Haugk, Th. Frauenheim, S. Suhai, and G. Seifert. Self-consistent-charge density-functional tight-binding method for simulations of complex materials properties. *Phys. Rev. B*, 58:7260–7268, Sep 1998. ISSN 2469-9969, 2469-9950.
- [54] R. S. Mulliken. Electronic population analysis on lcao–mo molecular wave functions. i. *The Journal of Chemical Physics*, 23(10):1833–1840, 1955. ISSN 0021-9606, 1089-7690.
- [55] Ahmad W. Huran, Conrad Steigemann, Thomas Frauenheim, Bálint Aradi, and Miguel A. L. Marques. Efficient automatized density-functional tight-binding parametrizations: Application to group IV elements. *J. Chem. Theory Comput.*, 14(6):2947–2954, 2018. ISSN 1549-9626.
- [56] Pavel Lejček. *Approaches to Study Grain Boundary Segregation*, pages 25–49. Springer Berlin Heidelberg, Berlin, Heidelberg, 2010. ISBN 978-3-642-12505-8.
- [57] Thibault, Jany, Putaux, Jean-Luc, Jacques, Alain, George, Amand, and Elkajbaji, Mohamed. Plasticity of a silicon bicrystal: a hrem study. *Microsc. Microanal. Microstruct.*, 1(5-6):395–404, 1990. ISSN 1154-2799.
- [58] Sutatch Ratanaphan, Yohan Yoon, and Gregory S. Rohrer. The five parameter grain boundary character distribution of polycrystalline silicon. *J. Mater. Sci.*, 49(14): 4938–4945, 07 2014. ISSN 1573-4803.
- [59] M. L. Kronberg and F. H. Wilson. Secondary recrystallization in copper. *JOM*, 1(8): 501–514, Aug 1949. ISSN 1543-1851.
- [60] H. Grimmer, W. Bollmann, and D. H. Warrington. Coincidence-site lattices and complete pattern-shift in cubic crystals. *Acta Crystallographica Section A*, 30(2): 197–207, Mar 1974. ISSN 2053-2733.
- [61] Jun Chen and Takashi Sekiguchi. Carrier recombination activity and structural properties of small-angle grain boundaries in multicrystalline silicon. *Jpn. J. Appl. Phys.*, 46 (10A):6489–6497, 10 2007. ISSN 1089-7550, 0021-8979.
- [62] A. Voigta, E. Wolfb, and H.P. Strunk. Grain orientation and grain boundaries in cast multicrystalline silicon. *Mater. Sci. Eng. B*, 54(3):202–206, 1998. ISSN 0921-5107.
- [63] B. Gallien, Th. Duffar, S. Lay, and F. Robaut. Analysis of grain orientation in cold crucible continuous casting of photovoltaic Si. *J. Cryst. Growth*, 318(1):208–211, 2011. ISSN 0022-0248.

- [64] S Von Alfthan, PD Haynes, K Kaski, and AP Sutton. Are the structures of twist grain boundaries in silicon ordered at 0 K? *Phys. Rev. Lett.*, 96(5):055505, 2006. ISSN 1079-7114, 0031-9007.
- [65] S. Von Alfthan, K. Kaski, and A. P. Sutton. Order and structural units in simulations of twist grain boundaries in silicon at absolute zero. *Phys. Rev. B*, 74:134101, Oct 2006. ISSN 2469-9969, 2469-9950.
- [66] S. Von Alfthan, K. Kaski, and A. P. Sutton. Molecular dynamics simulations of temperature-induced structural transitions at twist boundaries in silicon. *Phys. Rev. B*, 76:245317, Dec 2007. ISSN 2469-9969, 2469-9950.
- [67] Jian Zhang, Cai-Zhuang Wang, and Kai-Ming Ho. Finding the low-energy structures of Si [001] symmetric tilted grain boundaries with a genetic algorithm. *Phys. Rev. B*, 80:174102, 2009. ISSN 2469-9969, 2469-9950.
- [68] Alvin L.-S. Chua, Nicole A. Benedek, Lin Chen, Mike W. Finnis, and Adrian P. Sutton. A genetic algorithm for predicting the structures of interfaces in multicomponent systems. *Nat. Mater.*, 9:418–422, 2010. ISSN 1476-4660.
- [69] Timofey Frolov, David L. Olmsted, Mark Asta, and Yuri Mishin. Structural phase transformations in metallic grain boundaries. *Nat. Commun.*, 4:1899, 2013. ISSN 2041-1723.
- [70] Xin Zhao, Qiang Shu, Manh Cuong Nguyen, Yangang Wang, Min Ji, Hongjun Xiang, Kai-Ming Ho, Xingao Gong, and Cai-Zhuang Wang. Interface structure prediction from first-principles. *J. Phys. Chem. C*, 118(18):9524–9530, 2014. ISSN 1932-7455, 1932-7447.
- [71] Georg Schusteritsch and Chris J Pickard. Predicting interface structures: From SrTiO₃ to graphene. *Physical Review B*, 90(3):035424, 2014. ISSN 2469-9969, 2469-9950.
- [72] J. Hickman and Y. Mishin. Extra variable in grain boundary description. *Phys. Rev. Mater.*, 1:010601, 06 2017. ISSN 2475-9953.
- [73] A. Stoffers, B. Ziebarth, J. Barthel, O. Cojocaru-Miréidin, C. Elsässer, and D. Raabe. Complex nanotwin substructure of an asymmetric $\Sigma 9$ tilt grain boundary in a silicon polycrystal. *Phys. Rev. Lett.*, 115:235502, 12 2015. ISSN 1079-7114, 0031-9007.
- [74] Qiang Zhu, Amit Samanta, Bingxi Li, Robert E. Rudd, and Timofey Frolov. Predicting phase behavior of grain boundaries with evolutionary search and machine learning. *Nat. Commun.*, 9(1):467, 2018. ISSN 2041-1723.
- [75] Bo Gao, Pengyue Gao, Shaohua Lu, Jian Lv Lv, Yanchao Wang, and Yanming Ma. Interface structure prediction via calypso method. *Science Bulletin*, 64(5):301 – 309, 2019. ISSN 2095-9273.
- [76] Colin W Glass, Artem R Oganov, and Nikolaus Hansen. Uspex—evolutionary crystal structure prediction. *Computer physics communications*, 175(11-12):713–720, 2006. ISSN 0010-4655.

- [77] Andriy O Lyakhov, Artem R Oganov, Harold T Stokes, and Qiang Zhu. New developments in evolutionary structure prediction algorithm uspx. *Computer Physics Communications*, 184(4):1172–1182, 2013. ISSN 0010-4655.
- [78] Sebastian von Althaus, Nicole A. Benedek, Lin Chen, Alvin Chua, David Cockayne, Karleen J. Dudeck, Christian Elsässer, Michael W. Finnis, Christoph T. Koch, Behnaz Rahmati, Manfred Rühle, Shao-Ju Shih, and Adrian P. Sutton. The structure of grain boundaries in strontium titanate: Theory, simulation, and electron microscopy. *Annual Review of Materials Research*, 40(1):557–599, 2010. ISSN 1545-4118.
- [79] T. Frolov, W. Setyawan, R. J. Kurtz, J. Marian, A. R. Oganov, R. E. Rudd, and Q. Zhu. Grain boundary phases in bcc metals. *Nanoscale*, 10:8253–8268, 2018. ISSN 2040-3372.
- [80] Arash Dehghan Banadaki, Mark A. Tschopp, and Srikanth Patala. An efficient monte carlo algorithm for determining the minimum energy structures of metallic grain boundaries. *Computational Materials Science*, 155:466 – 475, 2018. ISSN 0927-0256.
- [81] P. W. Tasker and D. M. Duffy. On the structure of twist grain boundaries in ionic oxides. *Philosophical Magazine A*, 47(6):L45–L48, 1983. ISSN 1460-6992.
- [82] Balint Aradi, Ben Hourahine, and Th Frauenheim. DFTB+, a sparse matrix-based implementation of the DFTB method. *J. Phys. Chem. A*, 111(26):5678–5684, 2007. ISSN 1520-5215, 1089-5639.
- [83] S. Alireza Ghasemi, Maximilian Amsler, Richard G. Hennig, Shantanu Roy, Stefan Goedecker, Thomas J. Lenosky, C. J. Umrigar, Luigi Genovese, Tetsuya Morishita, and Kengo Nishio. Energy landscape of silicon systems and its description by force fields, tight binding schemes, density functional methods, and quantum monte carlo methods. *Phys. Rev. B*, 81:214107, Jun 2010. ISSN 2469-9969, 2469-9950.
- [84] Albert P. Bartók, James Kermode, Noam Bernstein, and Gábor Csányi. Machine learning a general-purpose interatomic potential for silicon. *Phys. Rev. X*, 8:041048, Dec 2018. ISSN 2160-3308.
- [85] Mário R. G. Marques, Jakob Wolff, Conrad Steigemann, and Miguel A. L. Marques. Neural network force fields for simple metals and semiconductors: construction and application to the calculation of phonons and melting temperatures. *Phys. Chem. Chem. Phys.*, 21:6506–6516, 2019. ISSN 1463-9084.
- [86] Stefan Goedecker. Minima hopping: An efficient search method for the global minimum of the potential energy surface of complex molecular systems. *J. Chem. Phys.*, 120(21):9911–9917, 2004. ISSN 1089-7690, 0021-9606.
- [87] Maximilian Amsler and Stefan Goedecker. Crystal structure prediction using the minima hopping method. *J. Chem. Phys.*, 133(22):224104, 2010. ISSN 1089-7690, 0021-9606.
- [88] Ronald Percy Bell. The theory of reactions involving proton transfers. *Proceedings of the Royal Society of London. Series A-Mathematical and Physical Sciences*, 154(882): 414–429, 1936. ISSN 0370-1662.

- [89] MG Evans and M Polanyi. On the introduction of thermodynamic variables into reaction kinetics. *Transactions of the Faraday Society*, 33:448–452, 1937. ISSN 0014-7672.
- [90] Tran Doan Huan, Maximilian Amsler, Miguel A. L. Marques, Silvana Botti, Alexander Willand, and Stefan Goedecker. Low-energy polymeric phases of alanates. *Phys. Rev. Lett.*, 110:135502, 03 2013. ISSN 1079-7114, 0031-9007.
- [91] Maximilian Amsler, Silvana Botti, Miguel A. L. Marques, Thomas J. Lenosky, and Stefan Goedecker. Low-density silicon allotropes for photovoltaic applications. *Phys. Rev. B*, 92:014101, 07 2015. ISSN 2469-9969, 2469-9950.
- [92] Silvana Botti, Maximilian Amsler, José A. Flores-Livas, Paul Ceria, Stefan Goedecker, and Miguel A. L. Marques. Carbon structures and defect planes in diamond at high pressure. *Phys. Rev. B*, 88:014102, 07 2013. ISSN 2469-9969, 2469-9950.
- [93] Pedro Borlido, Conrad Steigemann, Nektarios N Lathiotakis, Miguel A L Marques, and Silvana Botti. Structural prediction of two-dimensional materials under strain. *2D Mater.*, 4(4):045009, 09 2017. ISSN 2053-1583.
- [94] Maximilian Amsler, Silvana Botti, Miguel A. L. Marques, and Stefan Goedecker. Conducting boron sheets formed by the reconstruction of the α -boron (111) surface. *Phys. Rev. Lett.*, 111:136101, 09 2013. ISSN 1079-7114, 0031-9007.
- [95] Pedro Borlido, Claudia Rödl, Miguel A L Marques, and Silvana Botti. The ground state of two-dimensional silicon. *2D Mater.*, 5(3):035010, 04 2018. ISSN 2053-1583.
- [96] G. Kresse and J. Hafner. Ab initio molecular dynamics for liquid metals. *Phys. Rev. B*, 47:558–561, 01 1993. ISSN 2469-9969, 2469-9950.
- [97] Georg Kresse and Jürgen Furthmüller. Efficient iterative schemes for ab initio total-energy calculations using a plane-wave basis set. *Phys. Rev. B*, 54(16):11169, 1996. ISSN 2469-9969, 2469-9950.
- [98] Georg Kresse and D Joubert. From ultrasoft pseudopotentials to the projector augmented-wave method. *Phys. Rev. B*, 59(3):1758, 1999. ISSN 2469-9969, 2469-9950.
- [99] Yubo Zhang, Daniil A Kitchaev, Julia Yang, Tina Chen, Stephen T Dacek, Rafael A Sarmiento-Pérez, Maguel AL Marques, Haowei Peng, Gerbrand Ceder, John P Perdew, et al. Efficient first-principles prediction of solid stability: Towards chemical accuracy. *npj Computational Materials*, 4(1):9, 2018. ISSN 2057-3960.
- [100] Silvana Botti, José A. Flores-Livas, Maximilian Amsler, Stefan Goedecker, and Miguel A. L. Marques. Low-energy silicon allotropes with strong absorption in the visible for photovoltaic applications. *Phys. Rev. B*, 86:121204, Sep 2012. ISSN 2469-9969, 2469-9950.
- [101] Xavier Gonze, Bernard Amadon, P-M Anglade, J-M Beuken, François Bottin, Paul Boulanger, Fabien Bruneval, Damien Caliste, Razvan Caracas, Michel Côté, et al. Abinit: First-principles approach to material and nanosystem properties. *Comput. Phys. Commun.*, 180(12):2582–2615, 2009. ISSN 0010-4655.

- [102] Hiroshi Ogawa. Gbstudio: a builder software on periodic models of CSL boundaries for molecular simulation. *Mater. Trans.*, 47(11):2706–2710, 2006. ISSN 1347-5320, 1345-9678.
- [103] Hendrik J Monkhorst and James D Pack. Special points for brillouin-zone integrations. *Phys. Rev. B*, 13(12):5188–5192, 1976. ISSN 2469-9969, 2469-9950.
- [104] J. Dabrowski and G. Kissinger. Supercell-size convergence of formation energies and gap levels of vacancy complexes in crystalline silicon in density functional theory calculations. *Phys. Rev. B*, 92:144104, Oct 2015. ISSN 2469-9969, 2469-9950.
- [105] Jing Zhu. Ab initio pseudopotential calculations of dopant diffusion in Si. *Comput. Mater. Sci.*, 12(4):309 – 318, 1998. ISSN 0927-0256.
- [106] Jochen Heyd, Gustavo E. Scuseria, and Matthias Ernzerhof. Hybrid functionals based on a screened Coulomb potential. *J. Chem. Phys.*, 118(18):8207–8215, may 2003. ISSN 1089-7690, 0021-9606.
- [107] Claudia Rödl, Jürgen Furthmüller, Jens Renè Suckert, Valerio Armuzza, Friedhelm Bechstedt, and Silvana Botti. Accurate electronic and optical properties of hexagonal germanium for optoelectronic applications. *Phys. Rev. Materials*, 3:034602, Mar 2019. ISSN 2475-9953.
- [108] Jens Renè Suckert, Claudia Rödl, Jürgen Furthmüller, Friedhelm Bechstedt, and Silvana Botti. Efficient strain-induced light emission in lonsdaleite germanium. *Phys. Rev. Materials*, 5:024602, Feb 2021. ISSN 2475-9953.
- [109] Elham M. T. Fadaly, Alain Dijkstra, Jens Renè Suckert, Dorian Ziss, Marvin A. J. van Tilburg, Chenyang Mao, Yizhen Ren, Victor T. van Lange, Ksenia Korzun, Sebastian Kölling, and et al. Direct-bandgap emission from hexagonal ge and sige alloys. *Nature*, 580(7802):205–209, Apr 2020. ISSN 1476-4687.
- [110] M. Boujnah, H. Ennaceri, A. El Kenz, A. Benyoussef, E. Chavira, M. Loulidi, and H. Ez-Zahraouy. The impact of point defects on the optical and electrical properties of cubic ZrO₂. *J. Comput. Electron.*, 19(3):940–946, May 2020. ISSN 1572-8137.
- [111] A. H. Reshak and Sushil Auluck. Influence of an oxygen vacancy on the electronic structure of the asymmetric mixed borate–carbonate Pb₇O(OH)₃(CO₃)₃(BO₃). *RSC Adv.*, 6:18965–18972, 2016. ISSN 2046-2069.
- [112] Xiaohua Liu, Lili Xi, Wujie Qiu, Jiong Yang, Tiejun Zhu, Xinbing Zhao, and Wenqing Zhang. Significant roles of intrinsic point defects in Mg₂X (X = Si, Ge, Sn) thermoelectric materials. *Adv. Electron. Mater.*, 2(2):1500284, 2016. ISSN 2199-160X.
- [113] Norihito Sakaguchi, Hideki Ichinose, and Seiichi Watanabe. Atomic structure of faceted Σ3 CSL grain boundary in silicon: HRTEM and Ab-initio calculation. *Mater. Trans.*, 48(10):2585–2589, 2007. ISSN 1347-5320, 1345-9678.
- [114] A.M. Papon and M. Petit. A survey of the geometrical reconstruction of [011] defects in semiconductors: Grain boundaries and dislocations. *Scr. Metall.*, 19(4):391–396, 1985. ISSN 0036-9748.

- [115] Yadira Arroyo Rojas Dasilva, Rolf Erni, Fabio Isa, Giovanni Isella, Hans von Känel, Pierangelo Gröning, and Marta D. Rossell. Atomic-scale structural characterization of grain boundaries in epitaxial Ge/Si microcrystals by HAADF-STEM. *Acta Mater.*, 167:159–166, 2019. ISSN 1359-6454.
- [116] Benedikt Ziebarth, Matous Mrovec, Christian Elsässer, and Peter Gumbsch. Interstitial iron impurities at grain boundaries in silicon: A first-principles study. *Phys. Rev. B*, 91:035309, 01 2015. ISSN 2469-9969, 2469-9950.
- [117] H.-J. Möller. $\langle 011 \rangle$ tilt boundaries in the diamond cubic lattice. *Philos. Mag. A*, 43(4):1045–1055, 1981. ISSN 1460-6992.
- [118] Yaogang Zhang, Hideki Ichinose, megumi nakanose, Kunio Ito, and Yoichi Ishida. Structure modelling of σ_3 and σ_9 coincident boundaries in CVD diamond thin films. *J. Electron Microsc.*, 48(3):245–251, 01 1999. ISSN 0022-0744.
- [119] A. A. Nazarov, O. A. Shenderova, and D. W. Brenner. Elastic models of symmetrical $\langle 001 \rangle$ and $\langle 011 \rangle$ tilt grain boundaries in diamond. *Phys. Rev. B*, 61:928–936, 2000. ISSN 2469-9969, 2469-9950.
- [120] M. F. Chisholm, A. Maiti, S. J. Pennycook, and S. T. Pantelides. Atomic configurations and energetics of arsenic impurities in a silicon grain boundary. *Phys. Rev. Lett.*, 81:132–135, 07 1998. ISSN 1079-7114, 0031-9007.
- [121] M Kohyama, R Yamamoto, Y Ebata, and M Kinoshita. The atomic and electronic structure of a (001) tilt grain boundary in Si. *J. Phys. C: Solid State Physics*, 21(17):3205, 1988. ISSN 0022-3719.
- [122] J. R. Morris, Z.-Y. Lu, D. M. Ring, J.-B. Xiang, K.-M. Ho, C. Z. Wang, and Chong-Long Fu. First-principles determination of the $\Sigma = 13$ $\{510\}$ symmetric tilt boundary structure in silicon and germanium. *Phys. Rev. B*, 58:11241–11245, 11 1998. ISSN 2469-9969, 2469-9950.
- [123] Bin Chen, Jun Chen, Takashi Sekiguchi, Mitsuhiro Saito, and Koji Kimoto. Structural characterization and iron detection at $\Sigma 3$ grain boundaries in multicrystalline silicon. *J. Appl. Phys.*, 105(11):113502, 2009. ISSN 1089-7550, 0021-8979.
- [124] Quan Li, Yanming Ma, Artem R. Oganov, Hongbo Wang, Hui Wang, Ying Xu, Tian Cui, Ho-Kwang Mao, and Guangtian Zou. Superhard monoclinic polymorph of carbon. *Phys. Rev. Lett.*, 102:175506, Apr 2009. ISSN 1079-7114, 0031-9007.
- [125] Jian-Tao Wang, Changfeng Chen, and Yoshiyuki Kawazoe. Low-temperature phase transformation from graphite to sp^3 orthorhombic carbon. *Phys. Rev. Lett.*, 106:075501, Feb 2011. ISSN 1079-7114, 0031-9007.
- [126] V. G. Kumar. Das, Lo Kong. Mun, Chen. Wei, and Thomas C. W. Mak. Synthesis, spectroscopic study, and x-ray crystal structure of bis[3-(2-pyridyl)-2-thienyl-c,n]diphenyltin(IV): the first example of a six-coordinate tetraorganotin compound. *Organometallics*, 6(1):10–14, 1987. ISSN 1520-6041, 0276-7333.

- [127] Vadapalli Chandrasekhar, Selvarajan Nagendran, and Viswanathan Baskar. Organotin assemblies containing sn-o bonds. *Coordination Chemistry Reviews*, 235(1):1 – 52, 2002. ISSN 0010-8545.
- [128] Masaichi Saito, Sanae Imaizumi, Tomoyuki Tajima, Kazuya Ishimura, and Shigeru Nagase. Synthesis and structure of pentaorganostannate having five carbon substituents. *Journal of the American Chemical Society*, 129(36):10974–10975, 2007. ISSN 1520-5126, 0002-7863.
- [129] Hans J. Reich and Nancy H. Phillips. Lithium-metalloid exchange reactions. observation of lithium pentaalkyl(aryl) tin ate complexes. *Journal of the American Chemical Society*, 108(8):2102–2103, 1986. ISSN 0002-7863.
- [130] Alfredo A Correa, Stanimir A Bonev, and Giulia Galli. Carbon under extreme conditions: phase boundaries and electronic properties from first-principles theory. *Proc. Natl. Acad. Sci. U S A*, 103:1204–1208, Jan 2006. ISSN 1091-6490.
- [131] Timofey Frolov, David L. Olmsted, Mark Asta, and Yuri Mishin. Structural phase transformations in metallic grain boundaries. *Nature Communications*, 4:1899, May 2013. ISSN 2041-1723.
- [132] A. K. Geim and K. S. Novoselov. The rise of graphene. *Nature Materials*, 6(3): 183–191, Mar 2007. ISSN 1476-4660.
- [133] A. K. Geim. Graphene: Status and prospects. *Science*, 324(5934):1530–1534, 2009. ISSN 1095-9203, 0036-8075.
- [134] A microscopic model for surface-induced diamond-to-graphite transitions. *Nature*, 379:523–526, 1996. ISSN 1476-4687.
- [135] Walter R. L. Lambrecht, Choon H. Lee, Benjamin Segall, John C. Angus, Zhidan Li, and Mahendra Sunkara. Diamond nucleation by hydrogenation of the edges of graphitic precursors. *Nature*, 364:607–610, 1993. ISSN 1476-4687.
- [136] Blake Regan, Alireza Aghajamali, Johannes Froech, Toan Trong Tran, John Scott, James Bishop, Irene Suarez-Martinez, Ying Liu, Julie M. Cairney, Nigel A Marks, Milos Toth, and Igor Aharonovich. Plastic deformation of single-crystal diamond nanopillars. *Advanced Materials*, 32(9):1906458, 2020. ISSN 1521-4095.
- [137] Hiromasa Ohnishi and Keiichiro Nasu. Photoinduced domain-type collective structural changes with interlayer σ -bonds in the visible region of graphite. *Phys. Rev. B*, 79: 054111, Feb 2009. ISSN 2469-9969, 2469-9950.
- [138] Jae-Kap Lee, Seung-Cheol Lee, Jae-Pyoung Ahn, Soo-Chul Kim, John I. B. Wilson, and Phillip John. The growth of aa graphite on (111) diamond. *The Journal of Chemical Physics*, 129(23):234709, 2008. ISSN 1089-7690.
- [139] S. ERGUN. Structure of graphite. *Nature Physical Science*, 241(107):65–67, Jan 1973. ISSN 2058-1106.

- [140] Xigui Yang, Jiajun Dong, Mingguang Yao, Kuo Hu, Huanhuan Sun, Ran Liu, Chong-Xin Shan, and Bingbing Liu. Diamond-graphite nanocomposite synthesized from multi-walled carbon nanotubes fibers. *Carbon*, 172:138–143, 2021. ISSN 0008-6223.
- [141] A.T. Balaban, D.J. Klein, and C.A. Folden. Diamond-graphite hybrids. *Chemical Physics Letters*, 217(3):266–270, 1994. ISSN 0009-2614.
- [142] Alessandro De Vita, Giulia Galli, Andrew Canning, and Roberto Car. A microscopic model for surface-induced diamond-to-graphite transitions. *Nature*, 379(6565):523–526, Feb 1996. ISSN 1476-4687.
- [143] C. Raffy, J. Furthmüller, and F. Bechstedt. Properties of hexagonal polytypes of group-IV elements from first-principles calculations. *Phys. Rev. B*, 66:075201, Aug 2002. ISSN 2469-9969, 2469-9950.
- [144] J. D. Joannopoulos and Marvin L. Cohen. Electronic properties of complex crystalline and amorphous phases of Ge and Si. I. Density of States and Band Structures. *Phys. Rev. B*, 7:2644–2657, Mar 1973. ISSN 2469-9969, 2469-9950.
- [145] J. D. Joannopoulos and Marvin L. Cohen. Electronic properties of complex crystalline and amorphous phases of Ge and Si. II. Band Structure and Optical Properties. *Phys. Rev. B*, 8:2733–2755, Sep 1973. ISSN 2469-9969, 2469-9950.
- [146] Amrit De and Craig E Pryor. Electronic structure and optical properties of Si, Ge and diamond in the lonsdaleite phase. *J. Phys. Condens. Matter.*, 26(4):045801, Jan 2014. ISSN 1361-648X, 0953-8984.
- [147] Marvin L. Cohen and James R. Chelikowsky. Diamond and Zinc-Blende structure semiconductors. In *Electronic Structure and Optical Properties of Semiconductors*, pages 79–139. Springer, 1988. ISBN 978-3-642-97080-1.
- [148] F. H. Allen, G. Gergerhoff, and R. Sievers, editors. *Crystallographic databases*. International Union of Crystallography, Chester, 1987.
- [149] Duck Young Kim, Stevce Stefanoski, Oleksandr O. Kurakevych, and Timothy A. Strobel. Synthesis of an open-framework allotrope of silicon. *Nat. Mater.*, 14(2): 169–173, Nov 2014. ISSN 1476-4660.
- [150] Håkon Ikaros T. Hauge, Marcel A. Verheijen, Sonia Conesa-Boj, Tanja Etzelstorfer, Marc Watzinger, Dominik Kriegner, Ilaria Zardo, Claudia Fasolato, Francesco Capitani, Paolo Postorino, and et al. Hexagonal silicon realized. *Nano Lett.*, 15(9): 5855–5860, Aug 2015. ISSN 1530-6992.
- [151] J. Tang, J.-L. Maurice, F. Fossard, I. Florea, W. Chen, E. V. Johnson, M. Foldyna, L. Yu, and P. Roca i Cabarrocas. Natural occurrence of the diamond hexagonal structure in silicon nanowires grown by a plasma-assisted vapour–liquid–solid method. *Nanoscale*, 9:8113–8118, 2017. ISSN 2040-3372.
- [152] Yizhen Ren, Philipp Leubner, Marcel A Verheijen, Jos E M Haverkort, and Erik P A M Bakkers. Hexagonal silicon grown from higher order silanes. *Nanotechnology*, 30(29):295602, Apr 2019. ISSN 1361-6528, 0957-4484.

- [153] Silvia Pandolfi, Carlos Renero-Lecuna, Yann Le Godec, Benoit Baptiste, Nicolas Menguy, Michele Lazzeri, Christel Gervais, Kristina Spektor, Wilson A. Crichton, and Oleksandr O. Kurakevych. Nature of Hexagonal Silicon Forming via High-Pressure Synthesis: Nanostructured Hexagonal 4H Polytype. 18:5989–5995, Aug 2018. ISSN 1530-6992.
- [154] Zhanbing He, Jean-Luc Maurice, Qikai Li, and Didier Pribat. Direct evidence of 2H hexagonal Si in Si nanowires. *Nanoscale*, 11:4846–4853, 2019. ISSN 2040-3372.
- [155] H. M. Jennings and M. H. Richman. A hexagonal (wurtzite) form of silicon. *Science*, 193(4259):1242–1243, 1976. ISSN 0036-8075.
- [156] J. Bandet, B. Despax, and M. Caumont. Vibrational and electronic properties of stabilized wurtzite-like silicon. *J. Phys. D: Appl. Phys.*, 35(3):234–239, jan 2002. ISSN 1361-6463.
- [157] Filippo Fabbri, Enzo Rotunno, Laura Lazzarini, Daniela Cavalcoli, Antonio Castaldini, Naoki Fukata, Keisuke Sato, Giancarlo Salviati, and Anna Cavallini. Preparing the way for doping wurtzite silicon nanowires while retaining the phase. *Nano Lett.*, 13(12):5900–5906, Nov 2013. ISSN 1530-6992.
- [158] Stefan Goedecker, Thierry Deutsch, and Luc Billard. A fourfold coordinated point defect in silicon. *Phys. Rev. Lett.*, 88:235501, May 2002. ISSN 1079-7114, 0031-9007.
- [159] Ann E. Mattsson, Ryan R. Wixom, and Rickard Armiento. Electronic surface error in the Si interstitial formation energy. *Phys. Rev. B*, 77:155211, Apr 2008. ISSN 2469-9969, 2469-9950.
- [160] Andrew J. Morris, Chris J. Pickard, and R. J. Needs. Hydrogen/silicon complexes in silicon from computational searches. *Phys. Rev. B*, 78:184102, Nov 2008. ISSN 2469-9969, 2469-9950.
- [161] Takuma Kobayashi, Kou Harada, Yu Kumagai, Fumiyasu Oba, and Yu-ichiro Matsushita. Native point defects and carbon clusters in 4H-SiC: A hybrid functional study. *J. Appl. Phys.*, 125(12):125701, 2019. ISSN 1089-7550, 0021-8979.
- [162] Jianqi Xi, Bin Liu, Yanwen Zhang, and William J. Weber. Ab initio study of point defects near stacking faults in 3C-SiC. *Comput. Mater. Sci.*, 123:131 – 138, 2016. ISSN 0927-0256.
- [163] Mariya G. Ganchenkova, Irina A. Supryadkina, Karine K. Abgaryan, Dmitriy I. Bazhanov, Ilya V. Mutigullin, and Vladimir A. Borodin. Influence of the ab-initio calculation parameters on prediction of energy of point defects in silicon. *Mod. Electron. Mater.*, 1(4):103 – 108, 2015. ISSN 2452-1779.
- [164] M. Posselt, F. Gao, and D. Zwicker. Atomistic study of the migration of di- and tri-interstitials in silicon. *Phys. Rev. B*, 71:245202, Jun 2005. ISSN 2469-9969, 2469-9950.
- [165] O. K. Al-Mushadani and R. J. Needs. Free-energy calculations of intrinsic point defects in silicon. *Phys. Rev. B*, 68:235205, Dec 2003. ISSN 2469-9969, 2469-9950.

- [166] Sholihun, Mineo Saito, Takahisa Ohno, and Takahiro Yamasaki. Density-functional-theory-based calculations of formation energy and concentration of the silicon monovacancy. *Jpn. J. Appl. Phys.*, 54(4):041301, feb 2015. ISSN 1089-7550, 0021-8979.
- [167] Pia Seeberger and Julien Vidal. On the ab initio calculation of vibrational formation entropy of point defect: the case of the silicon vacancy. *EPJ Photovolt.*, 8:85505, 2017. ISSN 2105-0716.

Ehrenwörtliche Erklärung

Ich erkläre hiermit ehrenwörtlich, dass ich die vorliegende Arbeit selbständig, ohne unzulässige Hilfe Dritter und ohne Benutzung anderer als der angegebenen Hilfsmittel und Literatur angefertigt habe. Die aus anderen Quellen direkt oder indirekt übernommenen Daten und Konzepte sind unter Angabe der Quelle gekennzeichnet.

Bei der Auswahl und Auswertung folgenden Materials haben mir die nachstehend aufgeführten Personen in der jeweils beschriebenen Weise entgeltlich/unentgeltlich geholfen:

1. Dr. Mário R. G. Marques für hilfreiche Diskussion über die Berechnung der Zustandsdichte in der Abbildung 6.2;
2. M.Sc. Ahmad W. Huran wer berechnete die in dieser Dissertation verwendeten Slater-Koster-Parameter;
3. Prof. Dr. Silvana Botti und Prof. Dr. Miguel A. L. Marques als betreuender Hochschullehrer.

Weitere Personen waren an der inhaltlich-materiellen Erstellung der vorliegenden Arbeit nicht beteiligt. Insbesondere habe ich hierfür nicht die entgeltliche Hilfe von Vermittlungs- bzw. Beratungsdiensten (Promotionsberater oder andere Personen) in Anspruch genommen.

Niemand hat von mir unmittelbar oder mittelbar geldwerte Leistungen für Arbeiten erhalten, die im Zusammenhang mit dem Inhalt der vorgelegten Dissertation stehen.

Die Arbeit wurde bisher weder im In- noch im Ausland in gleicher oder ähnlicher Form einer anderen Prüfungsbehörde vorgelegt. Die geltende Promotionsordnung der Physikalisch-Astronomischen Fakultät ist mir bekannt. Ich versichere ehrenwörtlich, dass ich nach bestem Wissen die reine Wahrheit gesagt und nichts verschwiegen habe.

Jena, 02-Juli-2021

Lebenslauf

Personal information

| | |
|----------------|--------------|
| Name | Lin Sun |
| Nationality | Chinese |
| Date of birth | 30.12.1989 |
| Place of birth | Hubei, China |

Education

- 2012 – 2015 M.Sc., School of Physics and Technology, Wuhan University, China
- 2013 – 2014 M.Sc., Department of Physics, Claude Bernard University Lyon 1, France
- 2007 – 2011 B.Sc., College of Physics and Electronic Engineering, Shanxi University, China

Jena, 02-July-2021